博士学位论文

RHIC-STAR上直接流的研究

论文作者： 陈佳赟
指导教师： 刘峰，唐爱洪
申请学位： 理学博士
专业名称： 粒子物理与原子核物理
研究方向： 相对论重离子碰撞

华中师范大学物理科学与技术学院

二零一一年五月

A Dissertation for Doctor of Philosophy in Physics

Directed Flow at STAR

by Jiayun Chen

Co-supervisor: Feng Liu and Aihong Tang

Huazhong Normal University

May 2011

摘要

二十世纪核物理的最重大成就之一是建立了强作用的基本理论－量子色动力学(QCD)。QCD是关于物质的基本组分－夸克－的动力学。在通常情况下，夸克先构成核子，再由核子构成核物质。但在特别的情况下，比如密度增大或温度升高时，核子间的边界渐渐模糊起来，夸克禁闭解除，核物质将变成新的物质形态－夸克物质(Quark Matter)。夸克物质研究是当代原子核物理最激动人心的方向之一，将深刻影响人们对于宇宙演化、星体的形成与性质、物质的微观结构与相互作用等众多方面的认识。因此，夸克物质一直引起巨大的研究兴趣：国际上有系列的夸克物质会议；国际权威学术刊物不断发表夸克物质相关的研究论文；世界上几大主要实验室(如:CERN,BNL 等)已经开始新一轮的实验探讨；天文学家也在努力寻找夸克物质的踪迹。

夸克物质可能产生的一种情况是重离子碰撞。早在30多年前，李政道先生就提出了通过重离子碰撞研究高能量密度或高重子密度物质性质的思想，并预言可能存在物理真空破缺对称的恢复及奇异致密物质态的产生。随着能量由低到高，重离子碰撞所涉及到的主要自由度将相应发生变化。在高能能区(比如RHIC/LHC能区)，重离子碰撞中可能发生由强子物质到夸克物质的退禁闭相变，形成新的物质形态。此时产生的夸克物质（如果产生）处于很高的温度状态，称为夸克-胶子等离子体(QGP)，或热夸克物质。基于格点QCD计算结果和实验研究，人们相信在RHIC能区或LHC能区的重离子碰撞中已经形成QGP。如何从末态粒子的性质判明QGP的形成和性质，是重离子碰撞实验中最为关心的一个问题。美国布鲁克海汶国家实验室（BNL）的相对论重离子对撞机（RHIC）自2000年运行以来，得到了许多激动人心的结果。大横动量强子证明了它们的相互作用在碰撞早期发生，这些相互作用很像发生在部分子之间。RHIC实验观测到了非常强的集体流，特别是观测到了碰撞早期产生的v_2对组分夸克的标度性,表明在RHIC上存在部分子的集体运动。利用高能高统计数据研究系统热化和QGP性质是RHIC的一个重要目标。物理学家们致力寻找和观测QCD相变信号，并通过研究碰撞发生后的物质动力学演化过程，进一步了解QGP产生和演化的机理。

集体流（直接流和椭圆流）与系统的早期演化有着密切的联系。测量RHIC 能区核-核碰撞的集体流能提供存在于早期演化过程中的部分子的信息，它对判明QGP是

否形成有着重要的意义,也是寻找相变的很好的探针。直接流（v_1）是发射粒子相对于反应平面分布的傅立叶变换的第一谐波系数。它描述了由碰撞产生的粒子和核碎片在X－Z平面上的方位角的分布情况，它载有碰撞最早期阶段的信息。直接流的大小和形状，特别是可鉴别粒子的直接流的大小和形状是特别有意义的，因为它们对于平衡态方程很敏感（EOS）。最近的理论研究表明，非对心碰撞中，参加碰撞的区域成一个“杏仁”状的火球，由于火球受到两个核碎片对其施加的侧向力，导致火球在X-Z平面上有一定角度的倾斜（不垂直于X-Z平面）。在随后的火球系统碰撞过程中，这种倾斜体现在作为快度函数的直接流中，在中心快度区，直接流可能呈现一个很小倾斜，甚至于完全是零。火球的倾斜扩张引起反向流（或者叫做第三种流组分）。反向流的方向是和火球面垂直，并和两个核碎片的反弹运动方向相反。如果火球的倾斜膨胀足够大，它甚至可以克服两个核碎片的反弹运动力，体现出来的是直接流在中心快度区域穿过零处三次，呈现一个摆动的结构。值的指出的是关于这个反向流的解释虽然是在与一级相变有关的SPS能区，但这个计算对于RHIC高能区的碰撞也是有可能发生。事实上，最新的引入倾斜源作为初始条件的流体力学计算给出了和实验数据一致的结果，带电粒子的直接流在中心快度区呈现了一个负向倾斜。但是这种摆动的结构也出现在相对论量子分子动力学（RQMD）模型中。在该模型中，这个摆动的结构的形成只来源于重子阻碍效应以及空间动量的正关联，没有任何的相变信息。该模型预言π介子和核子的直接流在中心快度区的方向相反。

为了区分重子阻碍效应和平滑过渡阶段有关联的反向流，可鉴别的粒子的直接流是很好的观测量，比较不同粒子的直接流在中间快度区的斜率可以提供更多的信息。特别是，质子的直接流$v_1(y)$对中心度可能揭示可能存在的一级相变。

通过对高能区域大统计量的2007年采集的200GeV金金碰撞实验数据进行研究，已经得到关于可鉴别粒子的直接流的新结果。结果包括有：pion介子，反质子，Kaon介子和Kshort的直接流是负向倾斜的，与“负向流”的图像是吻合的，但是质子的直接流在中间快度区域是接近于零。另一方面，从质子，反质子与Pion介子直接流的激发函数和模型比较的入手，发现考虑由QGP效应产生倾斜源的流体力学模型很好的描述了中心度10%-70%的质子和pion介子的结果，但无法描述质子和反质子直接流在中心度5%-30%呈现出的相当大区别。实验结果与现有的模型（RQMD，UrQMD，Ampt模型，以及部分子重组QGSM，带有倾斜源的流体力学模型）进行了比较，没有一个模型能够同时描述π介子和质子的直接流。也许解释质子

和反质子的直接流激发函数的中心度依赖的不同需要加入额外的机制。

2008 年STAR 实验组产生了部分低能的数据（9.2GeV），通过与现有STAR 实验组的高能62.4GeV 和200GeV 的带电强子集体流比较，以及其他实验组（例如NA49 的实验组）的现有结果进行了一致性比较。我们发现，直接流和现有实验结果的趋势是一致的。其结果表明STAR实验是具有进行能量扫描计划的能力。

研究了在多项输运模型AMPT 中，不同能区200, 130, 62.4, 39, 17.2 以及9.2 GeV 带电强子和可鉴别粒子的直接流关于快度、中心度、能量的依赖关系。AMPT 模型给出了与已有实验能量相符合的快度倾斜度和能量依赖的趋势，虽然数值比实验值要低。发现在AMPT 模型中，当能量达到130GeV 时候，质子的直接流改变了方向。强子再闪射效应对RHIC 高能区的直接流有很小的影响。这些结果可以帮助我们理解集体流在相对论重离子碰撞早期的性质，也可为RHIC 能量扫描计划提供参照。

关键词: 相对论重离子碰撞 集体运动 直接流 反向流

Abstract

It is widely believed that the universe began in an explosion from a small volume with all energy of the universe, and during the first a few millionths of a second in the explosion, the universe passed through a phase made of Quark Gluon Plasma (QGP), a de-confined state of quark matter. To understand the origin of the universe as well as the strong interaction itself, the Relativistic Heavy Ion Collider (RHIC) at Brookhaven National Laboratory (BNL) in USA was built to re-create the hot and dense conditions of the universe's first minute, and is currently taking data. At RHIC, two nuclei are smashed together with a speed close to the speed of light, and thousands particles are produced due to the tremendous energy deposited. In order to characterize the collision, fluid-like dynamics are applied and directed flow is one of them.

Directed flow is the first coefficient (v_1) of Fourier expansion of the azimuthal distribution of emitted particles with respect to the reaction plane. It describes the collective sideward motion of produced particles and nuclear fragments, and it carries information from the very early stage of the collision. The magnitude and the shape of directed flow, in particular those for identified particles, are of the special interest because they are sensitive to the equation of the state (EOS). Recent theoretical work shows that directed flow, as a function of rapidity(y), may exhibit a small slope (flatness) at midrapidity due to a strong expansion of the fireball being tilted away from the collision axis. Such tilted expansion gives rise to anti-flow or a 3^{rd} flow component. The anti-flow is perpendicular to the source surface, and is in the opposite direction to the bouncing-off motion of nucleons. If the tilted expansion is strong enough, it can even overcome the bouncing-off motion and results in a negative $v_1(y)$ slope at midrapidity, potentially producing a wiggle-like structure in $v_1(y)$. Note that although calculations for both anti-flow and 3^{rd} flow component are made for collisions at SPS energies where the first order phase transition to a QGP is believed to be the most relevant, the direct cause of the negative slope is the strong, tilted expansion, which is also important at RHIC's top energies. Indeed hydrodynamic calculations for Au + Au collisions at $\sqrt{s_{NN}} = 200$ GeV with a tilted source as the initial condition can give a similar negative $v_1(y)$ slope as that found

in data. A wiggle structure is also seen in the Relativistic Quantum Molecular Dynamics (RQMD) model, and it is attributed to baryon stopping together with a positive space-momentum correlation. In this picture, no phase transition is needed, and pions and nucleons flow in opposite directions.

To distinguish between baryon stopping and anti-flow associated with a phase transition, it is desirable to measure the $v_1(y)$ for identified particles and compare the sign of their slopes at midrapidity. In particular, the observation of a centrality dependence of proton $v_1(y)$ may reveal the character of a possible first order phase transition. It is expected that in very peripheral collisions, protons flow in the same direction as spectators. In mid-central collisions, if there is a phase transition, the proton $v_1(y)$ slope at midrapidity may change sign and become negative. Eventually the slope diminishes in central collisions due to the symmetry of collisions.

At top RHIC energies, v_1 has been studied mostly for charged particles by both the STAR and the PHOBOS collaborations. It is found that v_1 in the forward region follows the limiting fragmentation hypothesis, and $v_1(\eta)$ depends only on the incident energy, but not on the size of the colliding system at a given centrality in Au+Au collisions are measured by the STAR experiment before 2005. The system size independence of v_1 can be explained by the hydrodynamic calculation with a tilted initial condition.

In this thesis, p, $\bar{p}$,K_s^0, Λ and $\bar{\Lambda}$'s directed flow in Au+Au collisions at $\sqrt{s_{NN}} =$ 62 GeV and $\sqrt{s_{NN}} =$ 200 GeV are measured by the STAR experiment in Run 4. To improve the event plane resolution, we determine the event plane from sideward deflection of spectator neutrons measured by STAR’ s shower maximum detector at zero degree calorimeters (ZDC-SMD), together with tracks reconstructed with the forward time projection chambers (FTPC). Our result is presented as a function of pseudorapidity, transverse momentum and centrality. within the rapidity range we studied, at both energies, proton v_1 is less than 1%, and antiproton is less than 2%, v_1 for K_s^0, Λ and $\bar{\Lambda}$ are found not more than 5%.

The systematic study of v_1 for identified particles at RHIC did not begin until recently because it is more challenging for two reasons: 1) v_1 for some identified particles (for example, protons) is much smaller than that of all charged particles, thus is more difficult to measure; 2) more statistics are needed to determine v_1 for identified particles other than pions. STAR's measurements of directed flow (v_1) at midrapidity for $\pi^{\pm}$, $K^{\pm}$, K^0_S, p and $\bar{p}$ in Au + Au collisions at $\sqrt{s_{NN}}$ = 200 GeV in Run 7 are presented. A negative $v_1(y)$ slope is observed for most of produced particles ($\pi^{\pm}$, $K^{\pm}$, K^0_S and $\bar{p}$). In 10-70% central collisions, $v_1(y)$ slopes of pions, kaons(K^0_S), and antiprotons are found to be mostly negative at mid-rapidity. However, protons exhibits a clearly flatter shape than that for antiprotons. A sizable difference is seen between v_1 of protons and antiprotons in 5-30% central collisions. Comparison to models (RQMD, UrQMD, AMPT, QGSM with parton recombination, hydrodynamics with a tilted source) is made. None of models explored can describe $v_1(y)$ for pions and protons simultaneously. An additional mechanism besides the anti-flow needs to explain the centrality dependence of the difference between the $v_1(y)$ slopes of protons and antiprotons.

The directed flow of charged hadron and identified particles has been studied in the framework of a multi-phase transport (AMPT) model, for ^{197}Au+^{197}Au collisions at $\sqrt{s_{NN}}$ =200, 130, 62.4, 39, 17.2 and 9.2 GeV. The rapidity, centrality and energy dependence of directed flow for charged particles over a wide rapidity range are presented. v_1 values calculated from the AMPT model for different energies are discussed. It is found that the AMPT model gives the right shape of v_1 versus y while underestimating the magnitude, possibly due to the lack of mean-field in its hadron cascade. AMPT model can describe the trend of the v_1 slope's energy dependence while missing the magnitude by a fraction of 75%. Hadronic rescattering is found to be less important at high energies as the strong collective motion becomes to be the dominant dynamics.

Exploring the quantum chromodynamics phase diagram is one of the target of heavy-ion collision experiments. The QCD phase diagram is usually plotted as the temperature (T) *vs.* the baryon chemical potential (μ_B). Experimentally we can access this phase diagram and vary these initial conditions by changing the beam energy. As an initial step to exam the capabilities of the collider and experiments, a test run is made for Au + Au collisions at $\sqrt{s_{NN}}$ = 9.2 GeV. The period of data taken lasted for less than 5 hour at the Solenoidal Tracker at RHIC (STAR) experiment. The preliminary results

on directed flow v_1 from STAR will be reported in this thesis later. The directed flow results from Au + Au $\sqrt{s_{NN}} = 9.2$ GeV are similar to those obtained from collisions at similar energies. The results besides the directed flow from Au + Au at $\sqrt{s_{NN}} = 9.2$ GeV demonstrates the capabilities of the STAR detector to pursue the proposal Beam Energy Scan.

Keywords: relativistic heavy-ion collision, collective motion, directed flow, anti-flow

TABLE OF CONTENTS

List of Figures

LIST OF TABLES

CHAPTER 1

Introduction

It is widely believed that the universe began in an explosion from a small volume with all energy of the universe, and during the first a few millionths of a second in the explosion, the universe passed through a phase made of Quark Gluon Plasma (QGP) [1], a deconfined state of quark matter. To understand the origin of the universe as well as the strong interaction itself, the Relativistic Heavy Ion Collider (RHIC) at Brookhaven National Laboratory (BNL) in USA was built to re-create the hot and dense conditions of the universe's first minute, and is currently taking data.

1.1 QGP and Quantum ChromoDynamics

The standard model of particle physics is a theory concerning the electromagnetic, weak, and strong nuclear interactions, which mediate the dynamics of the known subatomic particles. Developed throughout the early and middle 20th century, the current formulation was finalized in the mid 1970s upon experimental confirmation of the existence of quarks. Since then, discoveries of the bottom quark (1977), the top quark (1995) and the tau neutrino (2000) have given credence to the standard model. This model contains six flavors of quarks (q), named up (u), down (d), charm (c), strange (s), top (t), and bottom (b), shown in Fig. 1.1. Antiparticles of quarks are called antiquarks, and are denoted by a bar over the symbol for the corresponding quark, such as u for an up antiquark. As with antimatter in general, antiquarks have the same mass, mean lifetime, and spin as their respective quarks, but the electric charge and other charges have the opposite sign. Quarks are spin-$\frac{1}{2}$ particles, implying that they are fermions according to the spin-statistics theorem. They are subject to the Pauli exclusion principle, which

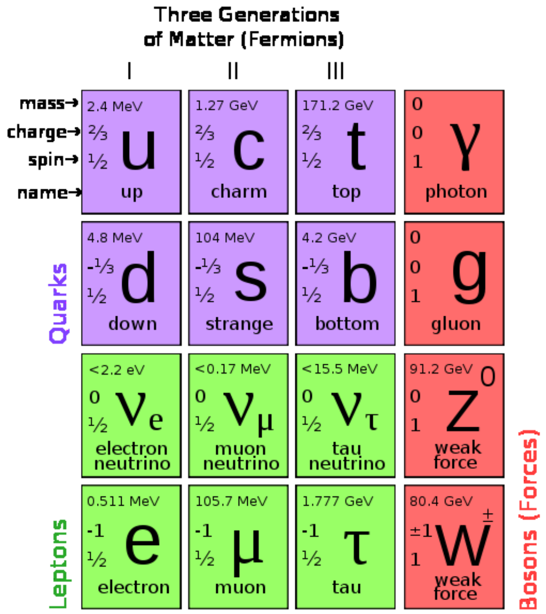

Figure 1.1: Six of the particles in the Standard Model are quarks (shown in purple). Each of the first three columns forms a generation of matter.

states that no two identical fermions can simultaneously occupy the same quantum state. This is in contrast to bosons (particles with integer spin), any number of which can be in the same state [2]. Unlike leptons, quarks possess color charge, which causes them to engage in the strong interaction. The resulting attraction between different quarks causes the formation of composite particles known as hadrons.

The theory of quark-gluon interactions is governed by Quantum Chromo-Dynamics (QCD) [3]. QCD is the unbroken SU(3) color non-Abelian gauge theory to describe the strong interactions, and together with the spontaneously broken $SU(2) \times U(1)$ electroweak theory, establishes the two basic components of the Standard Model of particle physics. QCD is an expanded version of the very successful theory of Quantum Electro-Dynamics (QED). Both QCD and QED are based on Quantum Field theory. However, there are crucial differences between QCD and QED. There is only one electric charge in QED, and the electromagnetic force bosons, photons, are electric charge neutral and do not self-interact. On the other hand the color charge in QCD has three components. Quarks change their color states by emitting or absorbing gluons. Due to the color conservation, gluons are required to also carry color charge and as a result self-interact. In

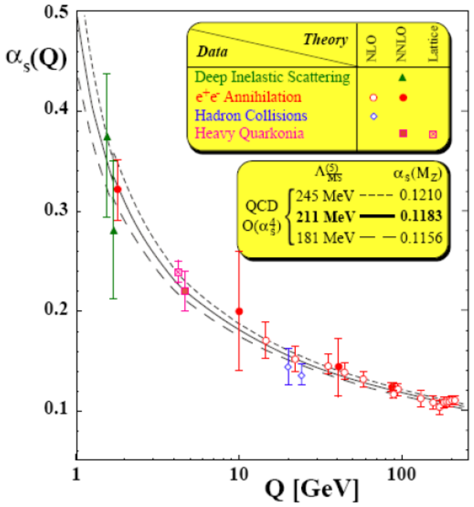

Figure 1.2: The measured QCD running coupling constant α_s from a variety of experiments compared to the QCD prediction. [5]

fact, it is the gluon self-interaction that makes QCD dynamics so peculiar [4].

For the electromagnetic force in QED, the coupling constant $\alpha = \frac{1}{137}$ is much less than unity and the use of perturbation theory is well established in QED. However, the gluon self-interactions lead to a completely different coupling constant in QCD. The effective coupling constant of strong interaction, α_s, has been experimentally measured to be a function strongly depending on the distance of interaction or the momentum transfer, written as:

$$\alpha_s(Q^2) \approx \frac{12\pi}{\beta_0 \ln(Q^2/\Lambda_{QCD})} \tag{1.1}$$

where Q^2 is the momentum transfer, Λ_{QCD} is the famous QCD scale and β_0 is a constant. Fig. shows the strong coupling constant, α_s, at different momentum transfer, Q, from various experiments as well as the QCD calculations.

The behavior in QCD running coupling constant illustrates two remarkable features of QCD. α_s becomes very small at very high momentum transfers or very short distances; thus quarks and gluons interact very weakly. This is known as asymptotic freedom [6, 7], which was first discovered in the early 1970s and honored by a Nobel Prize in 2004. At large distances or small momentum transfers, α_s becomes strong. The larger the distance that two quarks are separated the stronger the coupling; and thus the more self-coupled gluons holding the quarks together. That means an infinite amount of energy is needed to separate two quarks. As a result there are no isolated quarks and quarks are bound into color neutral hadrons. This is known as quark/color confinement. The confinement principle has never been rigorously proved. However, all experimental results concerning hadrons unambiguously support the quark/color confinement.

Accordingly, QCD yields two qualitatively different pictures to describe quark-gluon interactions. In the regime where the momentum transfer is high, i.e., the distance of interaction is small, perturbative expansions in α_s are applicable. Physics observables can be calculated in a truncated series as leading order (LO), next-to-leading order (NLO), etc. Over the past decades, there are plenty of experiments on hard processes providing quantitative tests on the validity of the perturbative QCD (pQCD) calculations. pQCD has been proven to describe a large set of high energy, large momentum transfer processes with high accuracy.

The non-perturbative quark-gluon interactions at long distances, i.e., at small momentum transfers, are always present in any process involving the strong interaction. Physicists have made significant efforts to bridge the gap between perturbative and non-perturbative regimes. Powerful numerical methods of solving QCD on a lattice of space and time (LQCD) have been developed. The principle of LQCD is to replace continuous space-time with a discrete lattice. LQCD needs no additional assumption beyond QCD. It has exactly as many free parameters as QCD itself, which are the strong coupling constant and one mass per quark species [8]. Although the performance is limited by computer memory and speed, LQCD provides a mathematically well-defined framework for non-perturbative QCD.

1.2 Heavy Ion Collider

As quark gluon plasma is believed to be the state of the matter which existed for a millionth of a second after the Big Bang. The collision of the relativistic heavy ions could

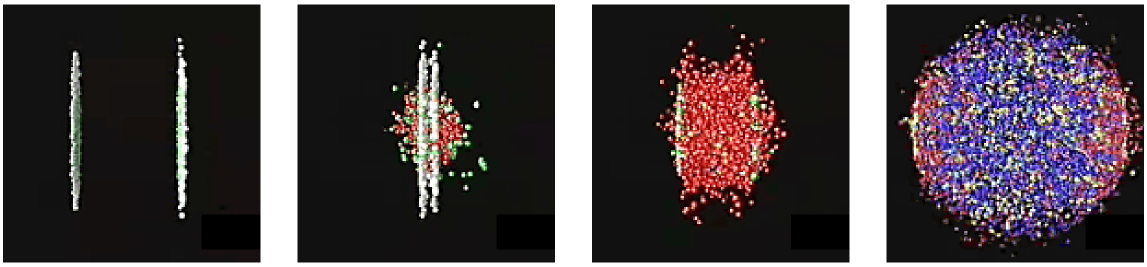

1. Ions about to collide* 2. Ion collision 3. Quarks, gluons freed 4. Plasma created

Figure 1.3: Simplified picture of two high energy nuclei from a central collision in the central of mass frame.

create the conditions of the early universe in the laboratory. Ultra-relativistic heavy-ion experiments have been performed at the Brookhaven National Lab - Alternating Gradient Synchrotron (AGS) with maximum center of mass energies of $\sqrt{s_{NN}}$ = 4.75 GeV, the CERN Super Proton Synchrotron (SPS) with maximum center of mass energies of $\sqrt{s_{NN}}$ = 17.2 GeV and the Brookhaven National Lab - Relativistic Heavy Ion Collider (RHIC) with maximum center of mass energies of $\sqrt{s_{NN}}$ = 200 GeV. The Large Hadron Collider (LHC) at CERN will be commissioned for Pb+Pb collisions at an energy of $\sqrt{s_{NN}}$ = 5.5 TeV. The measurements described in this thesis are performed by the Solenoidal Tracker at the Relativistic Heavy Ion Collider (STAR).

Fig. 1.3 shows a simplified picture of two high energy nuclei from a central collision in the central of mass frame, here the nuclei appear as thin discs due to the Lorentz Contraction during the collision. In the central region where the energy density is highest, it is expected that a new state of matter - the QGP is created. The state pass through some intermediate states with different properties and in this process it cools down. The quarks combine to hadrons, the interactions among them cease until the temperature of system come to the freeze-out temperature. The thousands more hadrons are formed and move towards the detectors. Each of these particles provides an important clue as to what occurred inside this collision.

The space time gradual development of of a heavy-ion collision is illustrated in

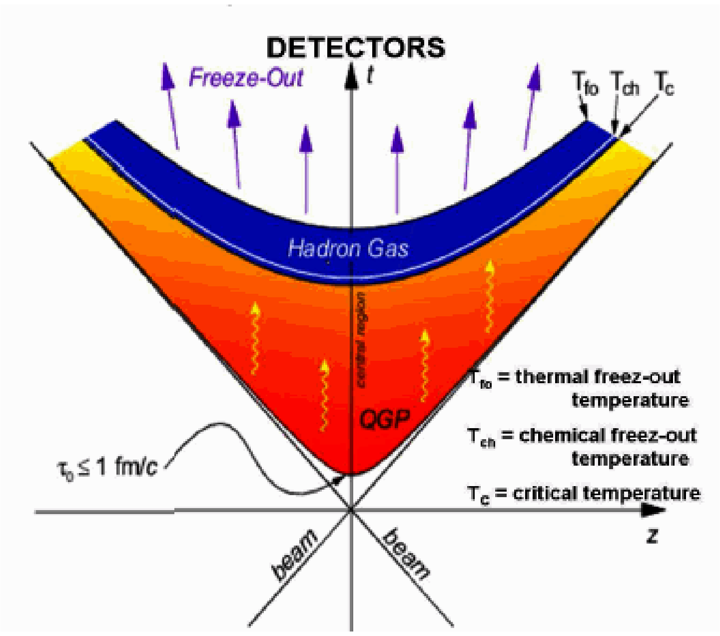

Figure 1.4: Illustration of the characteristic periods in time for the Heavy Ion Collision.

Fig. 1.4. The nuclei travels at relativistic velocities appear Lorentz-contracted in the laboratory frame. After the collision, there is a large amount of the energy deposited in the interaction region. If the energy density is large enough and the temperature of the created system (t) exceeds the Critical Temperature T_c, a phase transition is expected to occur and a fireball of unconfined quarks and gluons is formed. Interactions among quarks and gluons may lead to thermalization and chemical equilibration. The subsequent expansion of the medium is then governed by the equation of state of the QGP. As the system expands and cools down to the critical temperature T_c, hadronization stage takes place and the quarks and gluons become confined. Due to the finite formation time of the hadrons, the system is likely to evolve through a mixed phase where free quarks and gluons exist simultaneously with hadrons. Once all the quarks and gluons are confined inside hadrons, the system turns into a hadron gas. As the hadron gas continues to expand and the temperature cools down to the chemical freeze-out temperature T_{ch}, the inelastic scattering between hadrons cease and the relative abundance for hadron species will not change any more. When the system becomes so dilute that the hadrons even no longer interact with each other elastically, and the system becomes free-streaming, kinetic freeze-out occurs indicated by T_{fo}.

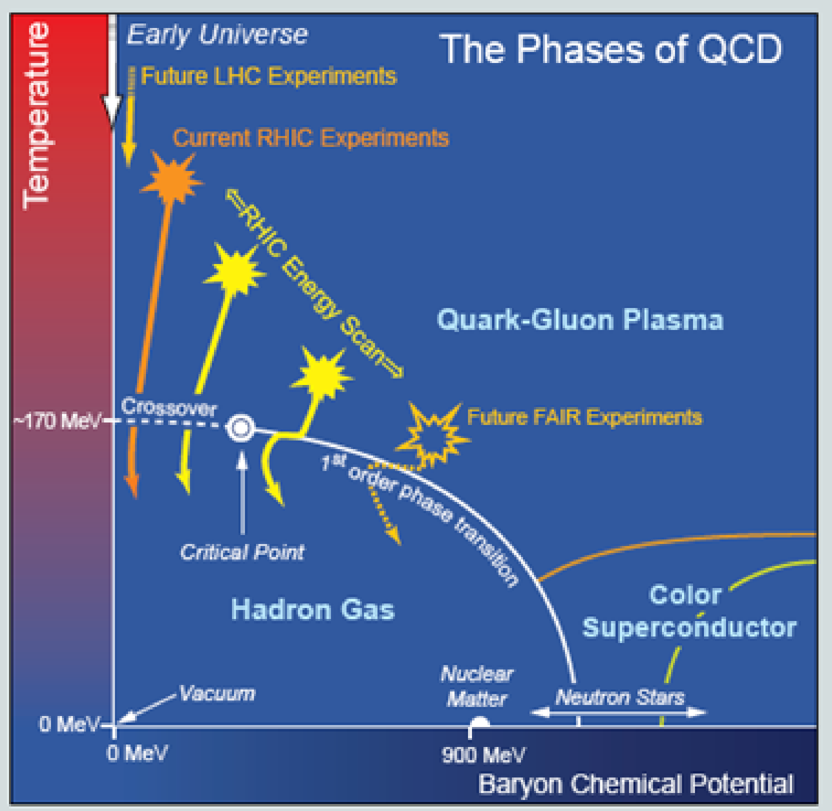

Figure 1.5: Theoretical Phase Diagram of nuclear matter.

In the first decade of STAR running, the evidence about the existence of a strongly coupled Quark Gluon Plasma (sQGP) [9] came in the form of strong suppression of particle production at large p_T [10] and the large amount of elliptic flow [11]. As an important step towards understanding the properties of sQGP and the structure of the QCD phase diagram, a systematic analysis of particle production as a function of collision energy is necessary. Theoretical calculations have indicated that the order of the transition from hadronic matter to the sQGP depends on the baryon chemical potential (μ_B) and temperature (T), shown in Fig. 1.5: at low μ_B and high T, a cross-over transition occurs[12]; at high μ_B and low T, the phase transition is thought to become first order [13]; this first order phase transition "meets" with the smooth cross-over at the critical point[14]. Experimentally we can access this phase diagram and vary these initial conditions by changing the beam energy. Thus a beam energy scan (BES) program will help us to explore the QCD phase diagram and to locate the critical point [15, 16]. As a first step of the BES program, RHIC made a test run for Au+Au collisions at $\sqrt{s_{NN}} = 9.2$ GeV. The preliminary results about directed flow in this test run from STAR will be reported in this thesis later.

1.3 Directed Flow

At RHIC, two nuclei are smashed together with a speed close to the speed of light, and thousands particles are produced due to the tremendous energy deposited. Thus occurrence of some multiparticle correlations, or collective phenomena, might be expected. These correlated emission of the produced particles, called "flow", was observed already in nuclear collisions at low energies [17, 18], and at present show up in the relativistic high energies. The term "flow" could be understood as a phenomenological description of the collective expansion from the produced particles in the collision.

As seen in Fig. 1.6, in the non-central collision (with the impact parameter $b > 0$), the two nuclei passes through each other, left an almond shaped fireball and the nuclei fragments. The plane defined by the beam direction and the impact parameter (b) is called the reaction plane (or X-Z plane). The impact parameter is the distance between

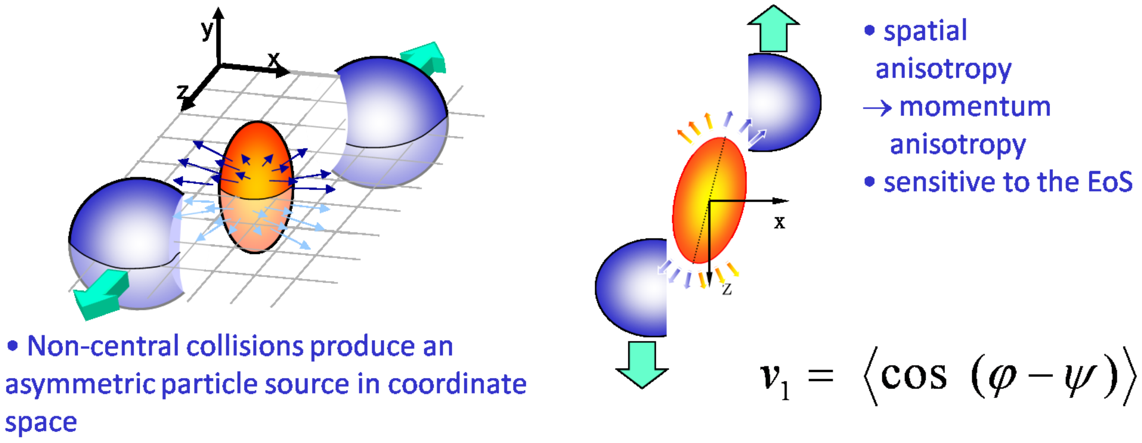

Figure 1.6: Sketch of an almond shaped fireball and the nuclei spectators, where z direction is the collision axis.

the centers of the nuclei in the transverse plane (X-Z plane).

In order to characterize the collective expansion of the particles in the X-Z plane, the particular type named "directed flow" is applied. As seen in Fig. 1.6, it named so because it has a direction and shows opposite sign in the two hemisphere.

The distribution of the particles in the azimuthal angle ϕ in the transverse plane is usually analyzed in the terms of the Fourier expansion [19]:

$$E\frac{d^3N}{d^3p} = \frac{1}{2\pi}\frac{d^2N}{p_T dp_T dy}(1 + 2\sum_{n=1}^{\infty} v_n(p_T, y)cos[n(\phi - \psi_R)]) \tag{1.2}$$

where ψ_R defines the angle of the reaction plane, seen in Fig. 1.6. The method of the estimation of the reaction plane and its resolution will explained in detail in the section (3.1.5) and (3.1.6).

Directed flow is the first coefficient (v_1) of Fourier expansion of the azimuthal distribution of emitted particles with respect to the reaction plane. It describes the collective sideward motion of produced particles and nuclear fragments, and it carries information from the very early stage of the collision [23, 24, 25]. The magnitude and the shape of directed flow, in particular those for identified particles, are of the special interest because they are sensitive to the equation of the state (EOS) and and may carry a phase

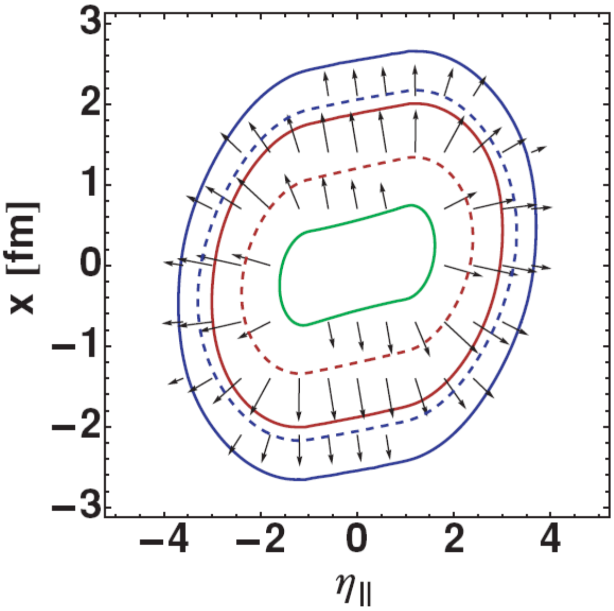

Figure 1.7: Contour plot of the initial pressure p(η, x, y = 0) in the fireball for the shifted densities for tilted initial conditions [26].See text in detail.

transition signal [22].

Recent theoretical work shows that in almost head-on collisions, due to the strong expansion of a QGP and the positive space-momentum correlation, directed flow as a function of rapidity crosses zero three times around mid-rapidity, and display a wiggle structure through the hydrodynamic evolution, seen in Fig. 1.7. The solid lines correspond to the pressure of 9, 3 and 1 GeV/fm^3 for Au + Au collisions with the impact parameter (b = 11 fm). The dashed lines are presented the pressure of 3 and 1 GeV/fm^3 for Cu + Cu collision with the parameter (b = 7.6 fm). The arrow shows the gradients $(-\partial_\eta p/\tau_0,\ -\partial_x p)$ for Au + Au collisions by the arbitrary units. It is the build up the flow away from the collision axis because of a tilt of the source, by assuming the initial density results from a superposition of the energy density which is radiated by the color sources in the target and the projectile. There is effects leading to the directed flow shows a negative sign.

The negative directed flow calculations are also made for collisions at SPS energies where the first order phase transition to a QGP is believed to be the most relevant [22]. It is argued that directed flow as function of rapidity(y), may exhibit a small slope (flatness) at midrapidity due to a strong expansion of the fireball being tilted away from the collision axis. Such tilted expansion gives rise to anti-flow [20] or a 3^{rd} flow component [21]. The anti-flow is perpendicular to the source surface and in the opposite direction to the bouncing-off motion of nucleons spectators. If the tilted expansion is strong enough, it can even overcome the bouncing-off motion and results in a negative $v_1(y)$ slope at midrapidity, potentially producing a wiggle-like structure in $v_1(y)$.

A wiggle structure is also seen in the Relativistic Quantum Molecular Dynamics (RQMD) model [37], shown in Fig. 1.8. This wiggle structure is attributed to baryon stopping together with a positive space-momentum correlation. It studies Au + Au collisions at $\sqrt{s_{NN}}$ = 200A GeV with the impact parameter range (b = 5 - 10 fm) in the relativistic quantum molecular dynamics (RQMD V2.4) model in cascade mode [38]. There are two Fourier coefficients here:

- the coefficient in the momentum space (at a given rapidity and transverse momentum): $v_1 = \langle \cos\phi \rangle$ where ϕ is the the azimuthal angle of a particle relative to the reaction plane angle (p_x-p_z plane).
- the coefficient in the coordinate space $s_1 = \langle \cos\phi_s \rangle$ where ϕ_s is the azimuthal angle of a particle relative to the reaction plane angle (X-Z plane), which is determined from the freeze-out coordinates X and Y.

Fig.1.8 shows the y_1 and s_1 for nucleons and pions in Au + Au collisions at RHIC energy from RQMD calculations. For the nucleons, both y_1 and s_1 show a negative slope at mid-rapidity, and larger rapidities the s_1 values leave the ordinate scale. The momentum distribution seems to follow the space distribution, because of the positive space-momentum correlation. Thus, positive slope of y_1 at mid-rapidity for the pions. But for pions, there is not ignorable effect from shadowing by nucleons. Compared to the large rapidity region, this contribution is relatively small in the midrapidity region where the nucleon-to-pion ratio is small. The shadowing effect becomes more dominant at beam-target rapidity region. That is why the pions v_1 has the opposite sign from s_1 close to beam rapidity region. In this picture, no phase transition is needed, and pions and nucleons flow in the opposite directions.

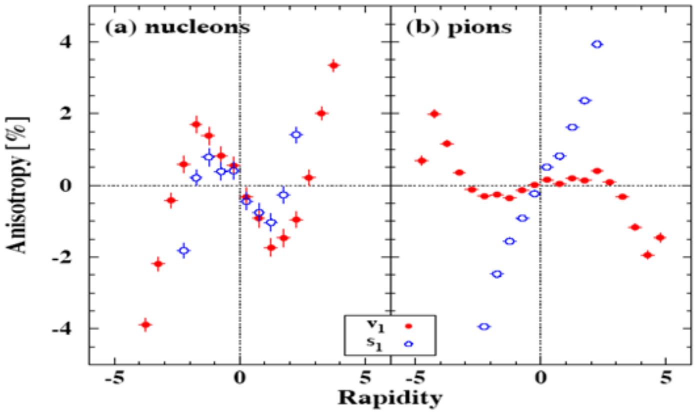

Figure 1.8: RQMD calculations of y_1 (filled circles) and s_1 (open circles) for nucleons (a panel) and pions (b panel). [37].See text in detail.

To distinguish between baryon stopping and anti-flow which is associated with a phase transition, it is desirable to measure the directed flow as function of rapidity for identified particles and compare the sign of their slopes at midrapidity. Particularly, the observation of the centrality dependence of proton $v_1(y)$'s slope (the excitation function) may reveal the character of a possible 1^{st} order phase transition [22].

CHAPTER 2

Experimental Setup

2.1 The RHIC accelerator

The Relativistic Heavy Ion Collider(RHIC) is the first collider in the world capable of colliding heavy ions. The center-of-mass collision energy is up to 200 GeV per nucleon pair, which is about more than 10 times greater than the highest energy reached at previous fixed target experiment. The atoms have had their outer cloud of electrons removed. The RHIC primarily uses ions of gold (one of the heaviest common elements), because that its nucleus is densely packed with particles. It started to construct during the year 1991 and began to operate in 2000. In the following the decades, it developed and continued under construction. The purpose of this extraordinary new accelerator is to seek out and explore new extremely high-energy and high-temperature forms of matter. Thus it continue to seek out the answer for the centuries-old question to understand the nature and origins of matter at its basic level. RHIC is also delivering the polarized proton beams up to center-of-mass energy 500 GeV/c to carry on vigorous spin scientific program.

	For Au + Au	For p + p
Beam Energy	100 → 30 GeV/nucleon	250 → 30 GeV/nucleon
Luminosity	2×10^{26} cm^{-2}s^{-1}	1.4×10^{31} cm^{-2}s^{-1}
Number of Bunches/ring	60 (→ 120)	60 (→ 120)
Luminosity Lifetime	$\sim$ 10 hours	$>$ 10 hours

Table 2.1: Performance specifications of RHIC

The original design parameters of the collider are list in Table. 2.1. [27]. At present, the actual achieved luminosity is much higher than the design. The store-averaged luminosity right now are 12×10^{26} cm^{-2}s^{-1} for Au + Au collisions, 2.3×10^{31} cm^{-2}s^{-1} for p + p collisions and 1.3×10^{29} cm^{-2}s^{-1} for d + Au collisions.

Fig. 2.1 shows a diagram of the RHIC machine complex. It has two 3.8 km rings to collide relativistic heavy ions, and polarized protons at six intersection points. It includes

- a Van de Graaff facility,
- a Linear Proton Accelerator,
- the Booster Synchrotron Ring,
- the Alternative Gradient Synchrotron (AGS),
- the RHIC Synchrotron Ring,

The process is in this order: For gold (Au) beam operations, the gold ions with charge $Q = -1e$ are created by the Pulsed Sputter Ion Source. Then, they go through the Van de Graaff facility which used to accelerated the gold ions with a series of stripping foils. At the exit of this facility, the gold ions are speeded up to a kinetic energy of 1 MeV/nucleon within a net charge of $Q = +32e$. In the following stage, the gold ions are injected into the booster synchrotron and continued to be accelerated to an energy of 95 MeV/nucleon. When the gold ions leave the booster, they could be stripped more to $Q = +77e$. Next, the gold ions are transferred to the AGS in which they are accelerated to 8.86 GeV/nucleon and arranged into four final bunches. Ultimately, the gold ions are injected into RHIC, stripped into the bare charge state ($Q = +79e$) during the transfer. For p+p operations, it is different from the gold beam operations. The protons are injected with 200 MeV by the Linac into the booster. And then they are accelerated in the AGS and injected into RHIC rings.

The two concentric super-conducting rings are indicated as the blue ring and the yellow ring. At the cross of these rings, there are six interaction points, which allow the particle beams to collide. The four interaction points are four experimental detector systems:

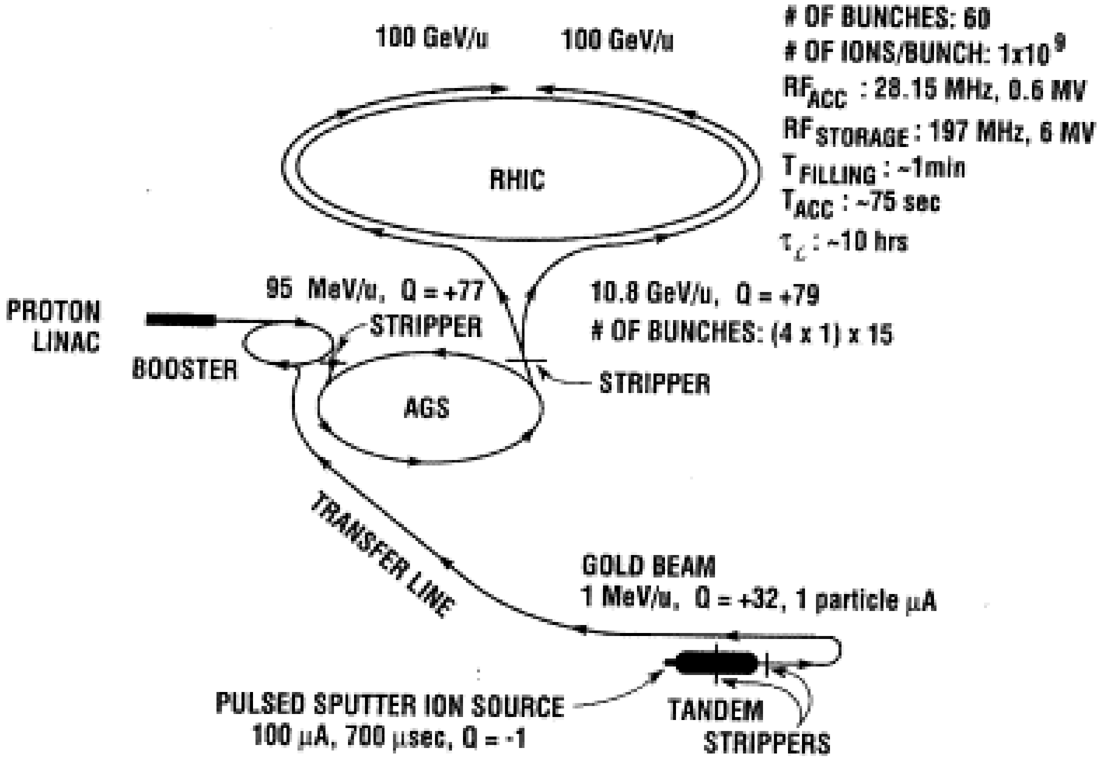

Figure 2.1: Schematic of the RHIC complex

- STAR (6 o'clock),
- PHENIX (8 o'clock),
- PHOBOS (10 o'clock),
- BRAHMS (2 o'clock).

In this dissertation research, we focus on the analysis of the Au + Au collisions at $\sqrt{s_{NN}} = 200$ GeV recorded by the STAR detector in year 2004 and 2007, at $\sqrt{s_{NN}} = 62.4$ GeV in year 2004.

2.2 The STAR detector

The Solenoidal Tracker At RHIC (STAR) is one of the four detector systems constructed at RHIC. It specializes in tracking thousands of particles produced by each ion collision at RHIC with high energy. STAR is a detector with a large acceptance, it is designed with an azimuthal symmetric acceptance (complete 2π in azimuthal) and large range around mid-rapidity, as shown in Fig. 2.2. This is the perspective view of the STAR detector with cutaway showing the inner components [28]. It could study a broad rang of physical observable. An emphasis was placed on mid-rapidity range physics to study both the soft (non-perturbative) and hard (perturbative) aspects physics at RHIC energies.

Fig. 2.3 presents the layout view of the STAR detector. The STAR subsystems and the main functions are as following:

- Time Projection Chamber (TPC): track the charged particles and particle identification (PID) in the mid-rapidity ($|\eta| < 1.3$).
- Forward Time Projection Chamber (FTPC): track forward region charged particles in the rapidity range ($2.5 < |\eta| < 4.2$).
- Silicon Vertex Tracker (SVT): track interaction region charged particles
- Time of Flight (TOF): particle identification

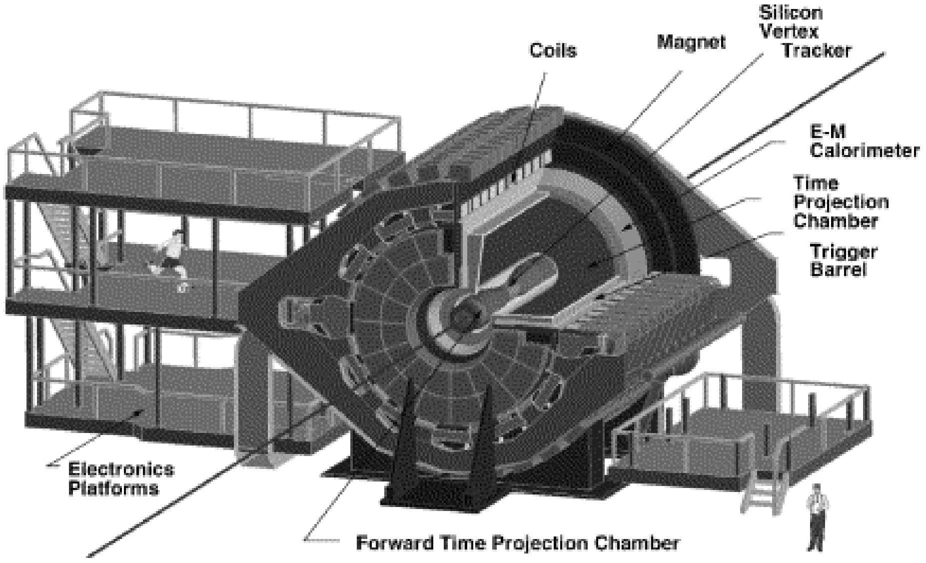

Figure 2.2: The perspective view of the STAR detector with cutaway showing the inner components.

- Barrel Electro-Magnetic Calorimeter (BEMC): measure the mid-rapidity range electrons, positrons and photons, and trigger high p_T events.
- Endcap ElectroMagnetic Calorimeter (EEMC): measure large-rapidity electrons, positrons and protons.
- Zero-Degree Calorimeter (ZDC): measure neutrons along the beam direction for event triggering
- Central Trigger Barrel (CTB): measure charged particles at midrapidity with a fast response for event trigger

The STAR magnet is cylindrical with the length of 6.85 m in design. It has inner and outer diameters of 5.27 m and 7.32 m, respectively. It generates a field along the length of the cylinder having maximum field strength of 0.5 Tesla. The magnetic field allows the tracking detectors to measure the bend trajectory of charged particles, thus get their momenta. To date, the STAR magnet is adjustable and has been run in full field, reversed full field and half field configurations.

The main detector are used in this dissertation research are Time Projection Chamber (TPC) [31], Forward Time Projection Chamber (FTPC) [32] and Shower Maximum

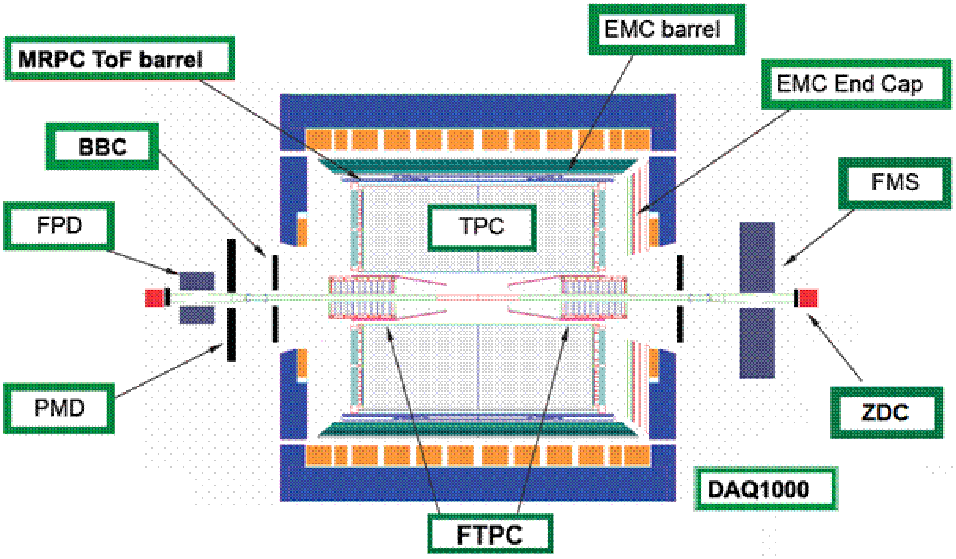

Figure 2.3: The layout view of the STAR detector.

Detector inside the Zero Degree Calorimeters (ZDC-SMD) [33].

2.2.1 The STAR's Time Projection Chamber (TPC)

The Time Projection Chamber (TPC) is the STAR primary tracking device [31]. The TPC is designed to track the particles, provide the information of their momenta, and the particle identification information by measuring their ionization energy loss (dE/dx). Charged particles are identified over a momentum range from 100 MeV/c to greater than 1 GeV/c and momenta are measured over a range of 100 MeV/c to 30 GeV/c.

It consists of a 4.2 m long cylinder with 4.0 m in diameter. The cylinder is concentric with the beam pipe. The inner and outer radii of the active volume are 0.5 m and 2.0 m, respectively. The TPC has the full azimuthal ($0 < \phi < 2\pi$) coverage. Its pseudo-rapidity coverage is $|\eta| < 2.0$ for inner radius and $|\eta| < 1$ for outer radius ideally. Fig. 2.4 shows the cutaway view of the STAR's TPC structure. The TPC sits in a homogeneous magnetic field up to 0.5 Tesla along the z axis, provided by a solenoidal magnet outside the drift chamber. The main components of TPC are

- the Central Membrane(CM): typically held at -28 kV high voltage, divide the TPC into two parts (the length of each is 2.1 m). A chain of 183 resistors and

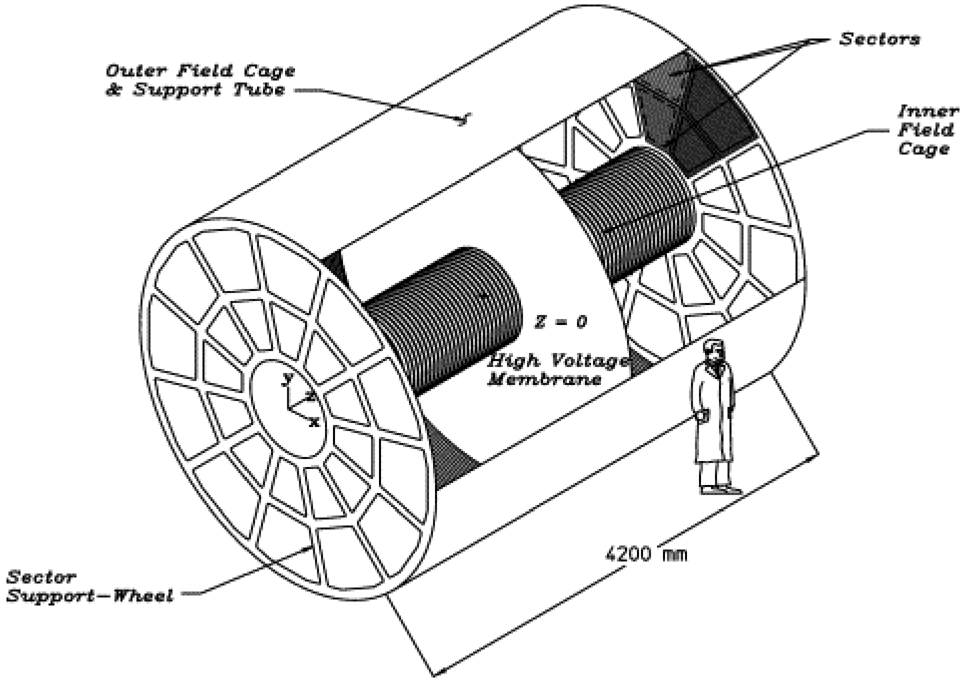

Figure 2.4: The Cutaway view of the STAR's TPC detector

equipotential rings along the inner and outer field cage create a uniform drift field (135 V/cm) between the CM and each end cap. Consequently the electric field and the magnetic field are parallel inside the TPC. The uniformity of electric field is critical because the track reconstruction precision is better than 1 mm and electron drift paths are up to 2 m.

- outer field cage (OFC), the inner field cage (IFC): The concentric IFC (radius = 0.5) and OFC cylinders (radius = 2.0 m)
- the anode read out end caps, which are 2.1 m away from the CM, define two coaxial cylindrical drift volumes of 24.75 m^3.

The working gas of the TPC is P10, consistent of 90% Ar and 10% CH4, regulated 2 mbar above the atmospheric pressure. The readout system is based on the Multi-Wire Proportional Chamber (MWPC) with readout pads. Each readout pad is divided into inner and outer sub-sectors. While the inner sub-sector is designed to handle high track density near collision vertex. The 136,608 readout pads provide (x,y) coordinate information, while z coordinate is provided by 512 time buckets and the drift velocity.

Typical resolution is about 0.5 - 1.0 mm. When charged particles traverse the TPC, they liberate the electrons from the TPC gas due to the dE/dx. These electrons are drifted towards the end cap planes of the TPC and collected by a readout pad. The signal is amplified and integrated by a circuit containing a pre-amplifier and a shaper. Then it is digitalized and then transmitted over a set of optical fibers to STAR Data Acquisition system (DAQ).

At the DAQ stage, raw events containing millions of ADC values and TDC values were recorded. Raw data were then reconstructed into hits, tracks, vertices, the collision position through the reconstruction chain of TPC by Kalman method. The TPC reconstruction process begins by the 3D coordinate space points finding. This step results in a collection of points reported in global Cartesian coordinates. The Timing Projection chamber Tracker (TPT) algorithm is then used to reconstruct tracks by helical trajectory fit. The resulted track collection from the TPC is combined with any other available tracking detector reconstruction results and then refit by application of a Kalman filter routine, it is complete and robust statistical treatment. The primary collision vertex is then reconstructed from these global tracks and a refit on these tracks with the distance of closest approach (DCA) less the 3 cm is preformed by a constrained Kalman fit that forces the track to originate from the primary vertex. As expected, the vertex resolution decreases as the square root of the number of tracks used in the calculation. The primary vertex resolution is $\sim 350\ \mu$m with a track multiplicity above 1000. The reconstruction efficiency including the detector acceptance for primary tracks depends on the particle type, track quality cuts, p_T , track multiplicity etc. The typical value for the primary pions with $N_{fit} \geq 25$ and $|\eta|$ <0.7, DCA $<$ 3.0 cm is approximate constant at $p_T >$ 0.4 GeV/c: >90% for Au+Au peripheral collisions and $>$ 80% for central collisions, respectively.

The TPC provide the track momentum and the dE/dx information for charged particles identification. For a particle with charge z (in units of e) and speed $\beta = v/c$ passing through The mean rate of dE/dx is given by the Bethe-Bloch equation [34]:

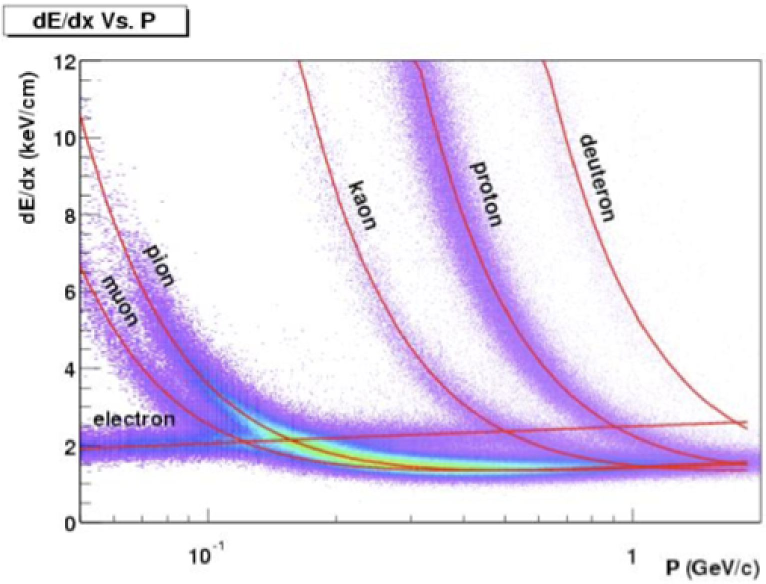

Figure 2.5: The dE/dx distribution for primary and secondary particles in the STAR TPC as a function of the momentum of primary particles with the magnetic field was 0.25 T.

$$-\frac{dE}{dx} = Kz^2\frac{Z}{A}\frac{1}{\beta^2}[\frac{1}{2}ln\frac{2m_ec^2\beta^2\gamma^2T_{max}}{I^2} - \beta^2 - \frac{\delta}{2}] \tag{2.1}$$

The meaning of each symbol can be referred to Ref. [34]. Different types of particles (different rest masses) with the same momentum have different kinematic variables β (γ, which may result in distinguishable dE/dx. The typical resolution of dE/dxx in Au + Au collisions is $\sim$ 8%, which makes the π/K separation up to p $\sim$ 0.7 GeV/c and proton/meson separation up to p $\sim$ 1.1 GeV/c. The curves in Fig. 2.5 indicate the expected ionization energy loss for different particle species according to the Bethe-Bloch equation.

Combined the TPC with other detectors, such as the TOF detector and the BEMC, etc., the capability of particle identification can be greatly improved, particle separation can be extended to higher p_T region.

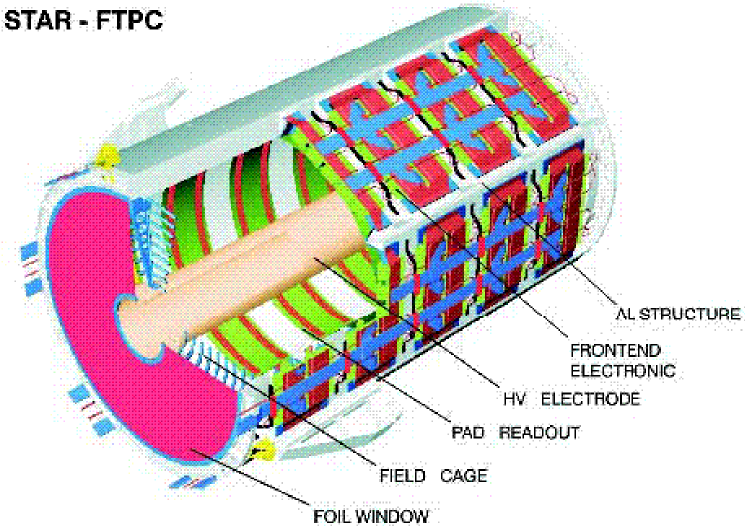

Figure 2.6: TSchematic diagram of an FTPC for the STAR experiment.

2.2.2 The STAR's Forward Time Projection Chamber (FTPC)

The Forward Time Projection Chambers (FTPC) were constructed to extend the acceptance of the main TPC [32]. They cover the pseudorapidity range of $2.5 < |\eta| < 4.0$ on both sides of STAR and measure momenta and production rates of charged particles as well as neutral strange particles. The FTPC illustrated in Fig. 2.6 is a cylindrical structure, 75 cm in diameter and 120 cm long, with a radial drift, and readout chambers located in 5 rings on the outer cylinder surface. Each ring has two padrows and is subdivided azimuthally into 6 readout chambers. The radial drift field, perpendicular to the magnetic field, was chosen to improve the two-track separation in the region close to the beam pipe where the particle density is highest. The field cage is formed by the inner HV-electrode, a thin metalized plastic tube, and the outer cylinder wall at ground potential. The field region at both ends is closed by concentric rings. The front-end electronics, which amplifies, shapes, and digitizes the signals, is mounted on the back of the readout chambers. Each particle trajectory is sampled up to 10 times. The ionization electrons are drifted to the anode sense wires and the induced signal on the adjacent cathode surface is read out by 9600 pads. The filled gas is a mixture of 50% Ar and 50% CO2.

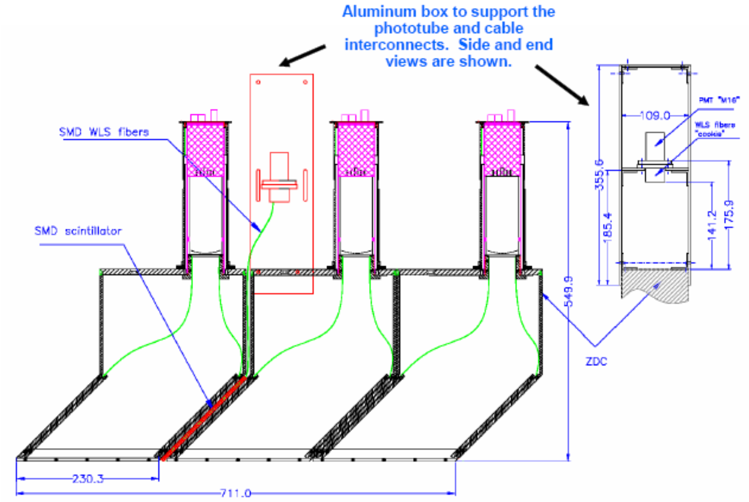

Figure 2.7: The SMD fits between the baseline ZDC modules.

The reconstruction of tracks in FTPC proceeds in two steps. The first step is to calculate the track points (cluster finding) from the charge distribution measured by the pads. In the second step (track finding), these track points of different padrows are grouped to tracks. Using the magnetic field map, the up to ten position measurements per track are then used to fit the momentum. The FTPCs obtain a position resolution of 100μm, a two-track separation of 1 - 2 mm, a momentum resolution between 12% and 15%, and overall reconstruction efficiency between 70% and 80%.

2.2.3 The STAR's Shower Maximum Detector inside the Zero Degree Calorimeters (ZDC-SMD)

The STAR ZDCs in their baseline form provide a signal that is correlated with the number of spectator neutrons produced in the collision. An upgrade that provides some information about the event-by-event pattern of transverse momentum among these neutrons opens up enhanced physics capabilities. In the subsections below, we discuss four areas of STAR physics where this new information is of significant value.

The ZDC-SMDswere be placed between the first and second modules of the ZDCs, seen Fig. 2.7. The SMD is an 8 channel by 7 channel hodoscope that sits directly on the face of the 2nd ZDC module, shown in Fig. 2.8. The hodoscope is made with strips

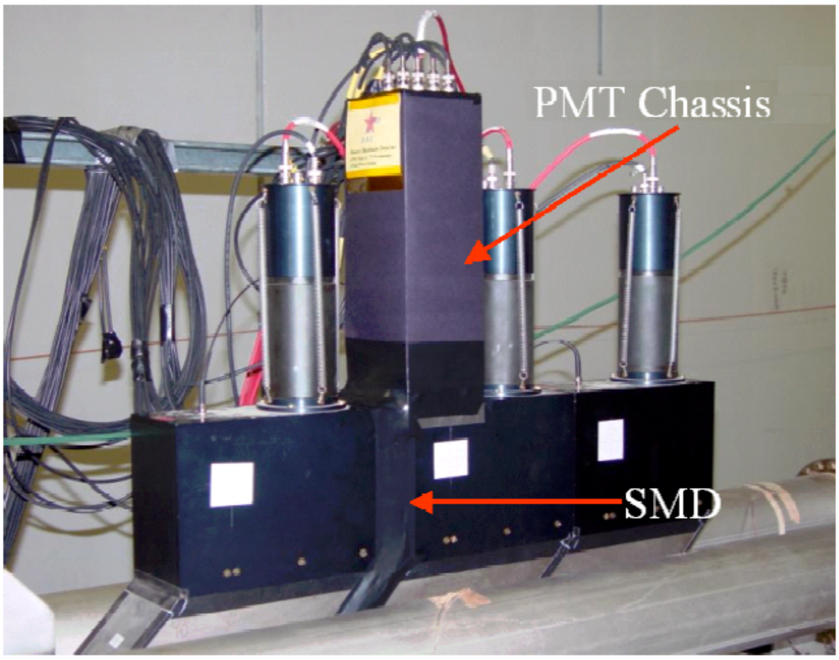

Figure 2.8: A ZDC-SMD module shown installed at STAR.

of scintillating plastic that are laid out in an X-Y pattern, with 21 strips having their long axes vertical and 32 strips having their long axes horizontal. The cross section of each strip is approximately an equilateral triangle with an apex-to-base height of 7 mm, shown in Fig. 2.9. A hole running axially along the center of each triangle allows the insertion of a 0.83 mm wavelength-shifting fiber which is used to collect and transport the scintillation light. Individual triangular strips are wrapped with 50 μm aluminized mylar to optically isolate them from their neighbors. The wrapped scintillator strips are then epoxied between two G-10 sheets to form a plane. Each slat aligned in the vertical direction consists of three strips, and the corresponding three fibers are joined to make one channel, and routed to the face of a 16-channel segmented cathode phototube conveniently located in a chassis above the SMD. The slats aligned in the horizontal direction are each made up of four strips and their fibers. The overall dimensions of the hodoscope are approximately 2 cm × 11 cm × 18 cm.

The chassis to support the phototube is a simple aluminum structure that is designed to be sturdy and to bear the load of the phototube and the 16 cables hanging off the tube. It also supports the weight of the HV and BNC cables that go to the electronics

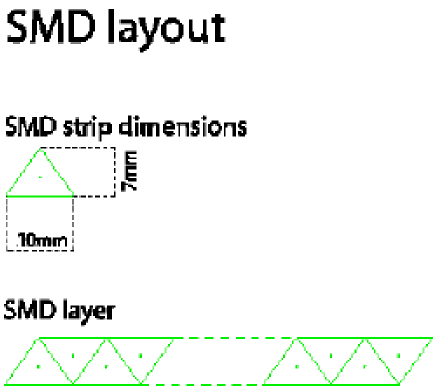

Figure 2.9: The SMD planes are built-up from scintillator strips with triangular cross section.

racks on the STAR detector. The design of the chassis, hodoscope, and phototube mounting are identical to the design that was used in PHENIX by Sebastian White and his collaborators during run III. The phototube is a 16-channel multi-anode PMT with a conventional resistive base (Hamamatsu H6568-10 [35]). The tube requires DC at -0.75 kV and it uses sixteen 50 ohm BNC cables for output. The sixteenth channel is a “sum” output. The electronics for the readout of the phototube were taken from spares for the STAR Central Trigger Barrel.

The possible impact on STAR was an important consideration at the time of the ZDC-SMD proposal. The primary change to the existing apparatus was that the 2nd and 3rd ZDC modules were moved away from STAR by about 2 cm in order to create a gap between modules 1 and 2. All other ZDC locations and the alignment with the beam stayed the same. The gap was used for the installation of the SMD. The SMD itself is approximately 1.5 cm of plastic and 2 mm of G-10 tilted on a 45 degree angle. This puts about 3 g/cm^2 of material in the path of neutrons coming from the interaction point. This amount of material is negligible compared to the $>$ 270 g/cm^2 of Tungsten and plastic in each ZDC module which comes before and after the SMD. Perhaps more important is the fact that ZDC modules 2 and 3 have moved away from module 1. This means they will be sampling the neutron-induced showers at a slightly greater depth in the shower. This change was insignificant because the ZDCs are calibrated annually and the change in performance of the ZDCs was below the rms of the calibration error.

CHAPTER 3

Analysis Methods

In this chapter, analysis details of directed flow from charged hadrons, p, $\bar{p}$,K_s^0, Λ and $\bar{\Lambda}$'s directed flow in Au+Au collisions at $\sqrt{s_{NN}}$ = 62 GeV and $\sqrt{s_{NN}}$ = 200 GeV are measured by the STAR experiment in Run 4, Run5 and Run7. The data-sets and cuts are shown, including the tracks selection from TPC and FTPC, the reconstruction of K_S^0, Λ, $\bar{\Lambda}$. The event plane reconstruction, the analysis methods for v_1 measurement.

3.1 Directed Flow from Au + Au Collisions at $\sqrt{s_{NN}}$ = 200 GeV in Run 7

3.1.1 Data-set and Cuts

In total fifty-four million events for Au+Au collisions at $\sqrt{s_{NN}}$ = 200 GeV are used in this study, all taken by a minimum-bias trigger with STAR detector during the RHIC seventh run in year 2007.

Trigger Setup Name	Production	Vertex Cut	Trigger ID	Events No.
ProductionMinBias	P08ic	$\lvert V_z\rvert < 30$ cm	200001, 200003, 200013	45 M
Production2	P08ic	$\lvert V_z\rvert < 30$ cm	200001, 200003, 200013	9 M

Table 3.1: The trigger and events selection in minimum bias Au+Au collisions at $\sqrt{s_{NN}}$ = 200 GeV in Run7.

The main trigger detector used is the vertex position detector (VPD) [29]. The trigger and event selection are list in Table 3.1. Particle Identification (PID) of charged particles is achieved by measuring energy loss (dE/dx) by ionization inside STAR's Time Projection Chamber (TPC) [31], together with the measurement of the momentum via TPC tracking. The centrality definition of an event was based on the number of charged tracks in the TPC with track quality cuts: $|\eta|$ <0.5, a Distance of Closest Approach (DCA) to the vertex less than 3 cm, and 10 or more fit points. In the analysis, events are required to have vertex z within 30 cm from the center of the TPC, and additional weight is assigned to each event in the analysis accounting for the uniform VPD trigger efficiency in the vertex z direction for different centrality classes. This Global reference multiplicity called gRefMult is showed in Fig. 3.1. It is consistent with the ideal multiplicity distribution from Monte-Carlos(MC) Glauber calculation which scaled by a constant factor. The raw distribution of the gRefMult is shown by blue line Fig. 3.2 and the black line is the gRefMult distribution after correction. The main difference of gRefMult is in the peripheral collision.

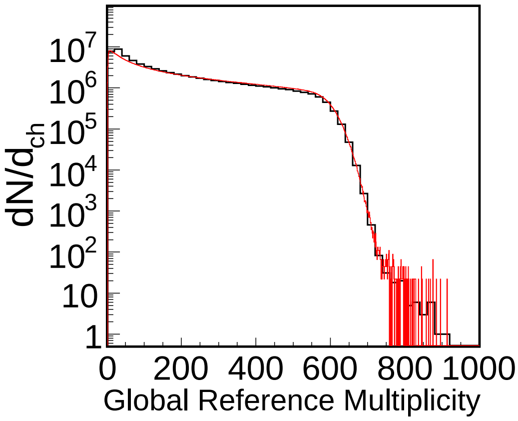

Figure 3.1: The Global reference multiplicity (gRefmult) distribution(the black line) from Au+Au collisions at $\sqrt{s_{NN}}$ = 200 GeV. The red line present the ideal multiplicity distribution from MC Glauber calculation. It is scaled by a constant factor.

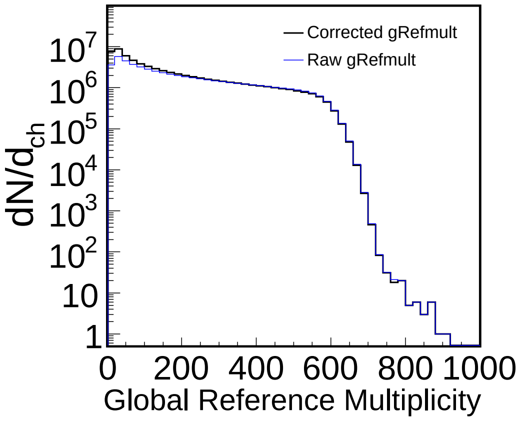

Figure 3.2: The Global reference multiplicity (gRefmult) distribution(the black line) after correction from Au+Au collisions at $\sqrt{s_{NN}}$ = 200 GeV. The blue line presents raw Global reference multiplicity distribution before correction.

The remaining issues are biases on multiplicity distribution introduced by the main online Vertex Position Detector(VPD) trigger-setup (200013). The biases come from two origination: 1)the VPD is more efficient at triggering on central events relative to peripheral over the full range in Z direction. This leads to a general deficit in peripheral events for a given data sample. 2)There is a centrality dependence of the VPD's online Z resolution. This is worse for peripheral events relative to central. Since the trigger-setup (200013) insisted events events fall within the inner tracking acceptance, for example, with an online cut of $|V_z| < 5$ cm, the resolution issue reflect that events at the higher $|V_z|$'s are more likely to peripheral whereas the events at lower $|V_z|$'s could be central. The V_z dependent biases in multiplicity distribution require a re-weighting correction to be applied for all analysis. The correction has to be applied as a function of V_z in 2 cm bins for acceptance reasons. In a given V_z bin, the weights are determined by normalizing the 1D global reference multiplicity distribution by the number of events with global reference multiplicity > 500. Then the ideal multiplicity distribution from MC Glauber calculation then has to be divided by the normalized global reference multiplicity distribution to calculate the weights.

The centrality definition *v.s.* the geometric cross section according to the global reference multiplicity for Au+Au collisions are listed in Table. 3.2

Centrality Bin	Global Reference Multiplicity	Geometric Cross Section
1	10-20	$70-80\%$
2	21-38	$60-70\%$
3	39-68	$50-60\%$
4	69-113	$40-50\%$
5	114-177	$30-40\%$
6	178-268	$20-30\%$
7	269-398	$10-20\%$
8	399-484	$5-10\%$
9	≥485	$0-5\%$

Table 3.2: Centrality definition in Au+Au collisions at $\sqrt{s_{NN}} = 200$ GeV fron Run VII data sample.

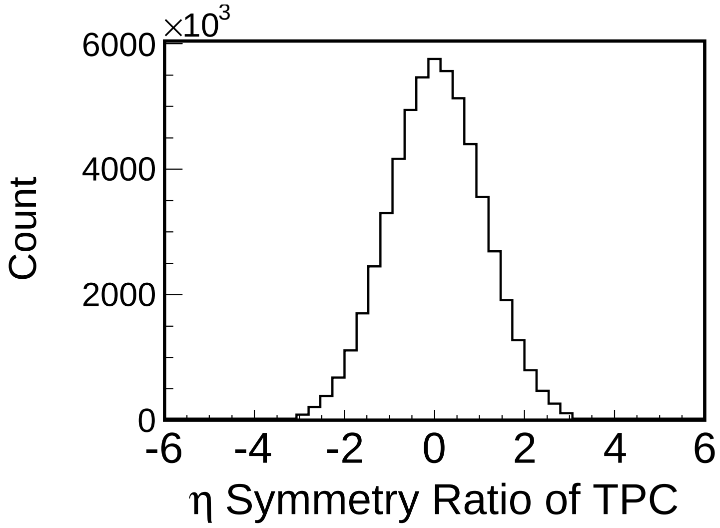

Figure 3.3: The η symmetry ratio of TPC from Au+Au collisions at $\sqrt{s_{NN}} = 200$ GeV.

3.1.2 Track Selections

The tracks used in analysis from TPC and FTPC are listed in Table. 4.1. The η symmetry cuts are necessary for the directed flow studies since there are some asymmetry in particles' η distribution in particular run days. To avoid these bad run, the η symmetry cuts are applied. The $N_{\eta>0}$(TPC) and $N_{\eta<0}$(TPC) stands for the number of the selected tracks from TPC in the negative η and positive η separately. It is defined as:

$$\sqrt{N_{\eta>0}(TPC) + N_{\eta<0}(TPC)} \times (\frac{N_{\eta>0}(TPC) - N_{\eta<0}(TPC)}{N_{\eta>0}(TPC) + N_{\eta<0}(TPC)} + 0.003 \times Vz) \qquad (3.1)$$

Here Vz is the vertex in the z direction, $0.003 \times Vz$ is used for the correction for acceptance. The distribution of η symmetry ratio from TPC is shown in Fig. 3.3.

The $N_{\eta>0}$(FTPC) and $N_{\eta<0}$(FTPC) is presented as the number of the selected tracks from FTPC in the negative η and positive η separately. It is defined as:

$$\sqrt{N_{\eta>0}(FTPC) + N_{\eta<0}(FTPC)} \times (\frac{N_{\eta>0}(FTPC) - N_{\eta<0}(FTPC)}{N_{\eta>0}(FTPC) + N_{\eta<0}(FTPC)}) \qquad (3.2)$$

Particle Identification (PID) of charged particles is achieved by measuring energy loss (dE/dx) by ionization inside STAR's Time Projection Chamber (TPC) [31], together with the measurement of the momentum via TPC tracking. The transverse momentum p_T for protons are required to be larger than 400 MeV/c, and DCA are required to be

	Tracks used for TPC	Tracks used for FTPC
No. of fit hits	[15,50]	[5,11]
Global track's DCA (cm)	(0,2.0]	(0,2.0]
No. of the fit hitsNo. of the possible hits	[0.52,1.05]	> 0.52
$\|\eta\|$	1.3	[2.5,4.0]
η symmetry	[-3.0,3.0]	[-5.0,5.0]

Table 3.3: racks selection from TPC and FTPC in Au+Au collisions at $\sqrt{s_{NN}} = 200$ GeV.

less than 1 cm, in order to avoid including background protons which are created in the beam-pipe. The same cuts are applied to anti-protons as well to ensure a fair comparison with protons. The high-end of the p_T cut is 1 GeV/c where protons and pions have the same energy loss in the TPC and thus become indistinguishable. For pions and kaons, momentum range are 0.15 - 0.75 GeV/c and 0.2 - 0.6 GeV/c, respectively.

3.1.3 V0 Reconstriction

The V0 particles such as K_s^o, Λ and $\bar{\Lambda}$ are reconstructed by their daughter particles which are identified by TPC. Their weak decay channels are $K_s^0 \to \pi^+ + \pi^-$, $\Lambda \to p + \pi^-$ and $\bar{\Lambda} \to \bar{p} + \pi^+$. Their properties are summarized in Table 3.4

Particle Type	Decay Channel	Branching Ratio (%)	$c\tau$ (cm)	Mass (GeV/c^2)
K_S^0	$\pi^+ + \pi^-$	68.95 ± 0.14	2.68	0.497
$\Lambda(\bar{\Lambda})$	$p + \pi^-$ $(\bar{p} + \pi^+)$	63.9 ± 0.5	7.89	1.115

Table 3.4: K_S^0, $\Lambda(\bar{\Lambda})$ weak decay properties.

Since there are many fake vertex among the reconstructed decay vertex known as the combinatorial background, such as the misidentification of the daughter tracks, the decay vertex close to the primary vertex and a pair of daughter tracks from different V0s.

The decay geometry is utilized to reject the fake V0 pairs. From the line 3 of the table 3.4, $c\tau$ of K_S^0 and $\Lambda(\bar{\Lambda})$ is 2.68 cm and 7.89 cm so that most of them will decay

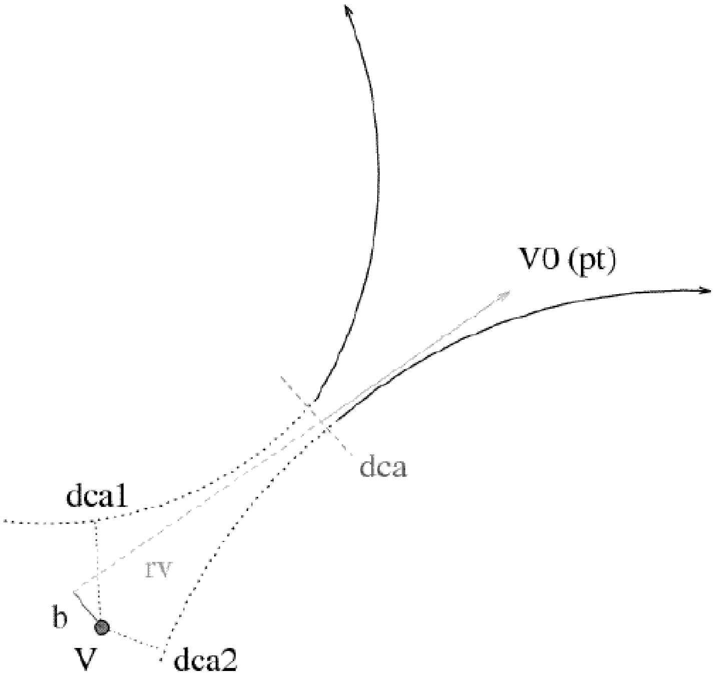

Figure 3.4: The V0 decay topology from figure in Ref. [36].

within 2 cm radius in the TPC. The decay vertex is in the order of a few centimeter further than the primary vertex with several hundreds microns. Thus the decay vertex and the primary vertex are well separated. The picture of the decay topology is shown in Fig. 3.4. The V0 is named from the topology as the capital letter "V" and the zero charge. The DCA (distance of the closet approach) between two daughter tracks is used to determine the point of the decay vertex. The fake decay vertex should distribute at larger DCA than the real decay vertex. Dca1 or Dca2 is the DCA of the daughter to the primary vertex. The primary tracks should distribute at smaller value than the decay daughters. The b stands for the DCA between the primary vertex to the V0 momentum direction ($b = 0$ ideally). The rv represents the V0 decay length that V0 travels distance in TPC.

The optimized cuts of K_S^0, $\Lambda(\bar{\Lambda})$ in Au+Au collisions at $\sqrt{s_{NN}} = 200$GeV are listed in Table 3.5 and 3.6 respectively. These cuts are used for the v_1 invariant mass method analysis, shown in the next section. The signal over background ratio will be significantly enhanced by these cuts.

There are another tight cuts used for K_S^0, $\Lambda(\bar{\Lambda})$ listed in Table 3.7. These cuts are used in the standard event plane method. The invariant mass distribution for K_S^0, $\Lambda$and $\bar{\Lambda}$. The mass window for being a K_S^0(red band), Λ(blue band) and $\bar{\Lambda}$(dark green band) are [0.48,0.51] and [1.11,1.12] respectively.

p_T (GeV/c)	< 0.8	0.8-3.6	> 3.6
π DCA to primary vertex (cm)	> 1.5	> 1.0	> 0.5
DCA between daughters (cm)	< 0.7	< 0.75	< 0.5
DCA from primary vertex to V0	< 0.7	< 0.75	< 0.5
decay length (cm)	4-150	4-150	10-120

Table 3.5: Cuts selection criteria for K_S^0 in Au+Au collisions at $\sqrt{s_{NN}} = 200$ GeV.

p_T (GeV/c)	< 0.8	0.8-3.6	> 3.6
π DCA to primary vertex (cm)	> 2.5	> 2.0	> 1.0
p DCA to primary vertex (cm)	> 1.0	> 0.75	> 0
DCA between daughters (cm)	< 0.7	< 0.75	< 0.4
DCA from primary vertex to V0	< 0.7	< 0.75	< 0.75
decay length (cm)	3.5-150	3.5-150	10-125

Table 3.6: Cuts selection criteria for $\Lambda(\bar{\Lambda})$ in Au+Au collisions at $\sqrt{s_{NN}} = 200$ GeV.

daughters(π,p) DCA to primary vertex (cm)	> 0.8
DCA between daughters (cm)	< 0.8
DCA from primary vertex to V0	< 0.5
decay length (cm)	> 6.0

Table 3.7: Cuts selection criteria for K_S^0 ,Λ, $\bar{\Lambda}$ in Au+Au collisions at $\sqrt{s_{NN}} = 200$ GeV.

3.1.4 The Estimation of the Reaction Plane and the Resolution

The anisotropic flow describes the azimuthal momentum distribution of the particle emission with respect to the reaction plane. The reaction plane is defined by the initial

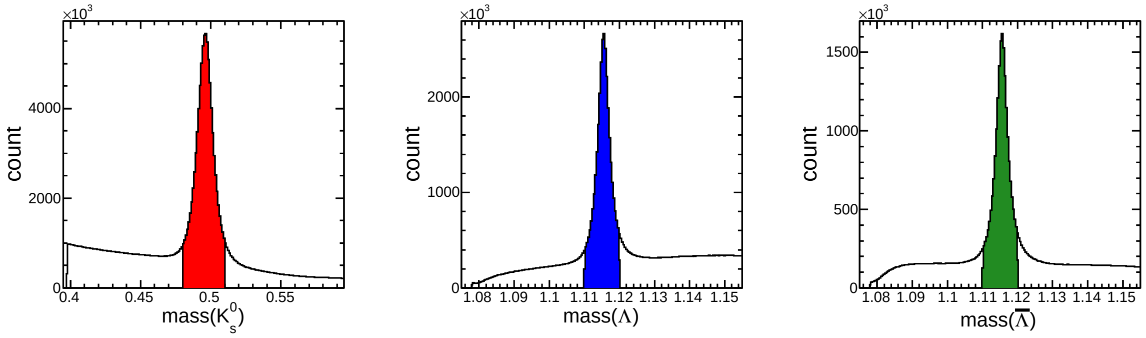

Figure 3.5: The invariant mass distribution for K_S^0, $\Lambda$and $\bar{\Lambda}$for Au+Au collisions at $\sqrt{s_{NN}} =$ 200GeV.

beam direction and the impact parameter-b (x-z plane). In the event-by-event analyse, the reaction plane need to be estimated. The estimated reaction plane is called event plane.

The anisotropic flow is usually quantified by the Fourier expansion of the particle emission azimuthal angle measured with respected to the reaction plane [19]:

$$E\frac{d^3N}{d^3p} = \frac{1}{2\pi}\frac{d^2N}{p_T dp_T dy}(1 + \sum_{n=1}^{\infty} 2v_n \cos[n(\phi - \psi_r)]\}) \tag{3.3}$$

where ϕ denotes the azimuthal angle of an outgoing particle, ψ_r is the orientation of the (true) reaction plane angle, and n denotes the harmonic. The sine terms in Fourier expansions vanish due to the reflection symmetry with respect to the reaction plane. The various coefficients in this expansion can be defined as:

$$v_n = \langle\cos[n(\phi - \psi_r)]\rangle \tag{3.4}$$

where $\langle\rangle$ indicates an average over all particles in all events.

Experimentally, the true reaction plane angle is unknown, we have to get the event plane. The event plane can be determined independently for each harmonic of the anisotropic flow. The nth harmonic event flow vector $\overrightarrow{Q_n}$ and the event plane angle ψ_n are defined by the formulas:

$$Q_n \cos(n\psi_n) = X_n = \sum_i w_i \cos(n\phi_i), \tag{3.5}$$

$$Q_n \sin(n\psi_n) = Y_n = \sum_i w_i \sin(n\phi_i), \tag{3.6}$$

or

$$\psi_n = \frac{1}{n} \arctan \frac{\sum_i w_i \sin(n\phi_i)}{\sum_i w_i \cos(n\phi_i)} \tag{3.7}$$

where ϕ_i denotes the azimuthal angle of the ith particle, and the w_i are weights to optimize the event plane resolution as good as possible. The weights are usually assigned with the transverse momentum (called the p_T weight), or the magnitude of the selected particles's pseudo-rapidity(called the η weight). Sometimes it uses the ϕ weight, the inverse of the raw ϕ distribution with proper normalization so that its average equals unity. This weighting allows us to compensate for the “blind spots” in the azimuthal of the track-based detector, such as the Forward Time Projection Chamber(FTPC). In our directed flow analysis, the particles in the forward region have stronger directed flow, thus they are assigned heavier weight than the particle in the mid-rapidity by the η weight. And the ϕ weight work well if the detecting efficiency is not too far from the being uniform in azimuthal.

However it is not uncommon that during data taking, the detector performance varies dramatically as a function of time, and sometimes it even suffers from severe electronic loss, which results in a big detecting inefficiency that cannot be compensated by weighting. As a consequence of that, the event plane after the weighting procedure might still be not flat. To make a further correction, we use the so-called shifting method [30] to make it flat. It makes corrections to the event plane angle itself to get the flatten event plane distribution. The corrected new angle are

$$n\psi_n^{'} = n\psi + n\Delta\psi \tag{3.8}$$

where $n\Delta\psi$ is written in the form

$$n\Delta\psi = \sum_{i=1}^{i_{max}}[A_i\cos(in\psi) + B_i\sin(in\psi_n)] \tag{3.9}$$

we have usually taken $i_{max} = \frac{4}{n}$ for $n = 1, 2$. Requiring the vanishing of the ith Fourier moment of the new distribution, the coefficients A_i and B_i can be evaluated by the original distribution

$$A_i = -\frac{2}{i}\langle\sin(in\psi_n)\rangle, \tag{3.10}$$

$$B_i = \frac{2}{i}\langle\cos(in\psi_n)\rangle, \tag{3.11}$$

$$n\psi_n^{'} = n\psi + \sum_{i=1}^{i_{max}}\frac{2}{i}[-\langle\sin(in\psi_n)\rangle\cos(in\psi) + \langle\cos(in\psi_n)\rangle\sin(in\psi_n)]. \tag{3.12}$$

Due to the small values of A_i and B_i (typically of the order of a few percent), thus this kind of the flatten distribution does not have any effect on the event plan resolution. This flatten procedure removes possible trigger biases due to the dead channels, imperfect calibration, or any other asymmetry.

We apply the same procedure to both FTPC east event plane and FTPC west event plane. The event plane from east FTPC and west FTPC of Au+Au collisions at $\sqrt{s_{NN}}$ = 200 GeV is shown in Fig. 3.6

The full event plane vector is a sum of the two event plane vectors (east and west) with the latter being flipped by 180°. The flip comes from the fact that directed flow of forward-going particles has an opposite sign than that of backward-going particles. The full event plane is then subsequently flattened by shifting.

Different from FTPC which measures tracks of particles, the STAR' shower maximum detector at zero degree calorimeters(ZDC-SMDs) measures energy deposited by hits. It is located at the $|\eta| > 6.3$ and measure the sideward deflection of the spectator neutrons. Since it is close to the beam rapidity thus have minimum contribution from the non-flow

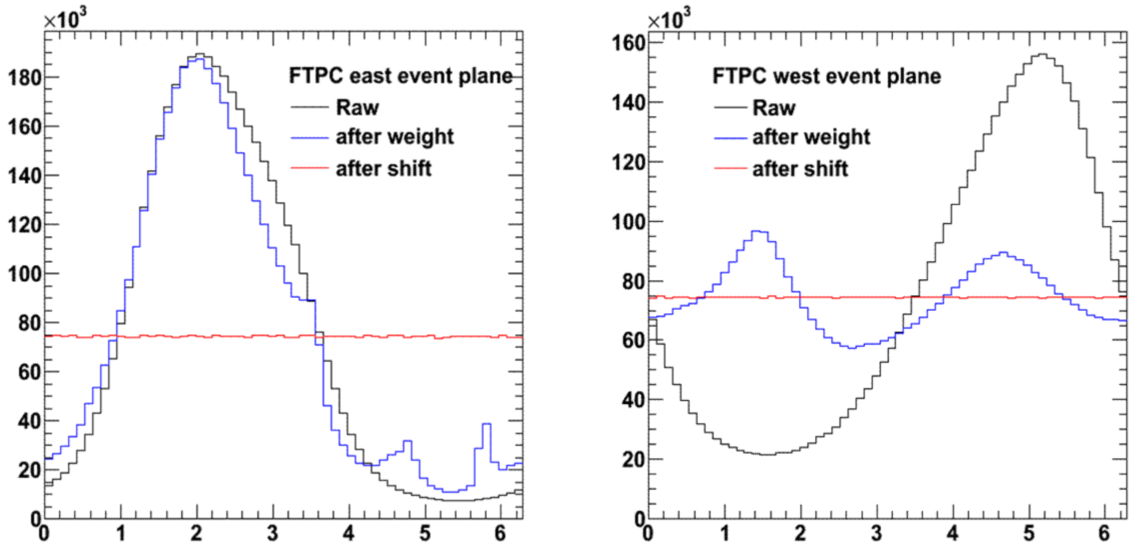

Figure 3.6: The azimuthal angle distribution of the 1st-order event plane from FTPC in Au+Au collisions at $\sqrt{s_{NN}} = 200$ GeV: east sub-event plane(left panel), west sub-event plane(right panel). The color lines represent the event plane distribution from procedure: the raw distribution(black lines), the distribution after η and ϕ weights, the final distribution after shift.

effect. Here we only consider the first-order event plane. The harmonic event flow vector $\overrightarrow{Q}$ and the 1st order event plane angle ψ_n are changed to other way:

$$Q_n \cos(n\psi) = X = \sum_{i=1}^{7} w_i x_i, \tag{3.13}$$

$$Q_n \sin(n\psi) = Y = \sum_{i=1}^{8} w_i y_i, \tag{3.14}$$

or

$$\psi_n = \arctan \frac{\sum_{i=1}^{7} w_i x_i}{\sum_i w_i y_i} \tag{3.15}$$

where the x_i is the fixed positions for the seven vertical slats while the y_i is the fixed positions for the eight horizontal slats. The w_i are calculated from the energy depositions(ADC signals) in the ith element, defined as:

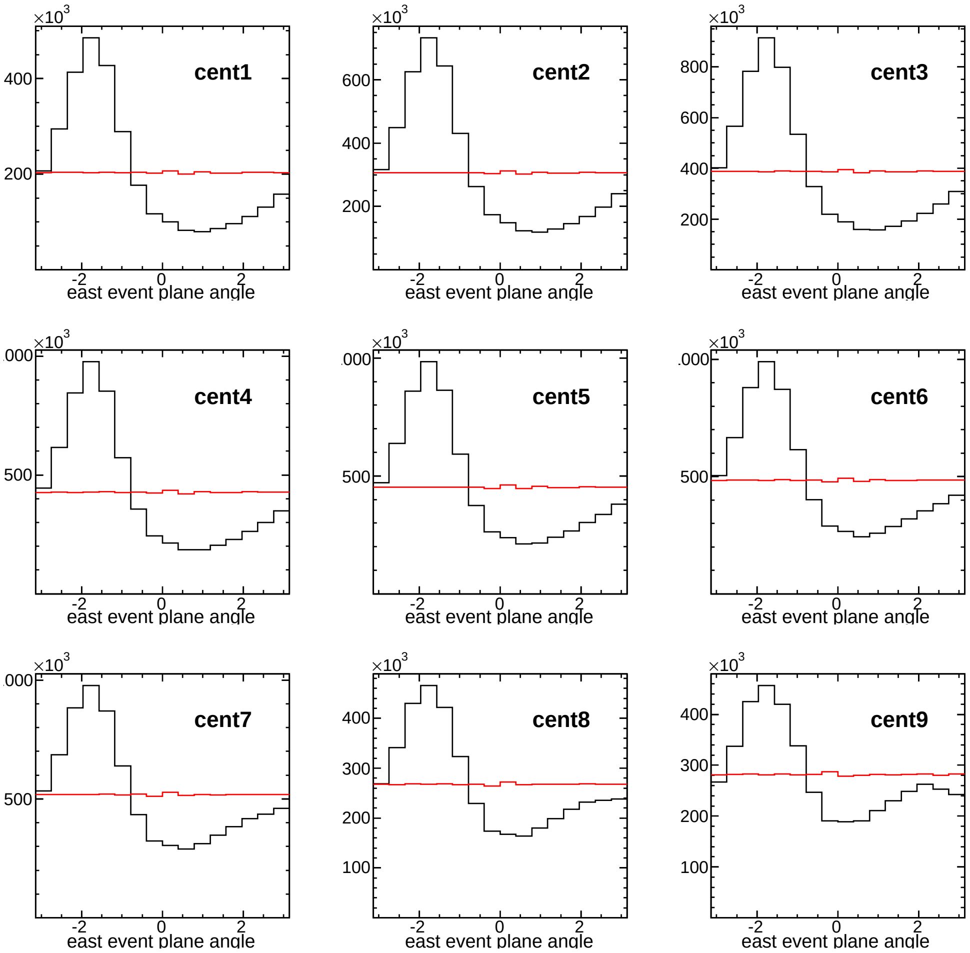

Figure 3.7: The ZDCSMD east event plane distribution from the peripheral(top left) to the central collisions(bottom right).

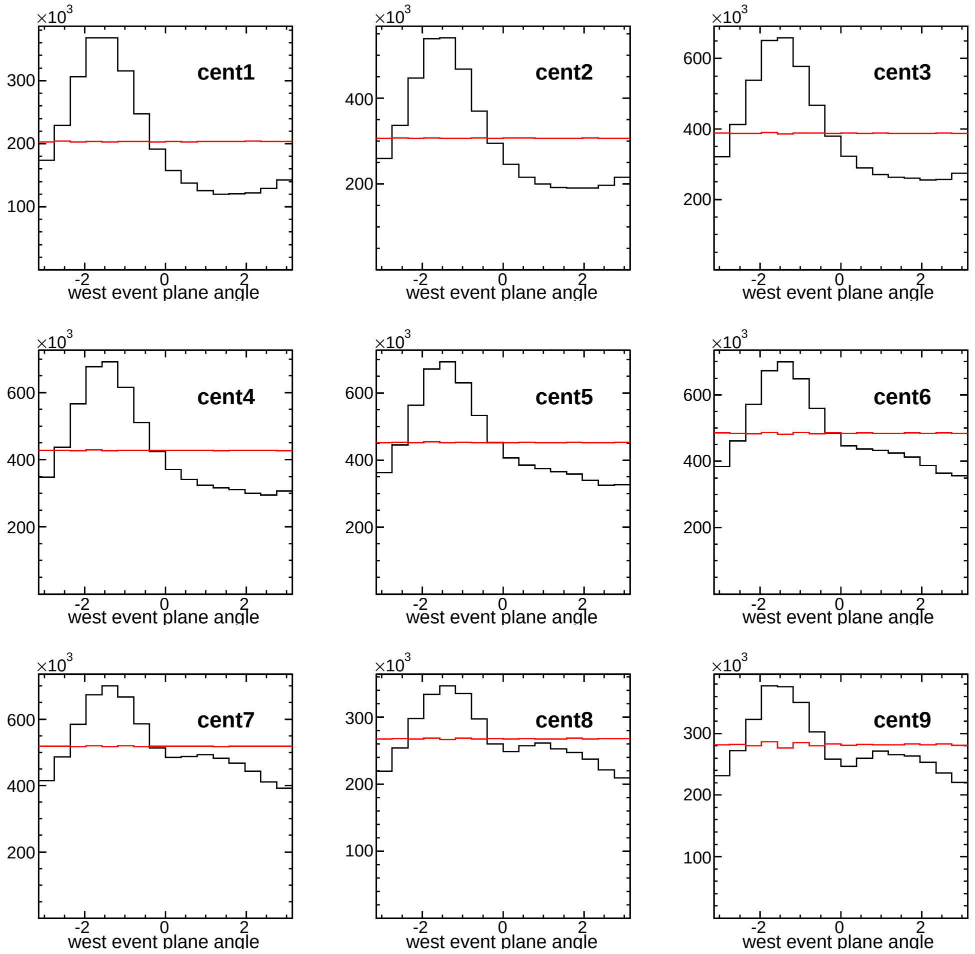

Figure 3.8: The ZDCSMD west event plane distribution from the peripheral(top left) to the central collisions(bottom right).

$$w_i = ADC_i/(\sum_{i=1}^{7or8} ADC_i) \tag{3.16}$$

Then we applied the shifting method for ZDC-SMD event planes because there is no track-wise information for us to carry out the ϕ weighting procedure. Similarly to the case for FTPC, the east and west ZDC-SMD event planes were flattened independently(shown in Fig. 3.7 and Fig. 3.8), and then the full event plane(shown in Fig. 3.9) was reconstructed from two flattened planes and subsequently flattened.

resolution, the coefficients in the Fourier expansion of the azimuthal distribution with respect to the real reaction plane can be evaluated,

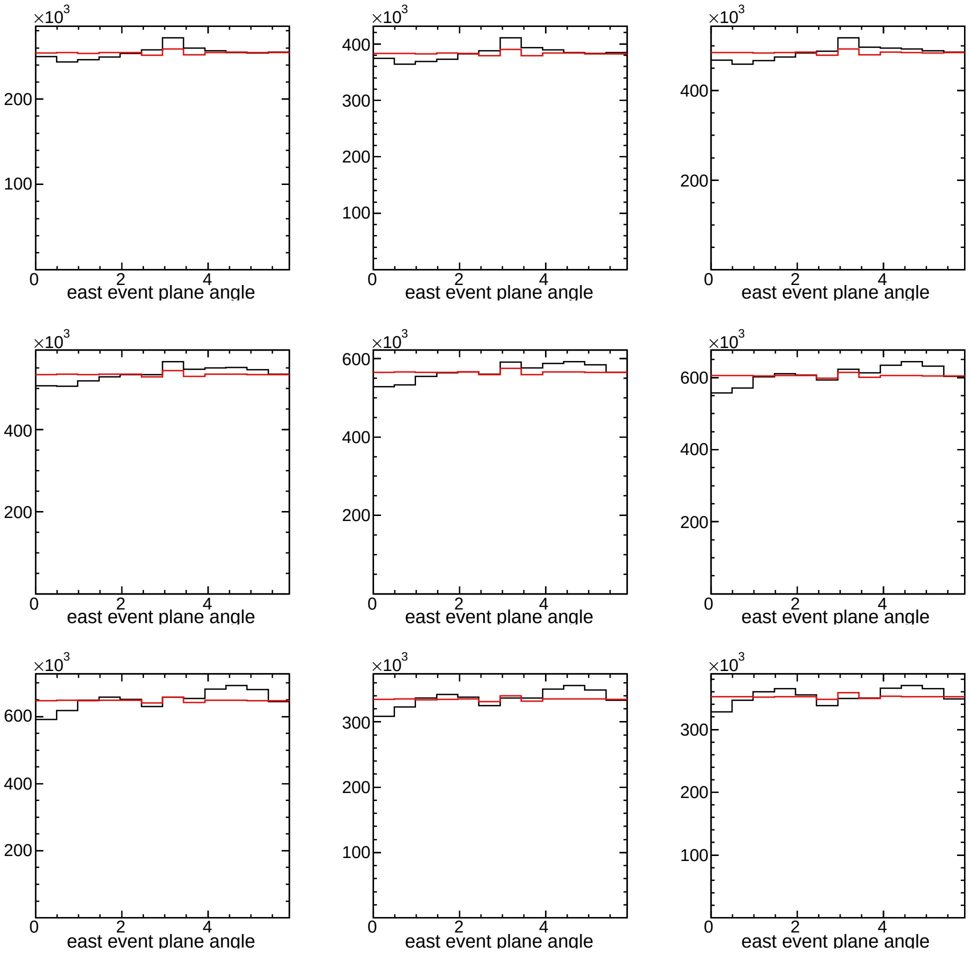

Figure 3.9: The ZDCSMD full event plane distribution from the peripheral(top left) to the central collisions(bottom right).

$$v_n = v_n^{obs} / \langle \cos(n(\psi_n - \psi_r)) \rangle \tag{3.17}$$

In our analysis, we use the sub-event plane from east and west ZDC-SMD, the correlation between these sub-event plane angle can be written as,

$$\langle \cos(\psi^{east} - \psi^{west}) \rangle = \langle \cos(\psi^{east} - \psi_r) \rangle \times \langle \cos(\psi^{west} - \psi_r) \rangle \tag{3.18}$$

Assuming that

$$\langle \cos(\psi^{east} - \psi_r) \rangle = \langle \cos(\psi^{west} - \psi_r) \rangle \tag{3.19}$$

So

$$\langle \cos(\psi^{sub} - \psi_r) \rangle = \sqrt{\langle \cos(\psi^{east} - \psi^{west}) \rangle} \tag{3.20}$$

The full event plane can be got from the equation

$$\langle \cos(\psi_{full} - \psi_r) \rangle = \frac{\sqrt{\pi}}{2\sqrt{2}} \chi \exp(-\frac{\chi^2}{4}) \times [I_0(\chi^2/4) + I_1(\chi^2/4)] \tag{3.21}$$

where $\chi = v/\sigma = v\sqrt{2N}$ for number flow, which can be exacted from the Fig. 3.10 [19] when $k = 1$. I_ν is the ν-order modified Bessel function. More detail can be found in Ref. [19].

The 1st-order event plane resolution is a number between 0 and unity depending on both the strength of the flow signal and the number of particles detected. The larger the resolution the easier the flow measurements. The Fig. 3.11 shows the 1st-order event plane resolution as function of centrality from Au+Au 200GeV. The 1st-order event plane resolution from ZDCSMD in the Run 7 is consistent with the Run 4 in the central and mid-central collisions. Although these are some differences in centrality 30%-80%, it will not effect our v_1 results(see Fig. 4.1). The resolution of 1st order event plane reconstructed by the FTPC in Run7 is much small than that from the ZDCSMD. Thus, we will only use 1st order event plane from the ZDCSMD.

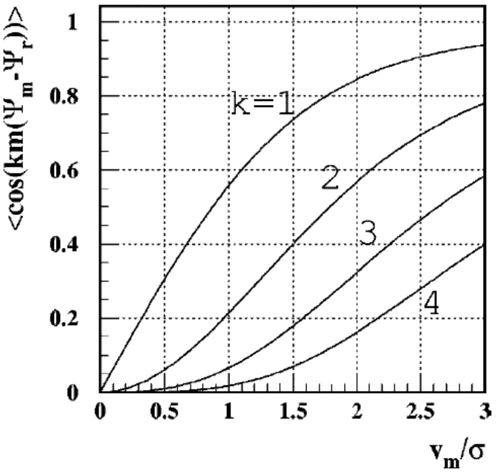

Figure 3.10: The event plane resolution as function of $\chi_m = v_m/\sigma$ from the nth ($n = km$) harmonic of the particle distribution with respect to the mth harmonic plane. For the 1st order event plane, $n = 1 = k = m$.

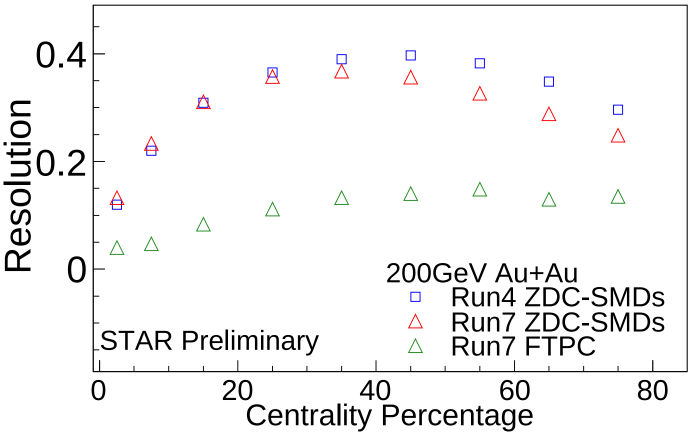

Figure 3.11: The 1st-order event plane resolution as function of centrality from Au+Au 200GeV: the 1st-order event plane reconstructed by ZDCSMD from Run4 data(blue squares), 1st-order event plane reconstructed by ZDCSMD from Run7 data(red triangles), the 1st-order event plane reconstructed by FTPC from Run7 data(dark green triangles).

3.1.5 The Standard Event Plane Method

As discussed in the reaction of the reaction plane section, the 1st order event plane ψ here is determined from the ZDCSMD.

$$v_1 = \frac{\langle \cos(\phi - \psi_1) \rangle}{Res(\psi_1)} \tag{3.22}$$

where ϕ and ψ_1 denotes the azimuthal angle of the particle and the 1st-order event plane, respectively. $Res(\psi_1) = \langle \cos(\psi_1 - \psi_r) \rangle$ represents the resolution of the 1st-order event plane. This standard event plane method are used in charged hadron, proton, antiproton, kaon, pion analysis. So it is directed flow analysis about K_S^0, $\Lambda(\bar{\Lambda})$ with the tight V0 cuts selection criteria. The tight cut minimum the background contamination as well as subtract the signal. The v_1 versus m_{inv} method are introduced below, and the directed flow results of K_S^0, $\Lambda(\bar{\Lambda})$ with the tight V0 cuts are regarded as systematic errors(discussed in next section).

3.1.6 v_1 versus m_{inv} Method

The v_1 versus m_{inv} method is useful to measure the directed flow of strange hadrons, K_S^0, $\Lambda(\bar{\Lambda})$. Their candidates are identified on statistical basis. The invariant mass(m_{inv}) distribution contained some remaining combinatorial background for K_S^0, $\Lambda(\bar{\Lambda})$. The goal of this method is to get the pure directed flow signal of K_S^0, $\Lambda(\bar{\Lambda})$ as possible. The primary way of this method is based on the equation as following:

$$v_{obs}^{Sig+Bg}(m_{inv}) = v_{obs}^{Sig} \frac{Sig}{Sig + Bg}(m_{inv}) + v_{obs}^{Bg}(m_{inv}) \frac{Bg}{Sig + Bg}(m_{inv}) \tag{3.23}$$

As we know the combined (signal+background) v_1 as function of m_{inv} on the left side of this equation. On the right side of this equation, the ratio versus m_{inv} of the backgound over total (signal+background) can be calculated. The ratio versus m_{inv} of the signal over total (signal+background) can be calculated by

$$\frac{Bg}{Sig + Bg}(m_{inv}) = 1 - \frac{Sig}{Sig + Bg}(m_{inv}) \tag{3.24}$$

The only left $v_1^{Bg}(m_{inv})$ and v_1^{Sig} remain to be measured. Assume the v_1^{Bg} as a certain function of m_{inv}, the v_1^{Bg} can be finally extracted by fitting the $v_1^{Sig+Bg}(m_{inv})$.

To illustrate this method, the Fig. 3.12 gives an example about K_S^0 in Au+Au collisions at $\sqrt{s_{NN}}$ = 200 GeV. The panel (a) shows the invariant mass distribution of K_S^0 (signal+background). A 4th order polynomial fitting function is used to describe the background of K_S^0(the solid red line). The fitting line over the data is regarded the value if $\frac{Bg}{Sig+Bg}$, the $\frac{Sig}{Sig+Bg}$ can be got from the equation 3.24. The panel (b) presents the v_{obs} of K_S^0 candidates in red circle while the solid line is the fit of K_S^0 candidates with the equation 3.12. This fit also showed in the panel (c) in red line, together with K_S^0 signal (blue dot-dashed line) and background (red dotted line).

In order to get the reliable results, there are several trial technical ways to make the fitting reasonable. The fitting of the data points are required over a wide m_{inv} range. The ratio of $\frac{Bg}{Sig+Bg}$ is set to be 1 when the invariant mass region is far away from the peak. That is because there is only background contribution and the v_{obs}^{Sig+Bg} data points have strong constraints on v_{obs}^{Bg} at these areas. Within the given ratio of $\frac{Sig}{Sig+Bg}$ and $\frac{Bg}{Sig+Bg}$, the the v_{obs}^{Sig+Bg} data points from the invariant mass peak region restrict on v_{obs}^{Sig}.

3.2 Directed Flow from Au + Au Collisions at $\sqrt{s_{NN}}$ = 200 GeV and 62 GeV in Run 4

3.2.1 Data-set and Cuts

In total two million events for Au+Au collisions at $\sqrt{s_{NN}}$ = 200 GeV are used in this study, all taken by a minimum-bias trigger with STAR detector during the RHIC fourth run in year 2004.

Trigger Setup Name	Production	Vertex Cut	Trigger ID	Events No.
ProductionMinBias & LowMidHigh	P04ic	$\lvert V_z\rvert < 30$ cm	15007	2 M

Table 3.8: The trigger and events selection in minimum bias Au+Au collisions at $\sqrt{s_{NN}}$ = 200 GeV in Run4.

The trigger and event selection in Run4 are list in Table 3.1. The global tracks are

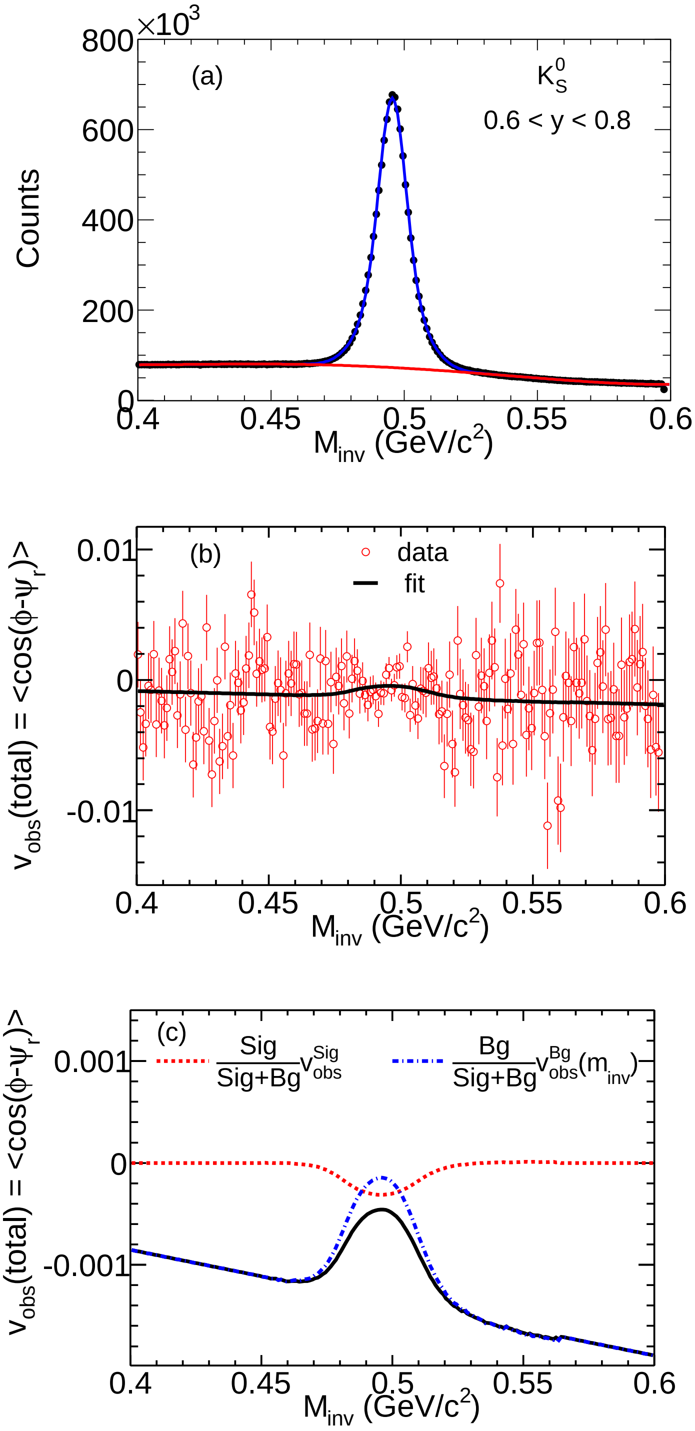

Figure 3.12: An example about $v_{obs}v.sm_{inv}$ method to exact v_{obs} of K_S^0.

defined as the helix fit to the TPC points one by one, and all the reconstructed global tracks determine the collision vertex. There is the other kind of the reconstructed tracks named as the primary tracks, they are defined by the TPC points along with the vertex. If there is no primary vertex, this events will be discarded. The centrality definition *v.s.* the geometric cross section according to the reference multiplicity for Au+Au collisions are listed in Table. 3.2. The TPC reference multiplicity is the number of the primary tracks which is with the fifteen or more points in the TPC within the absolute value of pseudo-rapidity less than 0.5 ($|\eta| < 0.5$), the distance of the closest approach (DCA) to the primary vertex(PV) is required less than 3 cm.

Centrality Bin	Multiplicity	Geometric Cross Section
1	14-31	$70-80\%$
2	31-57	$60-70\%$
3	57-96	$50-60\%$
4	96-150	$40-50\%$
5	150-222	$30-40\%$
6	222-319	$20-30\%$
7	319-441	$10-20\%$
8	441-520	$5-10\%$
9	≥520	$0-5\%$

Table 3.9: Centrality definition in Au+Au collisions at $\sqrt{s_{NN}} = 200$ GeV fron Run IV.

There about are 2 M events samples from Au+Au collisions at $\sqrt{s_{NN}} = 62.4$ GeV in Run 4 used in the analysis. All were obtained with minimum-bias trigger. The trigger selection and the cuts are listed in the Table 3.10. The centrality definition *v.s.* the geometric cross section according to the reference multiplicity for Au+Au collisions are listed in Table. 3.9. The tracks used in the reference multiplicity is the in same cuts as the Run 4.

Trigger Setup Name	Production	Vertex Cut	Trigger ID	Events No.
production62GeV	P04id	$\lvert V_z \rvert < 30$ cm	15007	5 M

Table 3.10: The trigger and events selection in minimum bias Au+Au collisions at $\sqrt{s_{NN}} =$ 62.4 GeV in Run4.

Centrality Bin	Multiplicity	Geometric Cross Section
1	9-20	$70 - 80\%$
2	20-38	$60 - 70\%$
3	38-65	$50 - 60\%$
4	65-102	$40 - 50\%$
5	102-154	$30 - 40\%$
6	154-222	$20 - 30\%$
7	222-313	$10 - 20\%$
8	313-373	$5 - 10\%$
9	≥373	$0 - 5\%$

Table 3.11: Centrality definition in Au+Au collisions at $\sqrt{s_{NN}} = 62.4$ GeV fron Run IV.

Cuts	V^0_s)
Distance of the closest approach(DCA) between daughters	¡ 0.8 cm
DCA of V0 to primary vertex (PV)	< 0.5 cm
Daughter’s DCA to PV	> 0.8 cm
Decay length	> 6.0 cm
Daughter’s TPC hits	> 15

Table 3.12: V0 reconstruction cuts.

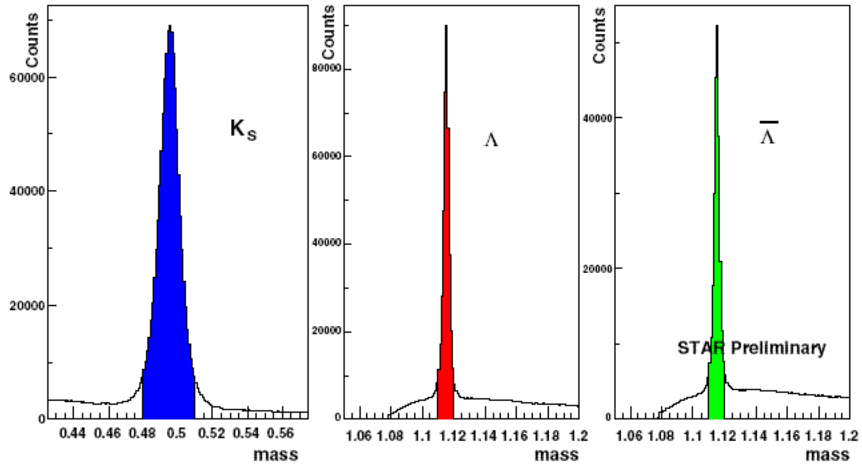

Figure 3.13: Invariant mass distribution for (from left to right) K_s^0, Λ and $\bar{\Lambda}$ for Au+Au collisions at $\sqrt{s_{NN}} = 62$ GeV.

3.2.2 Track Selections

Proton and antiproton are identified by their energy loss inside STAR's main time projection chamber (TPC). The pseudorapidity(eta) coverage of TPC is from -1.3 to 1.3. The tracks cuts are same in Section 3.1.3 and Section 3.1.4.

The $K_s^0 \to \pi^+ + \pi^-$, $\Lambda \to p + \pi^-$ and $\bar{\Lambda} \to \bar{p} + \pi^+$ are reconstructed from their charged daughter tracks inside TPC. We used the same centrality definition and cuts as those used in Ref. [40]. Cuts for V_s^0, a topology for which two tracks with opposite curvatures share a common secondary-vertex, are listed in Table. 3.12. Fig. 3.13 shows the invariant mass distribution of K_s^0, Λ and $\bar{\Lambda}$. The mass window for being a K_s^0 and a Λ and $\bar{\Lambda}$ are [0.48, 0.51] and [1.22, 1.12], respectively.

3.2.3 The Estimation of the Reaction Plane and the Resolution

Because of its small magnitude and the systematic uncertainty caused by non-flow correlations, it is challenging to measure v_1 accurately at RHIC energies. To improve the event plane resolution and minimize non-flow effects, we determine the first-order event plane from the sideward deflection of the spectator neutrons measured by STAR’ s shower maximum detector at zero degree calorimeters (ZDC-SMD), together with tracks

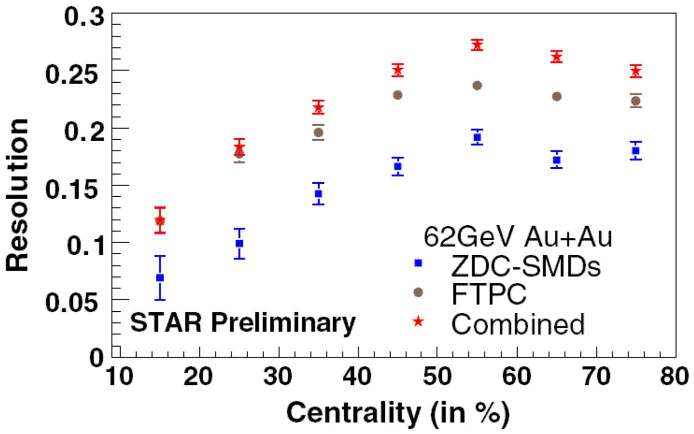

Figure 3.14: The resolution of the first-order full event plane obtained with STAR' s ZD-C-SMD (rectangles), FTPC (solid circles), and the combination of both (stars). Results for Au + Au collisions at 62 GeV is shown.

reconstructed with the forward time projection chambers (FTPC). The event plane obtained from this procedure, which we shall explain more later, is called "combined event plane".

As discussion in Eq.(3.5), the ϕ weight is the inverse of the raw ϕ distribution with proper normalization so that its average equals unity. This weighting allows us to compensate for "blind spots" in the azimuth of FTPC. The η weight is determined by the magnitude of particle' s pseudorapidity. Particles in the forward region have stronger directed flow, thus they are assigned heavier weight than particles at midrapidity. The two weightings, in particular the ϕ weighting, work well if the detecting efficiency is not too far from being uniform in azimuth. However it is not uncommon that during data taking, the detector performance varies dramatically as a function of time, and sometimes it even suffers from severe electronic loss, which results in a big detecting inefficiency that cannot be compensated by weighting. As a consequence of that, the event plane after the weighting procedure might still be not flat. To make a further correction, we use the so-called shifting method to make it flat.

After the shifting, the event plane becomes almost perfectly flat. We apply the same procedure to both FTPC east event plane and FTPC west event plane. The full event

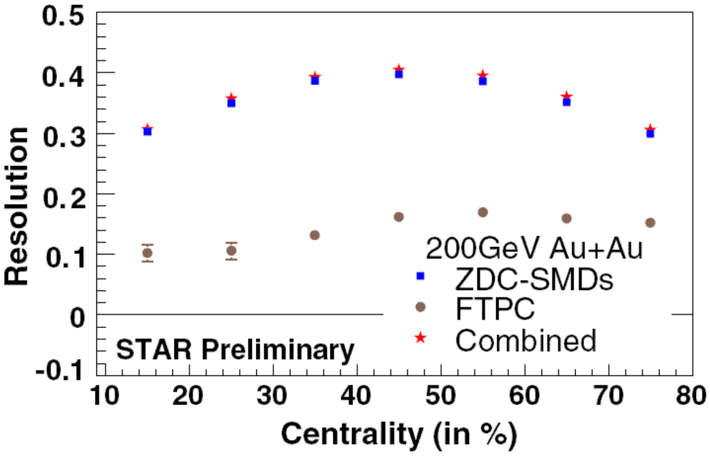

Figure 3.15: The resolution of the first-order full event plane obtained with STAR' s ZD-C-SMD (rectangles), FTPC (solid circles), and the combination of both (stars). Results for Au + Au collisions at 200 GeV is shown.

plane vector is a sum of the two event plane vectors (east and west) with the latter being flipped by 180^O. The flip comes from the fact that directed flow of forward-going particles has an opposite sign than that of backward-going particles. The full event plane is then subsequently flattened by shifting.

Different from FTPC which measures tracks of particles, the ZDC-SMD measures energy deposited by hits. We only applied the shifting method for ZDC-SMD event planes because there is no track-wise information for us to carry out the weighting procedure. Similarly to the case for FTPC, the east and west ZDC-SMD event planes were flattened independently, and then the full event plane was reconstructed from two flattened planes and subsequently flattened.

The final event plane (combined event plane) is obtained by a weighted sum of two unit vectors pointing to the direction of FTPC event plane and ZDC-SMD event plane, respectively. The weight used in the sum is their corresponding event plane resolutions.

The resolution is the first-order event plane resolution. It is a number between 0 and unity depending on both the strength of the flow signal and the number of particles detected. The larger the resolution the easier the flow measurements. In Fig. 3.15 and Fig. 3.14, we compare the resolution of the combined reaction plane to that of ZDC-

SMD event plane and FTPC event plane, for both 200 GeV and 62 GeV.We see that the resolution at 62 GeV is enhanced with the combined reaction plane for most centralities, while no obvious improvement is observed at 200 GeV. This is because of the fact that the directed flow moves to larger pseudo-rapidity at higher beam energy; the FTPC thus becomes less helpful. The v_1 result reported in this paper was obtained with the combined event plane for 62 GeV ($v_1$combined), and ZDC-SMD event plane for 200 GeV (v_1ZDC-SMD), respectively.

3.2.4 The Standard Event Plane Method

In this analysis, the directed flow results are got from the standard event plane method as discussed in Section 3.1.5.

3.3 Directed Flow from Au + Au Collisions at $\sqrt{s_{NN}}$ = 9.2 GeV in Run 8

3.3.1 Data-set and Cuts

In total 3000 events for Au+Au collisions at $\sqrt{s_{NN}} = 9.2$ GeV are used in this study, all taken by a minimum-bias trigger with STAR detector during the RHIC seventh run in year 2008.

Trigger Setup Name	Production	Vertex Cut	Trigger ID	Events No.
ProductionMinBias	P08ic	$\|V_z\| < 75$ cm	minimum bias	3 k

Table 3.13: The trigger and events selection in minimum bias Au+Au collisions at $\sqrt{s_{NN}} =$ 9.2 GeV in Run8.

The main trigger detector used is the vertex position detector (VPD) and the beam-beam counter (BBC) [29]. The trigger and event selection are list in Table 3.13. The BBC is scintillator annuli mounted around the beam pipe beyond the east and west pole-tips of the STAR magnet. It is about 3.75 m away from the center of the nominal

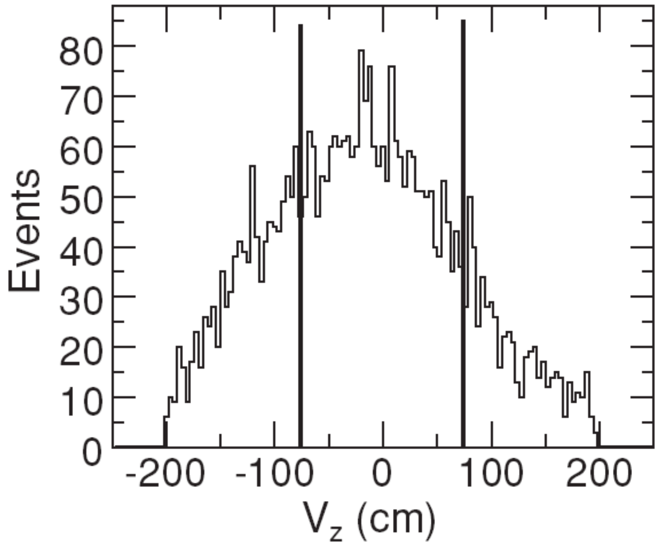

Figure 3.16: The primary vertex V_z in Au + Au collisions at $\sqrt{s_{NN}} = 9.2$ GeV.

interaction region (IR). The inner tiles of the BBCs (the pseudorapidity range is $3.8 < |\eta| < 5.2$) is with the full azimuthal coverage $\phi= 2\ \pi$. The BBCs of the east and west side are used to reconstruct the 1^{st} order event plane for the directed flow analysis. The VPDs are consist of 2 identical detector assemblies which are very close to the beam pipe, one on each side at a distance of —Vz— = 5.6 m from the center of the IR. They are based on the conventional plastic scintillator readout technology by photomultiplier tubes. The main detector used here to obtain the results on directed flow for charged hadrons is the Time Projection Chamber (TPC) and the Forward Time Projection Chambers (FTPCs).

The distribution of the primary vertex position along the longitudinal beam direction (V_z) is shown in Fig. 3.16. The vertical solid lines show the condition of $|V_z| < 75$ cm for selected events.

Fig. 3.17 shows the uncorrected multiplicity distribution for charged tracks from the data (open circles) and from which is obtained from simulation (lines). Simulated multiplicity density is calculated from the Glauber Monte Carlo simulation. More detail can be found in Ref. [41]

The centrality definition *v.s.* the geometric cross section according to the multiplicity for Au+Au collisions are listed in Table. 3.14

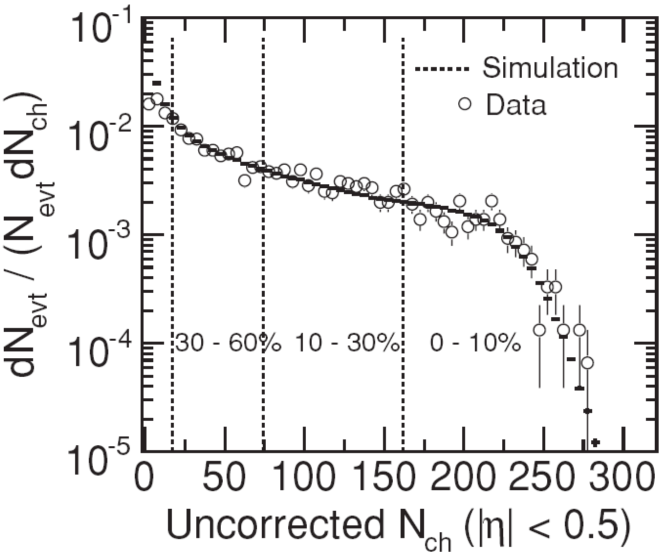

Figure 3.17: The Multiplicity distribution(the circles) from Au + Au collisions at $\sqrt{s_{NN}}$ = 9.2 GeV. The line presents simulated multiplicity distribution.

Centrality Bin	Global Reference Multiplicity	Geometric Cross Section
1	17-73	$30-60\%$
2	74-161	$10-30\%$
9	≥162	$0-10\%$

Table 3.14: Centrality definition in Au+Au collisions at $\sqrt{s_{NN}} = 9.2$ GeV fron Run 8 data sample.

3.3.2 The Mixed Harmonics Method

Because the slope of directed flow at RHIC is extremely small, the first-harmonic event plane is poorly defined in the TPC. A better way to measure v_1 is to use those mixed harmonics involving the second-harmonic event plane. This method utilizes the large elliptic flow signal at RHIC, and at the same time suppresses the non-flow arises from correlating particles from the same harmonics. We determine two first-order reaction planes ψ_1^{FTPC1} and ψ_1^{FTPC2} in the FTPCs and the second-order reaction plane ψ_2^{TPC1} in the TPC. We denote this measurement as $v_1\{EP_1, EP_2\}$ [40].

$$v_1\{EP_1, EP_2\} = \frac{\langle \cos(\phi + \psi_1^{FTPC} - 2\psi_2^{TPC})\rangle}{\sqrt{\langle \cos(\psi_1^{FTPC1} + \psi_1^{FTPC2} - 2\psi_2^{TPC})\rangle \bullet Res(\psi_2^{TPC})}} \tag{3.25}$$

where the ϕ of the particle is correlated with the ψ_1^{FTPC} in the other subevent and

$$Res(\psi_2^{TPC}) = \langle \cos[2(\psi_2 - \psi_{RP})]\rangle \tag{3.26}$$

represents the resolution of the second-order event plane measured in the TPC. The way of the estimation of the reaction plane and the resolution can be found in Section 3.1.2. This resolution, as usual, is derived from the square root of the correlation of TPC subevent planes.

CHAPTER 4

Results

In this chapter, the charged hadrons and the identified particles (pions, kaons(K^0_S), protons and anti-protons) directed flow from in Au+Au collisions at $\sqrt{s_{NN}} = 200$ GeV are presented. The systematic uncertainty about the results are discussed.

4.1 Charged Hadrons Directed Flow in Run4 and Run7

The Fig. 4.1 shows the charged hadrons v_1 as function of η from the peripheral(left top panel) to the central(right bottom panel) in Au+Au collisions at 200GeV. The p_T range in this study is 0.15-2.0 GeV/c. The v_1 results in Run7 data-set(blue open crosses) are compared with the Run4(black open stars) centrality by centrality. Although the resolution in Run4 and Run7 exist some differences in certain centralities, the charged hadron's v_1 are consistent with each other within error bars.

In order to demonstrate the difference of charged hadrons v_1 between the Run7 and Run4 data-set (named v_1(Run7) and v_1(Run4)), the $v_1(\text{Run7}) - v_1(\text{Run4})$ as function of η is shown in Fig. 4.2. It is fitted by the linear function. The relative differences $(\frac{v_1(\text{Run7})-v_1(\text{Run4})}{v_1(\text{Run4})})$ is no more than 10%. Zooming in the mid-rapidity, the $v_1(\text{Run7}) - v_1(\text{Run4})$ as function of η is shown in Fig. 4.3. Fitting by the linear function, it is clear that the charged hadrons v_1 difference between Run4 and Run7 is quite small. The $v_1(\text{Run7}) - v_1(\text{Run4})$ in $|\eta| < 1.3$ is less than 0.2%. The difference, which appears to be mostly caused by a slightly difference in our method for determining centrality, is considered as one source of the systematic error for the identified particles directed flow.

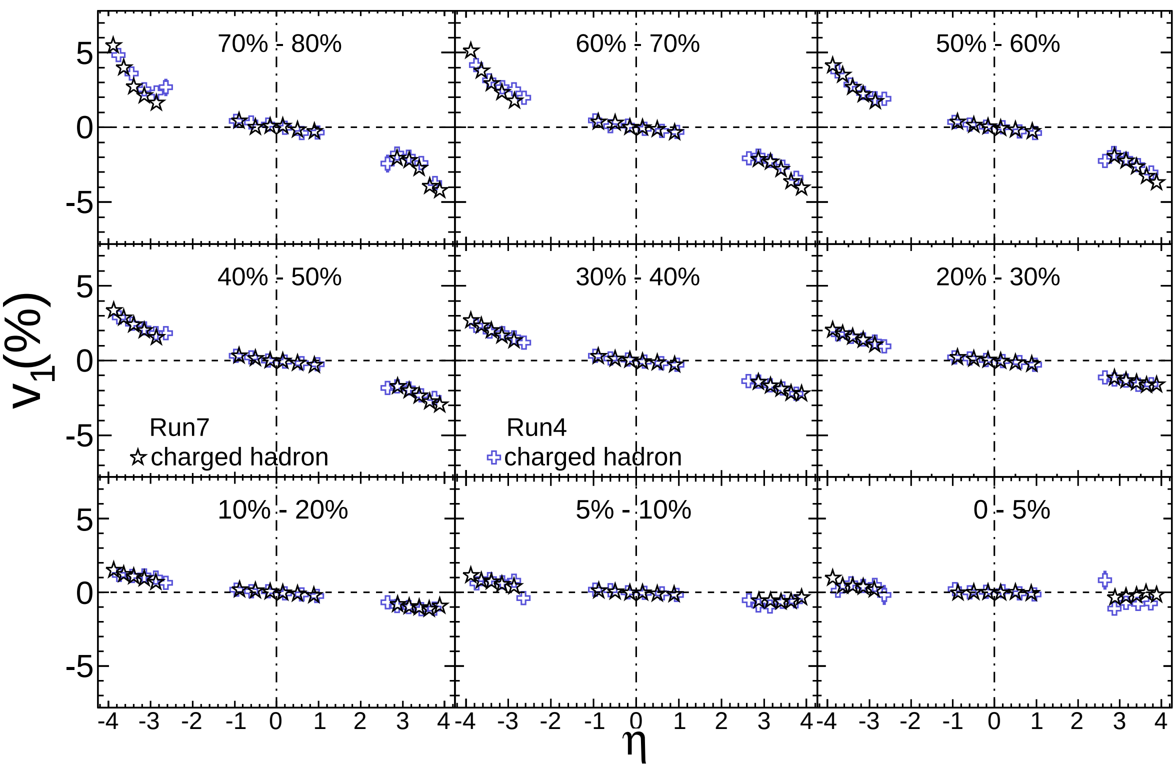

Figure 4.1: Charged hadron v_1 *v.s.* η for Au + Au collisions at $\sqrt{s_{NN}}$ = 200 GeV from Run4(black stars) and Run7(blue crosses) in 9 centralities.

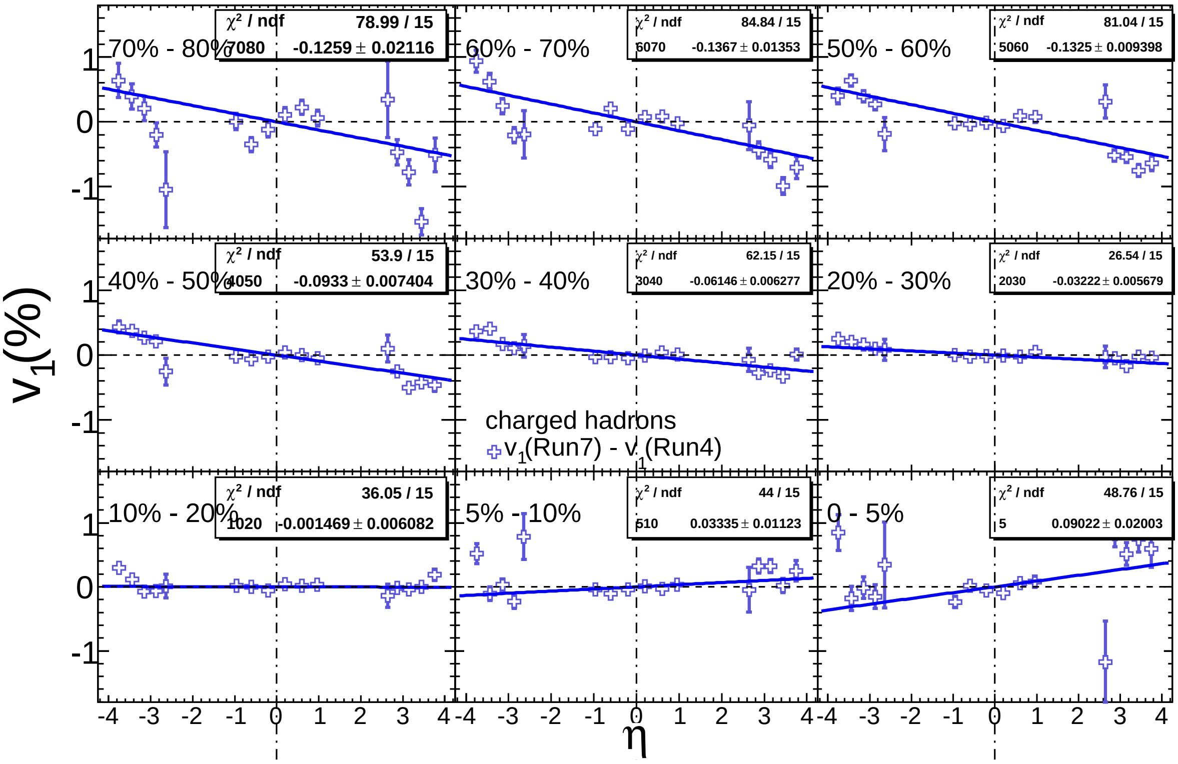

Figure 4.2: The difference between the charged hadron v_1 $v.s.$ η in $|\eta| < 4.0$ for Au + Au collisions at $\sqrt{s_{NN}} = 200$ GeV from Run4 and Run7(blue crosses) in 9 centralities.

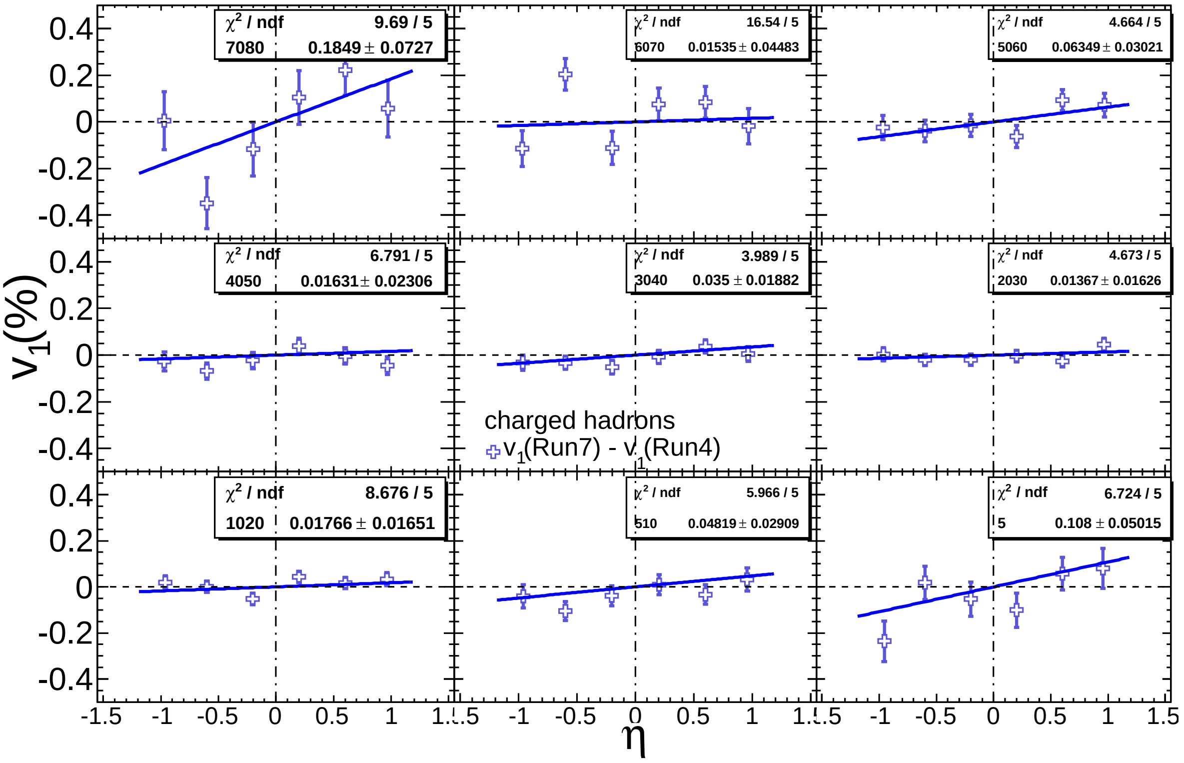

Figure 4.3: The difference between the charged hadron v_1 *v.s.* η in $|\eta| < 1.3$ for Au + Au collisions at $\sqrt{s_{NN}} = 200$ GeV from Run4 and Run7(blue crosses) in 9 centralities.

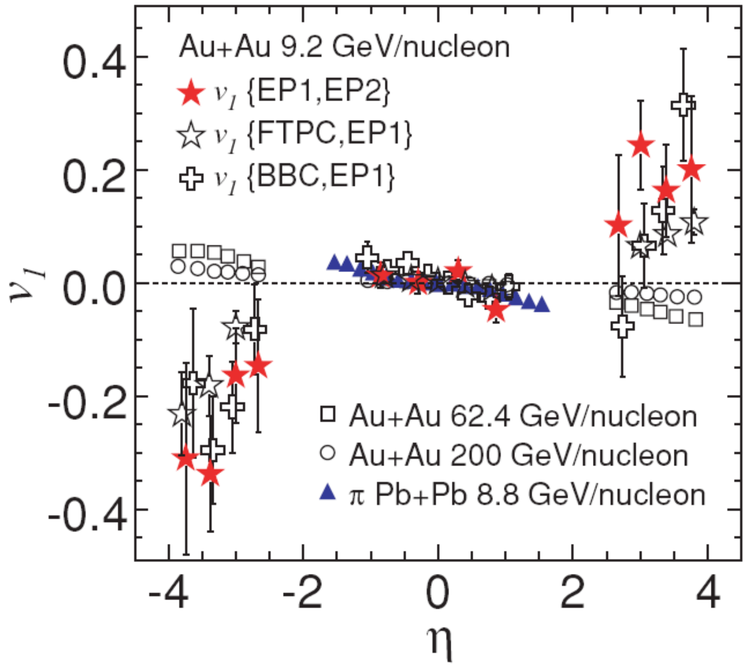

Figure 4.4: Charged-hadron v_1 as function of η from the centrality 0 - 60% in Au + Au collisions at $\sqrt{s_{NN}}$ = 9.2 GeV. The errors here are statistical. The solid star symbols are the results obtained from the mixed harmonic method, while the open star and open plus symbols represent results from the standard methods). The results are compared to v_1 from centrality 30 - 60% collision Au+Au collisions at $\sqrt{s_{NN}}$ = 62.4 and 200 GeV [48]. For comparison, charged pions' directed flow for the 0 - 60% centrality from Pb + Pb collisions at $\sqrt{s_{NN}}$ = 8.8 GeV [49] are also shown.

More detail is discussed in next section.

4.2 Charged Hadrons Directed Flow in Run 8

Fig. 4.4 shows the charged hadrons $v_1(\eta)$ in 0-60% most central Au+Au collisions at $\sqrt{s_{NN}}$ = 9.2 GeV. The p_T range is 0.15 - 2.0 GeV/c for this study. The v_1 results from $\sqrt{s_{NN}}$ = 9.2 GeV are obtained by different methods:

1. The standard methods: the one for which the 1^{st} order event plane is reconstructed from the FTPC tracks is named $v_1\{EP1, FTPC\}$, while which uses BBC hits for the 1^{st} order event plane reconstruction is named as$v_1\{EP1, BBC\}$

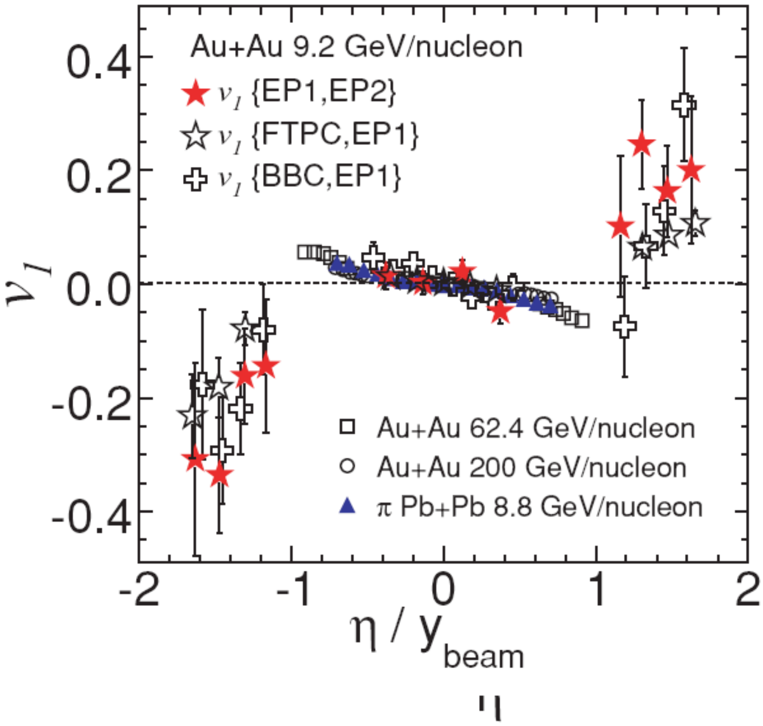

Figure 4.5: Proton and antiproton v_1 versus y, for Au+Au collision at 200 GeV using the reaction plane reconstructed by STAR’ s ZDC-SMD in Run4.

2. The mixed harmonics method: denoted by $v_1\{EP1, EP2\}$. In this method, it utilizes the large elliptic flow (v_2) signal at RHIC, and in the meanwhile it suppresses the non-flow effect which arise from the correlation of particles from the same harmonics.

The directed flow results at $\sqrt{s_{NN}} = 9.2$ GeV from different methods are consistent within the errors. These results from $\sqrt{s_{NN}} = 9.2$ GeV in Au+Au collisions have been compared with the corresponding results in centrality 30%-60% Au + Au collisions at 62.4 and 200 GeV from Ref. [48]. The results are also compared with charged pions’ v_1 in Pb + Pb collisions at $\sqrt{s_{NN}} = 8.8$ GeV. The directed flow values have beam energy independence at and near mid-rapidity, while at forward rapidity, the its seem to change sign at lower colliding energy. However, if directed flow value are plotted as a function of η scaled with the beam rapidity (y_{beam}), as shown in the Fig. 4.5. In the common region of values of η/y_{beam}, the v_1 values remain the same at all energies.

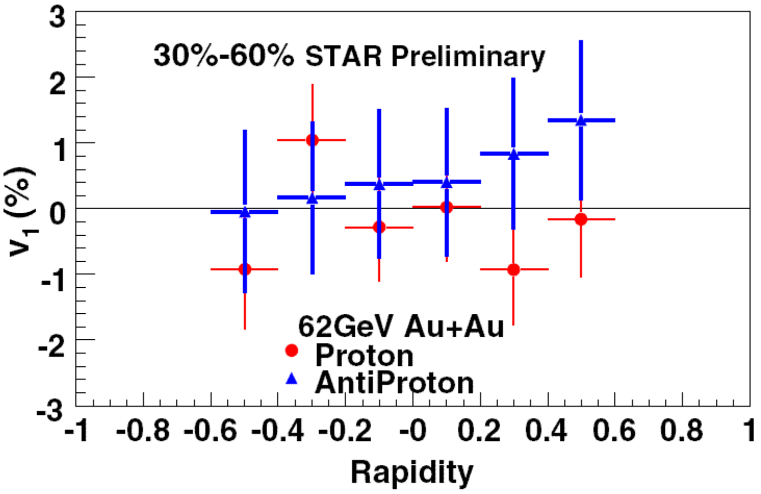

Figure 4.6: proton and antiproton v_1 versus y, for Au+Au collision at 62 GeV using combined reaction plane in Run4.

4.3 Identified Particles' Directed Flow

4.3.1 Rapidity and Centrality Dependance of Directed Flow in Run4

Fig. 4.7 and Fig. 4.6 show v_1 of proton and antiproton as a function of rapidity, for 30 – 60% central Au+Au collisions at 62 GeV and 200 GeV in Run 4. The p_T cut is 0.4 ¡ p_T ¡ 1.0 (GeV/c) and 0.15 ¡ p_T ¡ 1.0 (GeV/c), for protons and antiprotons respectively. The low-end cut for protons is set larger than that of antiprotons in order to remove the contamination of protons produced by beam backgrounds. We fit our result with a linear function passing through the origin, because one expects that v_1 is zero at $\eta = 0$. The slope obtained from the fitting is -0.4 ± 1.1 for proton and 1.3 ± 1.5 for antiproton at 62 GeV, and -1.9 ± 0.8 for proton and -0.6 ± 1.0 for antiproton at 200 GeV. Overall we report that within the rapidity range we studied, proton v_1 is less than 1%, and antiproton is less than 2% at both energies. The big statistical error prevents us from observing a wiggle structure, if there is any. However, during Run 7, we have taped 60 M events, which will allow us to see the rapidity dependence in more detail.

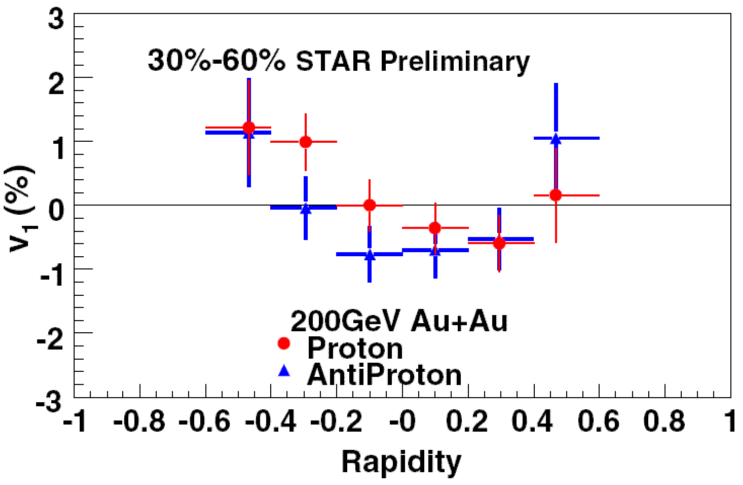

Figure 4.7: Proton and antiproton v_1 versus y, for Au+Au collision at 200 GeV using the reaction plane reconstructed by STAR' s ZDC-SMD in Run4.

We also made an attempt to study the directed flow of K^0_S, Λ and $\bar{\Lambda}$ using the combined reaction plane for Au+Au collision at 62 GeV in Run 4. The result is shown in Fig. 4.8. Their magnitude is found not more than 5% within the rapidity range we studied. The slope for the K^0_S v_1 is -3.2 ± 1.7 if fitted with a linear function. Our current measurements are dominated by statistic errors. Detailed study of systematic errors will be performed with large statistics obtained from Run 7.

In Fig. 4.9 and Fig. 4.10 show v_1 of proton and antiproton as a function of centrality in Au+Au collisions at 62 GeV and 200 GeV in Run 4. No strong centrality dependence is observed due to the small signal and large error bars.

4.3.2 Rapidity Dependance of Directed Flow in Run7

In Fig. 4.11, $v_1(y)$ of $\pi^{\pm}$, $K^{\pm}$, K^0_S, p and $\bar{p}$ are presented for centrality 10-70%. Following convention, the sign of spectator v_1 in the forward region is chosen to be positive, to which the measured sign of v_1 for particles of interest is only relative. Fitting with a linear function, the slopes are $-0.15 \pm 0.05(\text{stat}) \pm 0.08(\text{sys})(\%)$ for the protons, $-0.46 \pm 0.06(\text{stat}) \pm 0.04(\text{sys})(\%)$ for the antiprotons, $-0.27 \pm 0.01(\text{stat}) \pm 0.01(\text{sys})(\%)$ for the pions, $-0.02 \pm 0.11(\text{stat}) \pm 0.04(\text{sys})(\%)$ for the kaons and $-0.17 \pm 0.02(\text{stat}) \pm 0.04(\text{sys})(\%)$

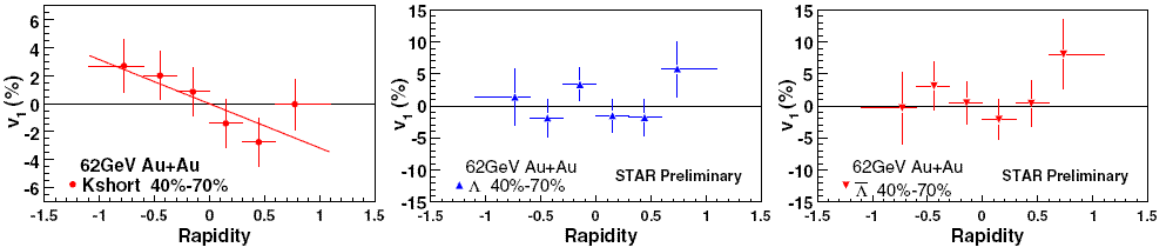

Figure 4.8: Directed flow of K_S^0(left), Λ(middle) and $\bar{\Lambda}$(right) as a function of rapidity, for centrality 40 - 70% in 62 GeV Au+Au collision using combined reaction plane in Run4 : K_S^0(left panel), Λ(middle panel) and $\bar{\Lambda}$(right panel).

Particle Species	dv_1/dy	χ^2/ndf
Proton	-0.15 ± 0.05	4.76/5
Antiproton	-0.46 ± 0.06	7.40/5
Pion	-0.27 ± 0.01	14.20/5
Kaon	-0.02 ± 0.11	3.81/5
Kshort	-0.17 ± 0.02	24.7197/5

Table 4.1: dv_1/dy slopes from proton, antiproton, pion, kaon and K_S^0 in Au+Au collisions at $\sqrt{s_{NN}}$ = 200 GeV.

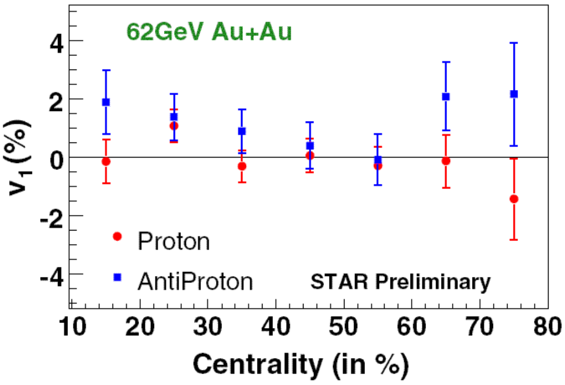

Figure 4.9: Proton and antiproton v_1 versus centrality, for Au+Au collision at 62 GeV using combined reaction plane in Run4.

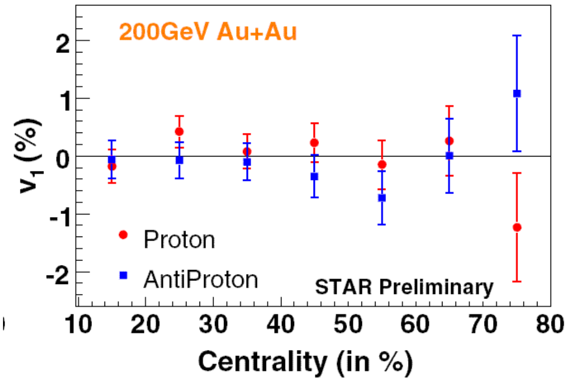

Figure 4.10: Proton and antiproton v_1 versus centrality, for Au+Au collision at 200 GeV using the reaction plane reconstructed by STAR ZDC-SMD in Run4.

for the K^0_S. The relative 16% common systematic error for all particles is not listed here. The $v_1(y)$ slope for the three produced particle types ($\pi^{\pm}$, $K^{\pm}$, K^0_S and $\bar{p}$) are mostly found to be negative at mid-rapidity, which is consistent with the anti-flow picture. In particular, K^0_S is less sensitive to shadowing effects due to the small kaon-nucleon cross section, yet it shows a negative slope. This is again consistent with the anti-flow picture. Interestingly, $v_1(y)$ for protons exhibits a clearly flatter shape than that for antiprotons. While mass may contribute to the difference in slope between pions and protons/antiprotons, it cannot explain the difference in slope observed for antiprotons and protons. Indeed, the observed v_1 for protons is a convolution of directed flow of produced protons with that of transported protons (from the original projectile and target nuclei), so the flatness of inclusive proton $v_1(y)$ around midrapidity could be explained by the negative flow of produced protons being compensated by the positive flow of protons transported from spectator rapidity, as a feature expected in the anti-flow picture.

In Fig. 4.12, pion and proton $v_1(y)$ is plotted together with five model calculations, namely, RQMD [37], UrQMD [39], AMPT [42], QGSM with parton recombination [43] and ideal slopes from a hydrodynamic calculation with a tilted source [26]. The model calculations are performed in the same p_T acceptance and centrality as the data. The RQMD and AMPT model calculation predict the wrong sign of pion $v_1(y)$, and the

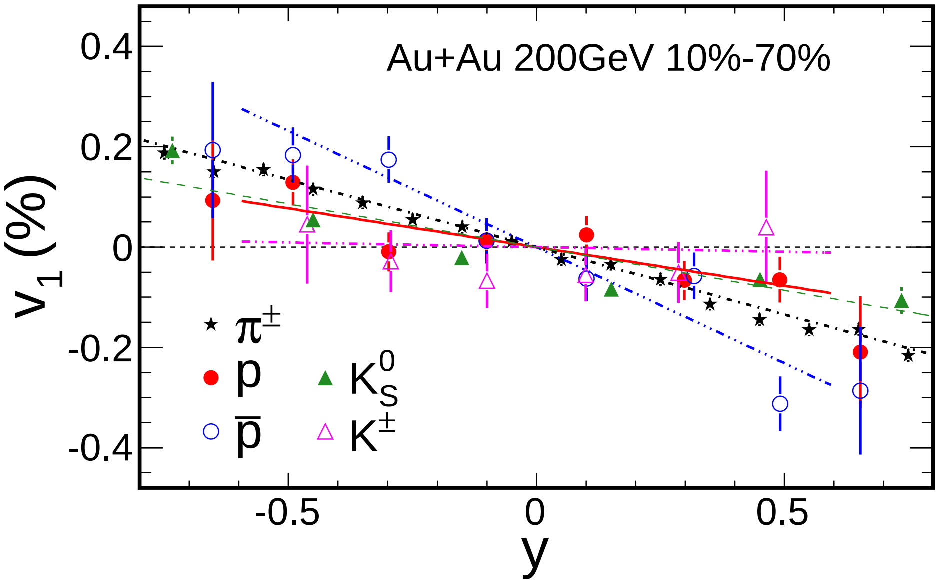

Figure 4.11: v_1 for $\pi^{\pm}$, $K^{\pm}$, K_S^0, p and $\bar{p}$ as a function of rapidity for 10-70% Au + Au collisions at $\sqrt{s_{NN}}$ = 200 GeV. The lines present the linear fit to the $\pi^{\pm}$, $K^{\pm}$, K_S^0, p and $\bar{p}$'s $v_1(y)$ respectively. Data points around $y = 0.29$ are slightly shifted horizontally to avoid overlapping.

RQMD and the UrQMD predict the wrong magnitude of proton $v_1(y)$. None of models explored can describe $v_1(y)$ for pions and protons simultaneously.

The model version numbers and parameter settings are listed as following:

- RQMD: the relativistic quantum molecular dynamics (RQMD v2.4) model in cascade mode [37]. The impact parameter range is $b = 4.6 - 12.4$ fm in Au + Au collisions at $\sqrt{s_{NN}} = 200$ GeV.
- QGSM: the quark-gluon string transport model has been extended for partonic recombination and fusion processes [43]. The centrality is 10% - 70% in Au+Au collisions at $\sqrt{s_{NN}} = 200$ GeV.
- AMPT: a multiphase transport (AMPT) model with string melting [42]. The quark coalescence is used instead to combine partons into hadrons and the parton cross section is chosen as 3 mb. The centrality definition is 10% - 70% with the corresponding impact parameter range $b = 4.7 - 12.7$ fm in Au + Au collisions at $\sqrt{s_{NN}} = 200$ AGeV

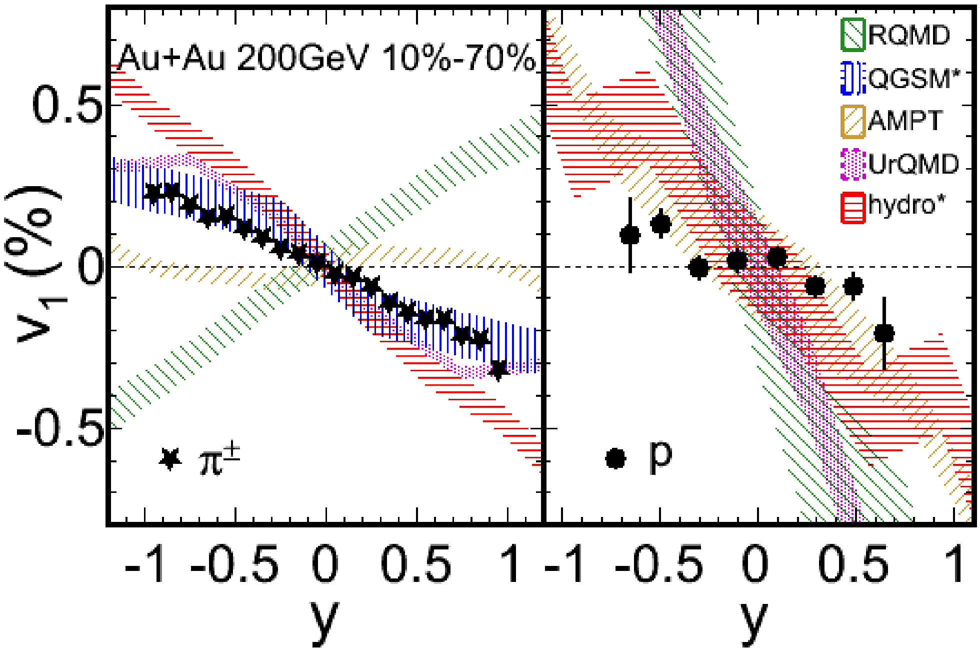

Figure 4.12: Model calculations of pion (left panel) and proton (right panel) $v_1(y)$ for 10-70% Au + Au collisions at $\sqrt{s_{NN}}$ = 200 GeV. QGSM* model presents the basic Quark-Gluon String model with parton recombination [43]. Hydro* model presents the hydrodynamic expansion from a tilted source[26].

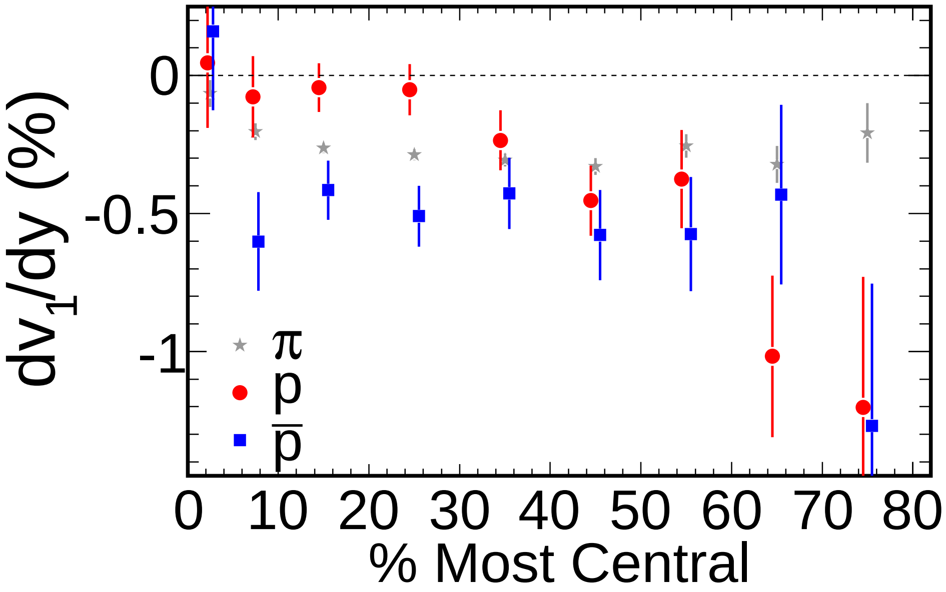

Figure 4.13: Charged (solid stars), proton (solid circles) and anti-proton (solid squares) $v_1(y)$ slope (dv_1/dy) at midrapidity as a function of centrality for Au + Au collisions at $\sqrt{s_{NN}}$ = 200 GeV.

- UrQMD: the Ultra-relativistic Quantum Molecular Dynamics (UrQMD 2.3) model in cascade mode [39]. The centrality is 10% - 70% in Au + Au collisions at $\sqrt{s_{NN}}$ = 200 AGeV at, i.e., with the corresponding impact parameter range $b = 4.4 - 11.7$ fm.

- hydro: a hydrodynamics model with a tilted source [26]. The centrality is 10% - 70% in Au + Au collisions at $\sqrt{s_{NN}}$ = 200 AGeV.

4.3.3 Centrality Dependance of Directed Flow in Run7

However, anti-flow has difficulties in explaining the centrality dependence of v_1. Fig 4.14 shows $v_1(y)$ slope at midrapidity as a function of centrality for protons, anti-protons and charged pions. If there is an anti-flow due to the strong, tilted expansion, one expects such an effect is larger in mid-central collisions than that in peripheral collisions. As a consequence, proton v_1 slope, which is expected to be positive in very peripheral collisions, will change its sign to negative in mid-central collisions and approach zero in central collisions. However, in 30-80% central collisions, proton v_1 slope is found negative and the magnitude decreases with decreasing centrality. In more central (5-30%) collisions, proton v_1 slope becomes extremely small, while anti-proton v_1 slope remains negative with finite magnitude, and continues to follow that of charged particles (mostly pions). Anti-flow may cause a difference between v_1 of protons and anti-protons, and such difference is expected to be accompanied by strongly negative v_1. In data, the large difference between proton and anti-proton v_1 slopes are seen in 5-30% centrality, while strongly negative v_1 slopes are found for protons, anti-protons and charged pions in a different centrality (30-80%). The hydrodynamics model with tilted source, while correctly predicts the pion $v_1(y)$ slope, does not predict the difference in $v_1(y)$ between particle species [44].

Assume that produced proton has the same yield and v_1 slope of it is as same as that of antiprotons. With the known

- inclusive proton (=transported + produced) v_1 slope
- antiproton v_1 slope
- $\bar{p}/p$ ratio(=produced proton/inclusive proton) in table IX. in Ref. [46]

We should be able to infer the v_1 slope for transported protons. As we expected, the transported proton v_1 slope are mostly positive. It is hard to refer the sharp of it within the huge error bars. Yet, it gives our a picture that the transported proton cancels out the produced proton v_1 effect.

4.3.4 Energy Dependance of Directed Flow in Run7

In Fig. 4.15, proton $v_1(y')$ slope - F ($= dv_1/dy'$) at midrapidity is plotted as a function of collision energy, where $y' = y/y_{beam}$. The values for the $v_1(y')$ slope is extracted via a polynomial fit of the form $Fy' + Cy'^3$. At low energies, the slope of proton's $\langle p_x(y') \rangle$ distribution has been studied by the E877 [18] and the E895 [17] Collaboration. The $d\langle p_x \rangle/dy'$ decrease steadily with increasing beam energy over these energy range. The similar trend is shown in the Fig. 4.15, the proton v_1 slope decreases rapidly with

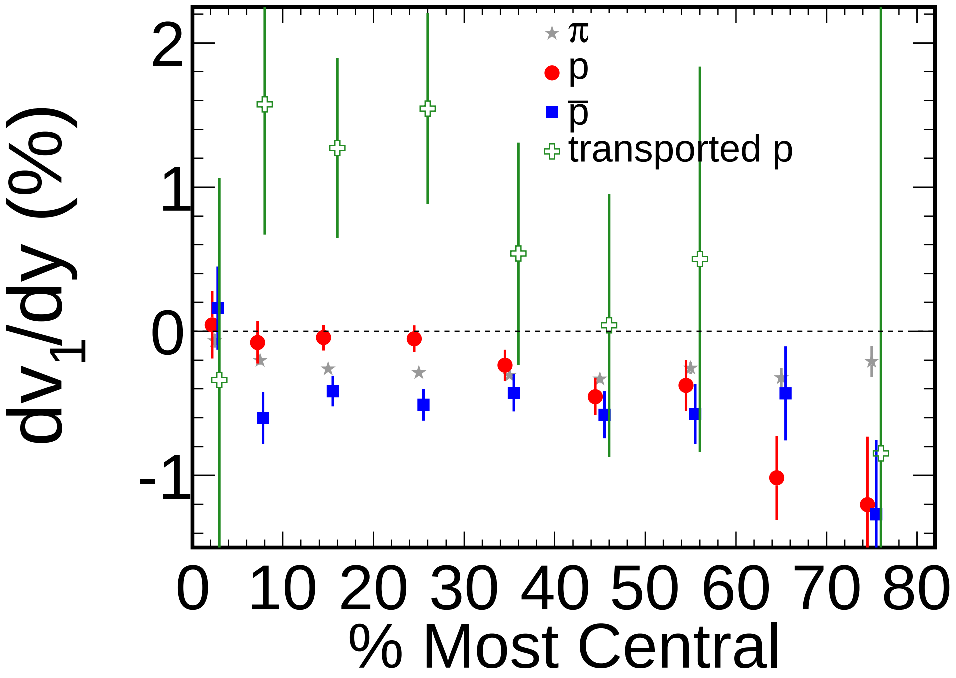

Figure 4.14: Pion(grey stars), proton(red circles), antiproton(blue squares) and transported proton(dark green crosses) $v_1(y)$ slope (dv_1/dy) at midrapidity as a function of centrality for Au + Au collisions at $\sqrt{s_{NN}} = 200$ GeV.

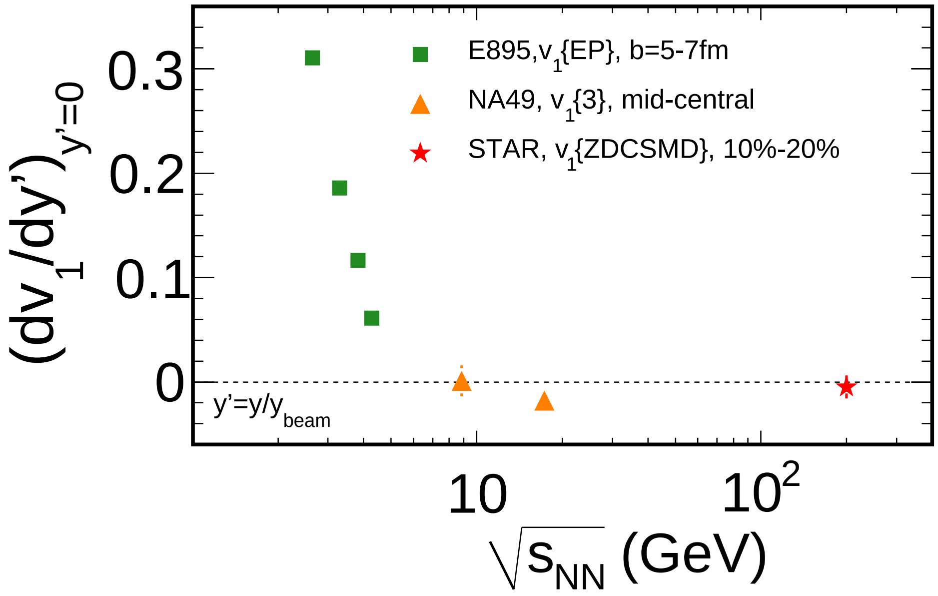

Figure 4.15: Proton $v_1(y^{'})$ slope $(dv_1/dy^{'})$ at midrapidity as a function of center of mass collision energy, where $y^{'} = y/y_{beam}$.

increasing energy, reaching zero around $\sqrt{s_{NN}} = 9$ GeV. It changes its sign to negative as shown by the data point at $\sqrt{s_{NN}} = 17$ GeV, measured by the NA49 experiment. The E877 result is not included in this plot because no dv_1/dy' from the E877 experiment is available. With previous measurements, which include only one point above $\sqrt{s_{NN}} = 9$ GeV, one cannot conclude if proton v_1 slope continues to decrease or stays close to zero when energy increases, the addition of the data point from RHIC indicates that proton v_1 slope remains close to zero at $\sqrt{s_{NN}} = 200$ GeV. Judging over the broad energy range, the transition of the proton v_1 slope sign from positive to negative happens around $\sqrt{s_{NN}} = 9$ GeV, interestingly, it coincides with the energy vicinity where $\langle k^+\rangle/\langle\pi^+\rangle$ exhibits a horn [45].

4.4 Systematic Uncertainties

Table. 4.2 listed the particles'dv_1/dy slopes value, statistic and systematic error. There are four systematic error sources, it is listed in Table. 4.3 and explained in the following:

The major systematic error in determining the slope of $v_1(y)$ is from the particle misidentification, and it is evaluated by varying the dE/dx cut and DCA cuts for the identified particle selections (named “PID” in the table. 4.3).

For protons, the contamination of background protons from beam on beam pipe collisions also contributes to the systematics considerably. Since the fraction of background protons can be estimated by comparing the $\bar{p}/p$ ratio derived from tracks that went into in this analysis to that of the published result [46], this effect can be estimated by taking the maximum change of $v_1(y)$ slope when taking into account the background contamination, with the assumption that background protons can have either zero v_1 or the same v_1 of pions (called “background” in Table.4.3).

Due to the p_T uniformity vs. y for protons and antiprotons, the limit p_T acceptance effect is considered as one source of systematic errors. It is estimated by taking the difference between slopes fitted with points integrated with the p_T acceptance at $y = 0$ and at $y = \pm 0.6$ (labeled as “p_T acceptance” in Table. 4.3).

The above uncertainties were estimated for each individual particle species respectively and added in quadrature to obtain the total systematic uncertainty from PID, the p_T acceptance effect and background contribution together.

As a systematic check we have compared our charged $v_1(\eta)$ slope to that from the RHIC run in 2004. The difference, which appears to be mostly caused by a slightly difference in our method for determining centrality. This uncertainty has been included in the systematic error assuming it is equal for all particle types. It was estimated to be $\sim 4\%$(relative error). The first order event plane determination, which was estimated to be $\sim 15\%$ relatively [47]. This common relative systematic error should be also applied to all particles. The relative 16% common systematic error for all particles is not listed in the following discussion.

Other systematic errors have been evaluated to be negligible.

Other systematics have been evaluated to be negligible.

Particle Species	dv_1/dy	Statistical Error	Systematic error
Proton	-0.15	0.05	0.08
Antiproton	-0.46	0.06	0.04
Pion	-0.27	0.01	0.01
Kaon	-0.02	0.11	0.04
Kshort	-0.17	0.02	0.04

Table 4.2: dv_1/dy slopes' statistic and systematic error from proton, antiproton, pion, kaon and K^0_S in Au+Au collisions at $\sqrt{s_{NN}} = 200$ GeV.

4.4.1 Systematic error from the particle misidentification

The systematic errors of $v_1(y)$ slope is evaluated by varying the dE/dx cuts and DCA cuts for the identified particles selections. The maximum difference between the cuts are taken as the systematic uncertainty. Fig. 4.16 shows the pion, proton, antiproton and kaon's directed flow as function of rapidity in different cuts:

1. DCA < 1 cm, $|n\sigma| < 2.5$;

Particle Species	PID	p_T acceptance	background
Proton	0.07	0.01	0.01
Antiproton	0.04	0.001	
Pion	0.01		
Kaon	0.04		
Kshort	0.04		

Table 4.3: dv_1/dy slopes' four type systematic error from proton, antiproton, pion, kaon and K^0_S in Au+Au collisions at $\sqrt{s_{NN}}$ = 200 GeV.

2. DCA < 2 cm, $|n\sigma| < 2.5$;
3. DCA < 1 cm, $|n\sigma| < 2$;
4. DCA < 1 cm, $|n\sigma| < 1$;

The linear function $v_1 = Fy$ are used to fit the data points and the differences between the slope F = dv_1/dy are taken as systematic errors(shadow bands) for each particle species. The systematic errors are listed in Table. 4.3 Queue 1.

4.4.2 Systematic error from the p_T acceptance effect

The p_T acceptance effect from AMPT calculation shown in Fig. 4.17. The results show $p_T < 1.0$ GeV/c have significant difference slope compared to that from full p_T acceptance. It is crucial to take take p_T acceptance effect at $y \sim 0.6$ region for protons and antiprotons' directed flow analysis.

This effect is estimated in this way:

- calculate the integral v_1 from v_1 vs. p_T at $y \sim 0$ with the relative p_T yield at $y \sim 0$., shown by the open squares in Fig. 4.18 and Fig. 4.19;
- take the integral v_1 from v_1 vs. p_T at $y \sim 0$ with the relative p_T yield at $y \sim \pm0.6$, shown by the full circles in Fig. 4.18 and Fig. 4.19;;

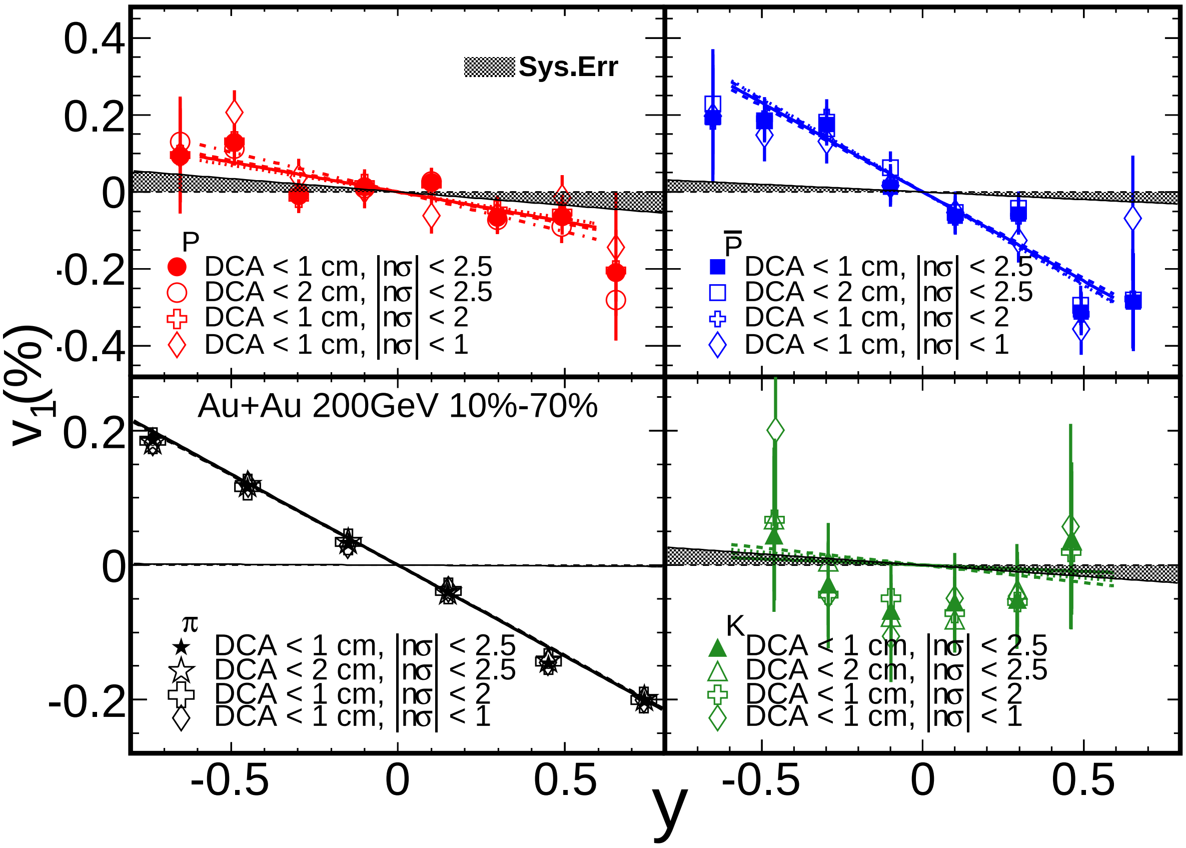

Figure 4.16: The $v_1 vs.y$ for pion, proton, antiproton and kaon in different cut types. The systematic errors are shown in shadow bands.

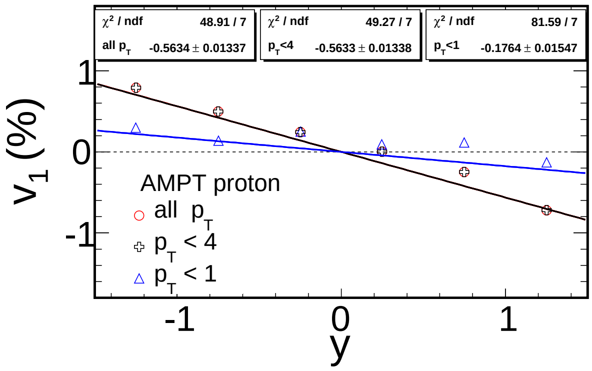

Figure 4.17: The proton directed flow as function of rapidity in centrality 10%-70% from AMPT model in Au+Au collision at 200GeV under different p_T cut: the whole p_T range(circles); $p_T < 4.0$ GeV/c(crosses); $p_T < 1.0$ GeV/c(triangles). The lines present the linear fit.

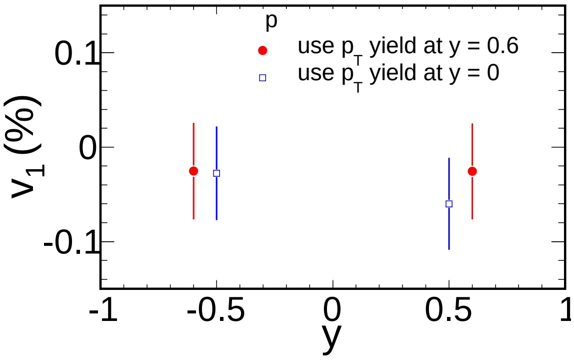

Figure 4.18: The two integral v_1 value at $y = \pm 0.6$ from proton.

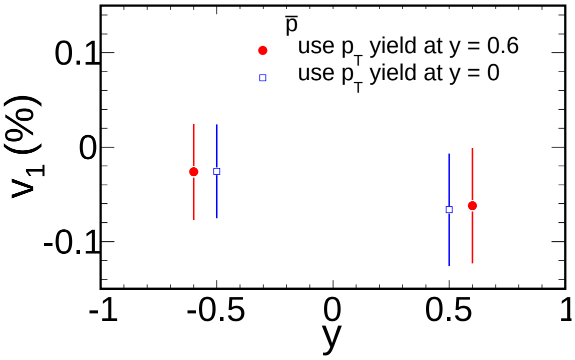

Figure 4.19: The two integral v_1 value at $y = \pm 0.6$ from antiproton.

- take the difference of the two integral v_1 above into account of the v_1 value at $y = \pm 0.6$, shown in Fig. 4.18 for protons and Fig. 4.19 for antiproton;
- the change of the dv_1/dy slope is taken as the systematic error from the p_T acceptance effect, shown in Fig. 4.20 for proton and Fig. 4.21 for antiproton. The dv_1/dy slope are listed in Table. 4.4 for protons and Table. 4.5 for antiprotons.

types	dv_1/dy	χ^2/ndf
original	-0.167 ± 0.049	5.649/7
min	-0.163 ± 0.049	5.772/7
max	-0.171 ± 0.049	5.683/7

Table 4.4: Proton dv_1/dy slopes from from varying the v_1 at $y \sim \pm 0.6$ in Au+Au collisions at $\sqrt{s_{NN}} = 200$ GeV.

types	dv_1/dy	χ^2/ndf
original	-0.448 ± 0.057	7.987/7
min	-0.448 ± 0.057	8.002/7
max	-0.449 ± 0.057	7.974/7

Table 4.5: Antiproton dv_1/dy slopes from from varying the v_1 at $y \sim \pm 0.6$ in Au+Au collisions at $\sqrt{s_{NN}} = 200$ GeV.

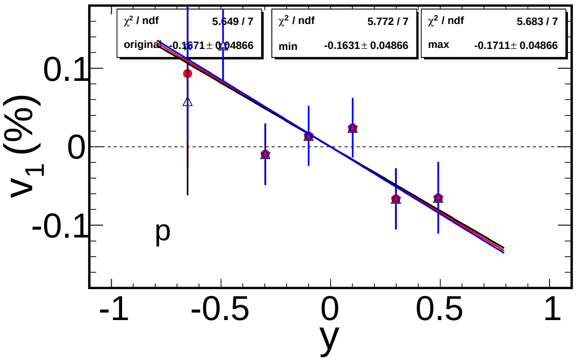

Figure 4.20: By varying the v_1 value at ($y \sim \pm 0.6$) according to the v_1 estimation of the p_T acceptance effect, the dv_1/dy proton slopes are the linear fits.

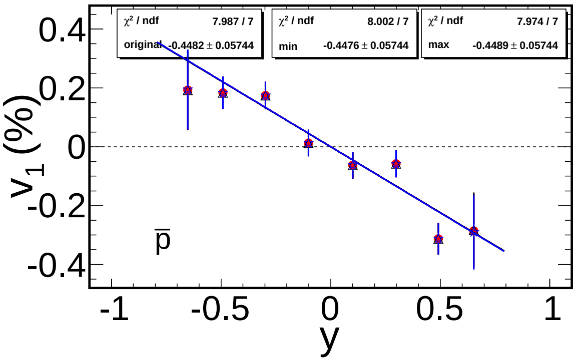

Figure 4.21: By varying the v_1 value at ($y \sim \pm 0.6$) according to the v_1 estimation of the p_T acceptance effect, the dv_1/dy antiproton slopes are the linear fits.

4.4.3 Systematic error from different centrality of Run4/7

One more systematic error arise from a slightly difference in our method for determining centrality. As a systematic check, the charged hadron's $v_1(\eta)$ slope are compared from the RHIC run in 2004 and 2007, shown in Fig.4.22. The relative error is found to be up to 3.8%. This uncertainty has been included in the systematic error assuming it is equal for all particle types, shown in Queue 2 of Table. 4.3.

4.4.4 Systematic error from the background contamination

The background contamination effect on proton is also considered. Assume that

- the inclusive proton v_1 contains the real proton and background proton' v_1 with relative yields, written as: v_1(inclusive proton) = v_1(real proton) × relative yield of real proton + v_1(background) × relative yield of background
- the background protons are knocked out by bulk of pions, thus their v_1 range is in between 0 and -0.128%(shown in Fig. 4.23).
- the relative yield of background in $0.4 < p_T < 1.0$ from centrality 10%-70% is 0.054 by regarding $\bar{p}/p$ ratio in $p_T > 1.0$ as the standard.

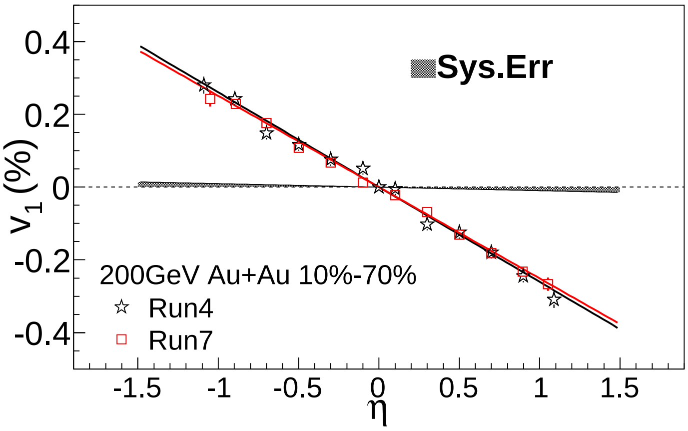

Figure 4.22: The charged hadron v_1 as function of rapidity from Run4(black stars) and Run7(red squares) at $\sqrt{s_{NN}}$ = 200 AGeV in centrality 10%-70%. The black and red lines present the corresponding linear fits for Run4 and Run7 respectively.

Thus

- the background protons are flowing with 0% of pion v_1, the v_1 for primordial proton is (-0.0015 - 0 × 0.054)0.946 = -0.159%,
- the background protons are flowing with -0.128% of pion v_1, the v_1 for primordial proton is (-0.0015 - (-0.128% × 0.054))0.946 = -0.151%,

So the systematic error due to the background contamination is no more than 0.01% relatively with the estimation of the worst case.

4.4.5 Systematic error for K_s^0

For the K_s^0, the difference between v_1 slope(listed in Table. 4.6) of the standard method and v_1 invariant mass method is taken as systematic errors, shown in Fig. 4.25.

4.5 Directed Flow from AMPT Model

In this section, directed flow (v_1) of the charged hadron and identified particles has been studied in the framework of a multi-phase transport (AMPT) model for ^{197}Au + ^{197}Au

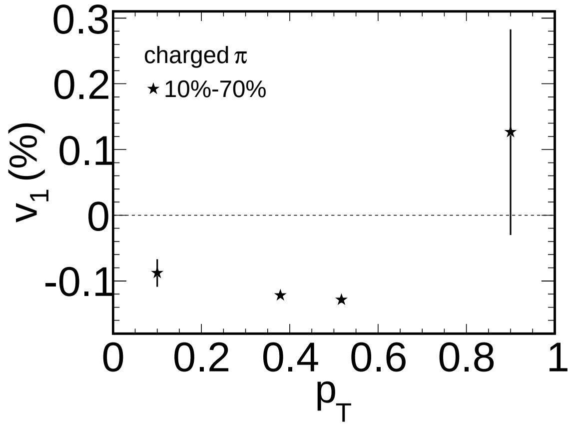

Figure 4.23: The pion directed flow as function of p_T in centrality 10%-70% from Au+Au collision at 200 GeV.

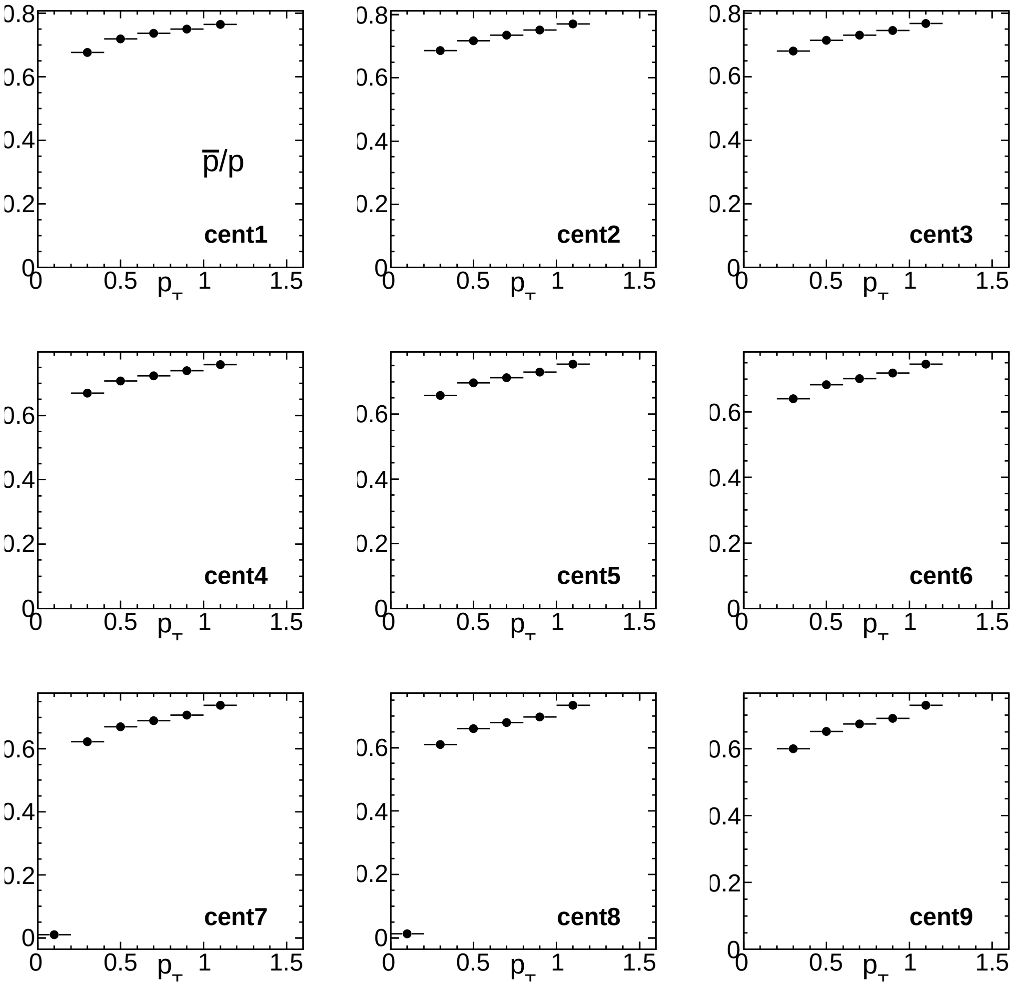

Figure 4.24: The particle dN/dp_T ratio of antiproton and proton from the peripheral(cen1) to central collision(cen9).

types	dv_1/dy	χ^2/ndf
method 1	-0.22 ± 0.03	23.7/5
method 2	-0.17 ± 0.02	24.7/5

Table 4.6: Kshort dv_1/dy slopes from from two methods in Au+Au collisions at $\sqrt{s_{NN}} = 200$ GeV.

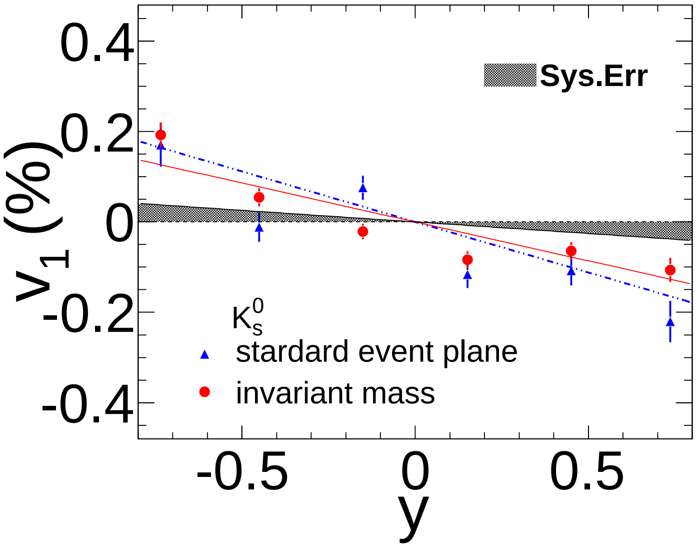

Figure 4.25: The $v_1 vs.y$ for K_S^0 in different methods:1)standard event plane method(blue triangles); 2)$v_1 vs.m_{inv}$ method. The solid and dashed lines present the linear fits. The systematic error is shown in shadow bands.

collisions at 6 energies ($\sqrt{s_{NN}}$ =200, 130, 62.4, 39, 17.2 and 9.2 GeV). The rapidity (y), centrality and energy dependence as function of directed flow for charged particles over a wide rapidity range are shown. The comparison with the measurements from STAR and PHOBOS are made at available top energies. The particle type dependence in a wide rapidity range has been discussed. This study could help us understand deeply about the energy dependence of directed flow. It can be also served as a valuable reference for the RHIC Beam Energy Scan program (BES).

4.5.1 Introduction of the AMPT model

The AMPT model consists of four main components [50]:

1. The initial conditions:
   It includes the spatial and momentum distributions of the mini-jet partons and soft string excitations. All of them are obtained from the HIJING model [51].

2. The partonic interactions:
   The scattering among partons are modeled by Zhang's parton cascade (ZPC) [52]. It includes two-body scattering with pQCD (with screening masses)'s cross-sections.

3. The conversion from partonic matter to hadronic matter:
   In the default version of the AMPT model, see Fig. 4.26 [53], the partons are recombined with their parent strings when they stop interacting, and result in the strings fragmentation into hadrons according to the Lund string fragmentation model [54]. In the AMPT model version with string melting, shown in Fig. 4.27 [55], the quark coalescence is common used instead of the combination partons into hadrons.

4. The hadronic interactions:
   The dynamics of the subsequent hadronic matter is described by the a relativistic transport(ART) [56] model. It is with modifications and extensions.

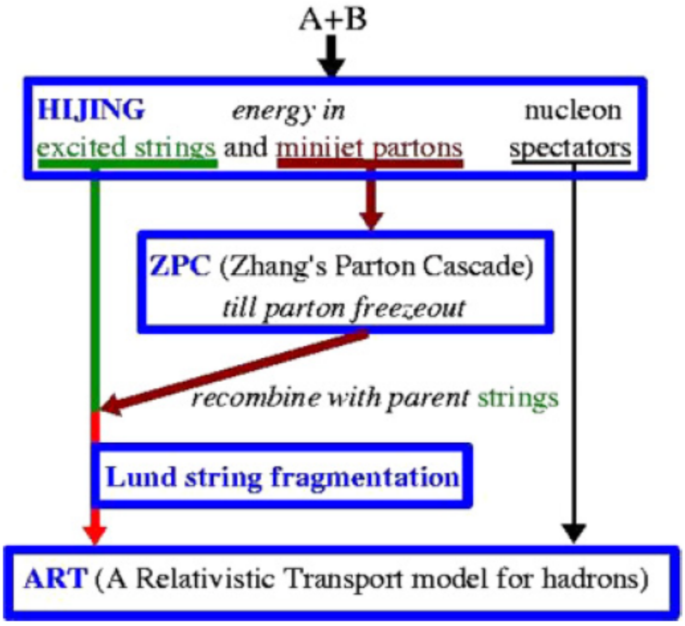

Figure 4.26: Structure of the default AMPT model.

In our analysis, the partonic cross section is chosen as 3 mb as suggested in Ref. [57]. As mentioned in Ref. [57], the selection of cross section will not effect the directed flow results. All the errors presented in this section are statistical errors only.

4.5.2 Analysis and results from AMPT model

Fig. 4.28 shows $v_1(y)$ of charged particles from AMPT model in collision energies of 200, 130, 62.4, 39, 17.2 and 9.2GeV. The centrality is divided into three bins: 0-30%, 30%-60% and 60%-80%, based on the impact parameter (b) distribution in the AMPT model. We found that the calculations with string melting scenario is used for high energies (200, 130, 62.4, 39GeV), while default scenario is suitable for low energies(17.2 and 9.2GeV) calculations. The reason for choosing in this way is explained in the following. It is argued in the Ref. [58, 59, 57] that the string melting section should be used to explain flow around midrapidity at top RHIC energies, and default setting could describes data at 9.2 GeV the best. That is because the energy density at the RHIC top energies is mush higher than the critical density for the QCD phase transition. More explanations and discussions on different AMPT configurations can be found later in the next paragraph.

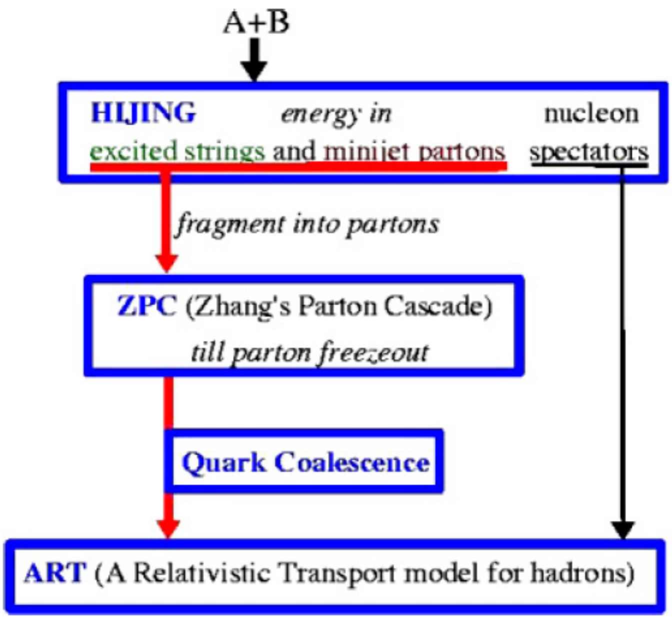

Figure 4.27: Structure of the AMPT model with string melting.

All results are obtained within the transverse momentum cut $p_T < 4.0$ GeV/c. The results are compared with experiments -STAR[?, ?] and PHOBOS[?]. The centrality is 0-40% central collisions from the PHOBOS experiment while 30%-60% in 200GeV 0-60% in 9.2GeV for STAR experiment. In general, $v_1(y)$ is larger at low energies than at high energies from AMPT model, and the same trend is shown in results from the experiment. At top RHIC energies, AMPT underestimated v_1. That is due to the turn-off of mean-field potentials in ART, it used to describe the hadronic scattering in AMPT model as mentioned in Ref. [50]. However, within the rapidity range$(-2.0 < y < 2.0)$, the v_1 shape from AMPT calculations and experimental results are in good agreement by scaling experimental results with a factor of 0.25.

The proton and pion's directed flow$(v_1 v.sy)$ are shown in Fig. 4.29. The $v_1(y)$ from pions and protons are shown different signs at low energies. It's regarded as the effect from the nucleon shadowing and baryon stopping [37, ?]. With the energy increase, the absolute values of the v_1 shape at midrapidity decrease. It is mostly profound for protons. The proton $v_1(y)$'s slope(dv_1/dy) keeps decreasing until energy is high enough, then the sign changes and proton's slope begins to flow together with pions. This is consistent with the "anti-flow" or the third flow compent picture [?]. As explained in Ref. [?],

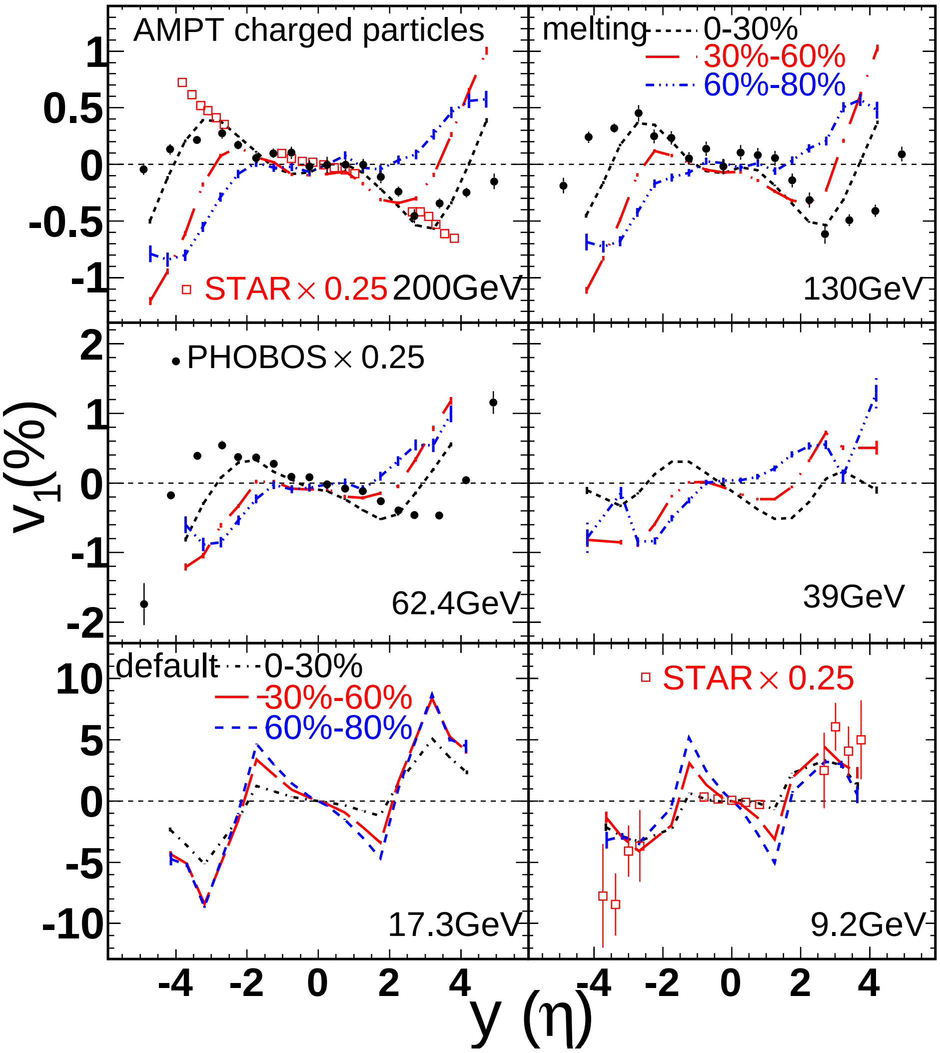

Figure 4.28: Charged particles' v_1 as function of rapidity in the AMPT model and comparison with results from the STAR and PHOBOS experiment (plotted as $v_1(\eta)$) in the Au+Au collisions at $\sqrt{s_{NN}}$ = 200GeV. The dashed lines are AMPT result from different centrality bins: 0-30%(black), 30%-60%(red), 60%-80%(blue).

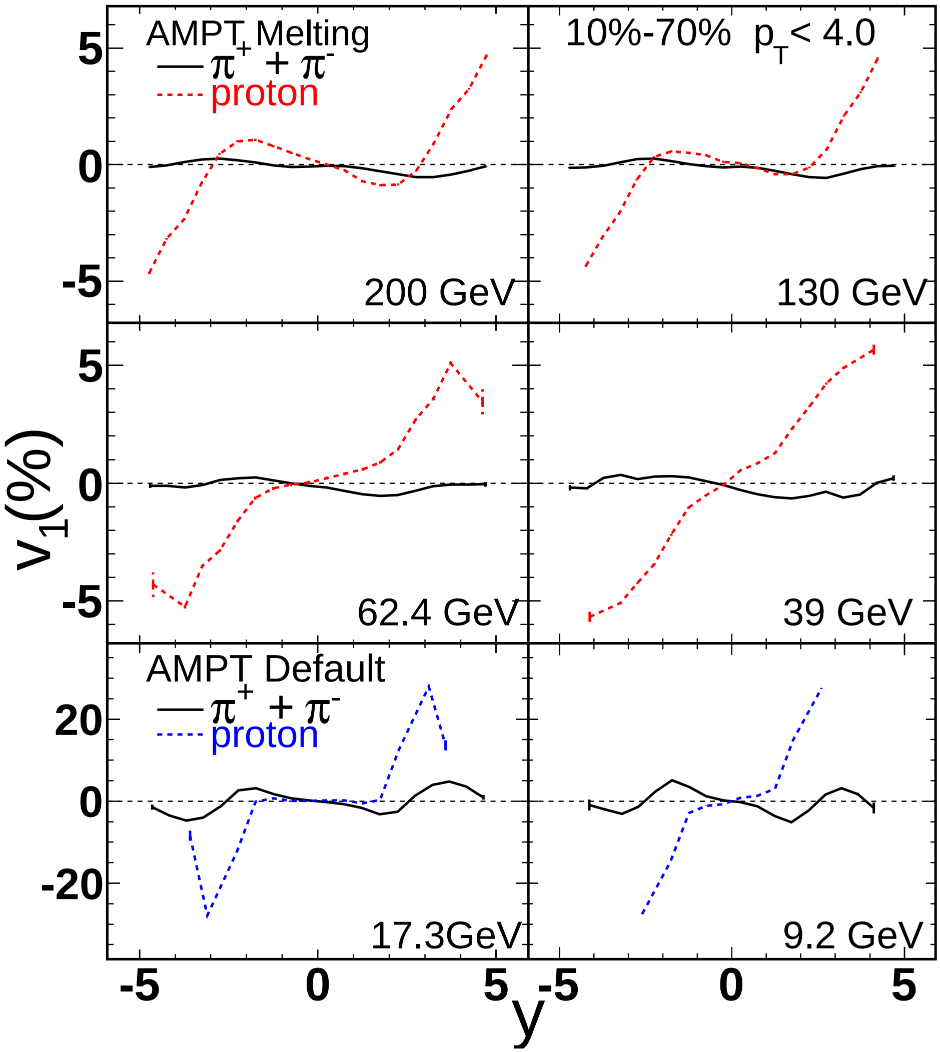

Figure 4.29: Directed flow as function of rapidity from proton(solid lines) and pion(dashed lines) in AMPT at centrality 10%-70%.

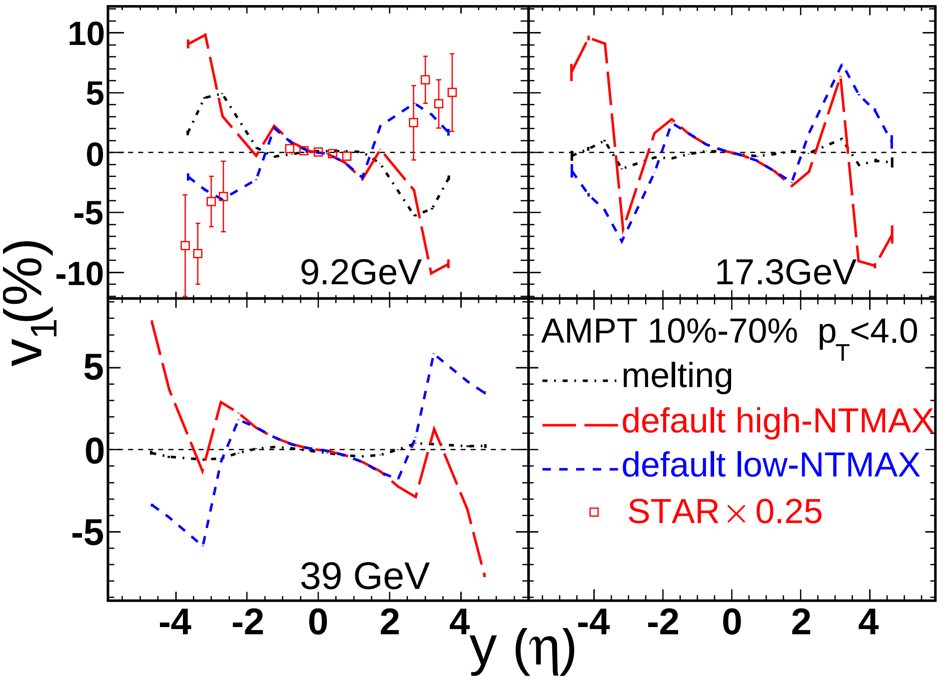

Figure 4.30: In AMPT model, charged particles' $v_1(y)$ in 10%-70% from 9.2 GeV (upper left panel),17.3 GeV (upper right panel) and 39 GeV (down left panel). The dashed lines show results from three AMPT versions in colors: the string melting scenario(black), the default scenario with high-NTMAX(red) and the default scenario low-NTMAX(blue). The STAR's data are plotted as a function of η.

the "bounce-off" motion and the "anti-flow" compete with each other in midrapidity, if "anti-flow" is strong enough especially at top RHIC energies, it overcomes the "bounce-off" motion effect. It causes protons to change their sign in $v_1(y)$ and flowing the dv_1/dy sign of pions.

To demonstrate the effect on directed flow results due to different configurations in AMPT, charged particles' $v_1(y)$ from centrality 10%-70% are presented in Fig. 4.30 in low energy collisions. The results are from AMPT calculations with the string melting scenario and the default scenario. The similar AMPT study for higher energies have been made in [57]. The calculation with string melting version in AMPT model gives the smallest v_1 slope around mid-rapidity and is close to data. More about two different default scenarios are also studied:

- one is calculated with NTMAX=2500, symbolled as high-NTMAX

- the other, NTMAX=150, named as low-NTMAX

Note that here NTMAX stands for the number of time-steps for the hadron cascade, more detail Ref. [50]. Larger NTMAX means a thoroughly developed hadron cascade since the 0.2fm/c*NTMAX is the termination time (all in the center of mass frame) in the hadron cascade from AMPT model. In the low energies, the comparison of v_1 calculated between low-NTMAX and high-NTMAX shows big different - $v_1(y)$ changes its sign at large rapidity under the condition of that the hardonic cascade'time is long enough. In default AMPT, the NTMAX should be much more than 150 used to describe v_1 at large rapidity correctly. The calculation made with high-NTMAX failed to repeat the experiment data, it may due to the lack of the mean-field in the hadron cascade in AMPT. This is a unpreventable effect at low energies when the nuclei passage time is not negligible . But at high energies, it has different story. The AMPT calculation with high-NTMAX at high energy has been shown in [60]. We address the comparison around midrapidity only, and results presented in this section are made with low-NTMAX unless otherwise specified.

The charged particles'excitation function is shown in Fig. 4.31 and compared with the experimental data. The centrality for AMPT model is 10%-70%. The centrality selection from PHOBOS data in different energies is 0-40%. The centrality selection for STAR data are 0-60% for 9.2 GeV, 10%-70% for 62.4 GeV, and 30%-60% for 200 GeV. In order to obtain the integrated v_1, one needs to fold in the spectra at different energies. It brings in an additional layer of systematics. Thus instead, we present the slope of $v_1(y')$ around normalizes mid-rapidity ($|y'| < 0.5$) extracted from the normalized ($y' = y/y_{beam}$), where y_{beam} is the beam rapidity. All the AMPT calculations underestimate the experimental data in the energy range 39 GeV and above, in this energy region, the string melting version AMPT model is used. However, they rightly predict the trend of the energy dependence. On the other side, the string melting version does not work well in the low energies, such as 9.2 GeV. But the calculation with the default AMPT seems better and the results show in the same direction of data yet is a little bit far from the data.

In AMPT model, the hadron re-scattering effect on directed flow v_1 can be done

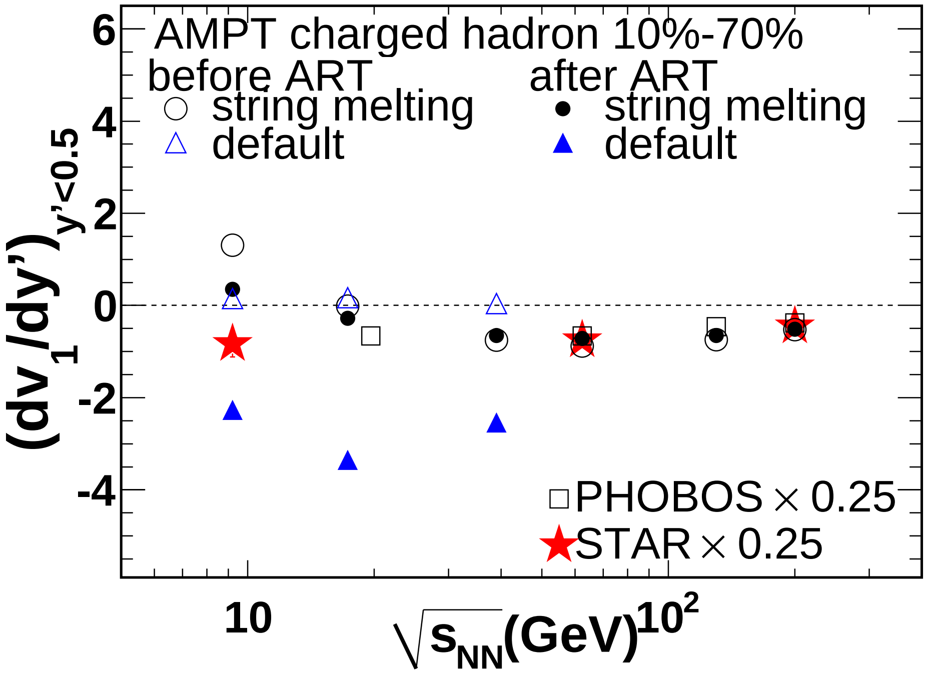

Figure 4.31: The directed flow's excitation function - dv_1/dy' within the normalized rapidity $|y'| < 0.5$ as a function of incident-energy from charged particles. The experiment results from STAR(stars) and PHOBOS(squares) are showed and scaled by a factor of 0.25. The AMPT calculatons with string melting before ART is presented in open circles and after hadron cascade are depicted with full circles. The open triangles represent the default AMPT calculations before ART and the full triangles stands of the results after hadron cascade.

by switching off the hadron cascade. Throughout comparing the difference between the result with (open symbols) and without (solid symbols)hadron cascade, it shows that the hadronic cascade has a significant effect on low energy v_1 results, but this effect is quite small little for that of high energies. This can be regarded as, the hadron re-scattering become less important due to the presence of strong collective motion built up beforehand when the energy is high enough.

CHAPTER 5

Discussion and Summary

In this thesis, we present p, $\bar{p}$,K_s^0, Λ and $\bar{\Lambda}$'s directed flow in Au+Au collisions at $\sqrt{s_{NN}}$ = 62 GeV and $\sqrt{s_{NN}}$ = 200 GeV, measured by the STAR experiment in Run 4. To improve the event plane resolution, we determine the event plane from sideward deflection of spectator neutrons measured by STAR' s shower maximum detector at zero degree calorimeters (ZDC-SMD), together with tracks reconstructed with the forward time projection chambers (FTPC). Our result is presented as a function of pseudorapidity, transverse momentum and centrality. within the rapidity range we studied, at both energies, proton v_1 is less than 1%, and antiproton is less than 2%, v_1 for K_s^0, Λ and $\bar{\Lambda}$ are found not more than 5%.

STAR's measurements of directed flow (v_1) at midrapidity for $\pi^{\pm}$, K$^{\pm}$, K$_S^0$, p and $\bar{p}$ in Au + Au collisions at $\sqrt{s_{NN}} = 200$ GeV in Run 7 are presented. A negative $v_1(y)$ slope is observed for most of produced particles ($\pi^{\pm}$, K$^{\pm}$, K$_S^0$ and $\bar{p}$). In 10-70% central collisions, $v_1(y)$ slopes of pions, kaons(K$_S^0$), and antiprotons are found to be mostly negative at midrapidity. However, protons exhibits a clearly flatter shape than that for antiprotons. A sizable difference is seen between v_1 of protons and antiprotons in 5-30% central collisions. Comparison to models (RQMD, UrQMD, AMPT, QGSM with parton recombination, hydrodynamics with a tilted source) is made. None of models explored can describe $v_1(y)$ for pions and protons simultaneously. An additional mechanism besides the anti-flow needs to explain the centrality dependence of the difference between the $v_1(y)$ slopes of protons and antiprotons.

The directed flow of charged hadron and identified particles has been studied in the framework of a multi-phase transport (AMPT) model, for ^{197}Au+^{197}Au collisions at $\sqrt{s_{NN}}$ =200, 130, 62.4, 39, 17.2 and 9.2 GeV. The rapidity, centrality and energy dependence of directed flow for charged particles over a wide rapidity range are presented. v_1 values calculated from the AMPT model for different energies are discussed. It is found that the AMPT model gives the right shape of v_1 versus y while underestimating the magnitude, possibly due to the lack of mean-field in its hadron cascade. In AMPT, the proton v_1 slope changes its sign when the energy increases to 130 GeV and begins to have the same sign as that of pions, as expected in the "anti-flow" scenario. The effect on v_1 due to string melting, low-NTMAX and high-NTMAX are illustrated. The energy dependence of the v_1 slope at midrapidity is compared to experimental data, and AMPT can describe the trend of energy dependence while missing the magnitude by a fraction of 75%. Hadronic rescattering is found to be less important at high energies as the strong collective motion becomes to be the dominant dynamics. These studies can help us to understand the collective dynamics at early times in relativistic heavy-ion collisions, and they can also be served as references for the RHIC Beam Energy Scan program.

Experimentally we can access this phase diagram and vary these initial conditions by changing the beam energy. Thus a beam energy scan (BES) program will help us to explore the QCD phase diagram and to locate the critical point. As a first step of the BES program, RHIC made a test run for Au + Au collisions at $\sqrt{s_{NN}} = 9.2$ GeV. The directed flow results from Au + Au 9.2 GeV are similar to those obtained from collisions at similar energies.

References

[1] BRAHMS, PHENIX, PHOBOS, and STAR Collaboration, Nucl. Phys. A **757** Issues 1-2 (2005).

[2] K.A. Peacock (2008). The Quantum Revolution. Greenwood Publishing Group. P125. ISBN 031333448X.

[3] F. Wilczek. "QUANTUM CHROMODYNAMICS (QCD): THE MODERN THEORY OF THE STRONG INTERACTION." Ann. Rev. Nucl. Part. Sci. **32**: 177-209 (1982).

[4] A. Khodjamirian. "Quantum chromodynamics and hadrons: An elementary introduction." 2004. hep-ph/0403145.

[5] S. Bethke. "alpha(s) 2002." Nucl. Phys. Proc. Suppl. **121**:74-81 (2003). hep-ex/0211012.

[6] D. J. Gross and F. Wilczek. Phys. Rev. Lett. **30** 1343 (1973).

[7] H. D. Politzer. Phys. Rev. Lett. **30** 1346 (1973).

[8] Olivier Pene. "An Introduction to lattice QCD." 1995. hep-ph/9504271.

[9] J.Adams *et al.*, (STAR Collaboration), Nucl. Phys. A **757** 102 (2005).

[10] J.Adams *et al.*, (STAR Collaboration), Phys. Rev. Lett. **91** 072304 (2003).

[11] K.H.Ackermann *et al.*, (STAR Collaboration), Phys. Rev. Lett. **86** 402 (2001).

[12] F.R. Brown *et al.*, Phys. Rev. Lett. **65** 2491 (1990).

[13] O.Scavenius *et al.*, Phys. Rev. C **64** 045202 (2001); N.G.Antoniou *et al.*, Phys. Lett. B **563** 165 (2003); M.Asakawa and K.Yazaki, Nucl. Phys. A **504** 668 (1989); A.Barducci *et al.*, Phys. Lett. B **231** 463 (1989); A.Barducci *et al.*, Phys. Rev. D **41** 1610 (1990); A.Barducci *et al.*, Phys. Rev. D **49** 426 (1994); J.Berges and K.Rajagopal, Nucl. Phys. B **538** 215 (1999); M.A.Halasz *et al.*, Phys. Rev. D **58** 096007 (1998); Y.Hatta and T.Ikeda, Phys. Rev. D **67** 014028 (2003).

[14] M.A.Stephanov, Prog. Theor. Phys. Suppl. **153** 139 (2004); M.A.Stephanov, Int. J. Mod. Phys. A **20** 4387 (2005).

[15] Helen Caines (for the STAR Collaboration), arXiv:0906.0305v1.

[16] B.I.Abelev *et al.*, (STAR Collaboration) SN0493 : Experimental Study of the QCD Phase Diagram & Search for the Critical Point: Selected Arguments for the Run-10 Beam Energy Scan, http://drupal.star.bnl.gov/STAR/starnotes/public/sn0493.

[17] H. Liu *et al.* (E895 Collaboration), Phys. Rev. Lett. **84** 5488 (2000).

[18] J. Barrette *et al.* (E877 Collaboration), Phys. Rev. C**56** 3254 (1997); Phys. Rev. C **55** 1420 (1997).

[19] A. M. Poskanzer and S. A. Voloshin, Phys. Rev. C **58** 1671 (1998).

[20] J. Brachmann *et al.* Phys. Rev. C **61** 024909 (2000).

[21] L. P. Csernai and D. Röhrich, Phys. Lett. B **458** 454 (1999).

[22] H. Stöcker, Nucl. Phys. A **750** 121 (2005).

[23] E. Schnedermann and U. Heinz, Phys. Rev. Lett. **69** 2908 (1992).

[24] D. E. Kahana *et al.*, Phys. Rev. Lett. **74** 4404 (1995).

[25] J. Barrette *et al.* (E877 Collaboration), Phys. Rev. Lett. **73** 2532 (1994).

[26] Piotr Bożek and Iwona Wyskiel, Phys. Rev. C **81**, 054902 (2010).

[27] M. Harrison, T. Ludlam, and S. Ozaki, “RHIC project overview.”, Nucl. Instrum. Meth., A **499**:235-244 (2003).

[28] K. H. Ackermann *et al.* “STAR detector overview.” Nucl. Instrum. Meth., A **499**:624-632, 2003.

[29] W. J. Llope *et al.*, Nucl. Instrum. Methods A **522** 252 (2004).

[30] J. Barrette *et al.* (E877 Collaboration) Phys. Rev. C **56** 3254 (1997).

[31] M. Anderson *et al.*, Nucl. Instrum. Method. A **499** 659 (2003).

[32] K.H. Ackerman *et al.*, Nucl. Instr. Method. A **499** 709 (2003).

[33] C. Adler *et al.*, Nucl. Instrum. Methods Phys. Res., Sect. A **470**, 488 (2001); The STAR ZDC-SMD has the same structure as the STAR EEMC (end cap electromagnetic calorimeter) SMD: C. E. Allgower *et al.*, Nucl. Instrum. Methods Phys. Res., Sect. A **499**, 740 (2003); STAR ZDCSMD proposal, STAR Note SN-0448, 2003.

[34] S. Eidelman *et al.*, Phys. Lett. B, **592** 1 (2004).

[35] http://usa.hamamatsu.com/hcpdf/parts H/H6568 series.pdf http://www.phenix.bnl.gov/phenix/WWW/publish/togawa/localpol/smd/H6568.pdf

[36] S. Margetis. STAR Note **0367** (1998).

[37] R. J. Snellings, H. Sorge, S. A. Voloshin, F. Q. Wang and N. Xu, Phys. Rev. Lett **84**, 2803 (2000).

[38] H. Sorge, Phys. Rev. C **52** 3291 (1995).

[39] M. Bleicher and H. Stöcker, Phys. Rev. B **526** 309 (2002).

[40] J. Adams *et al.* (STAR Collaboration), Phys. Rev. C**72** 014904 (2005).

[41] B. I. Abelev *et al.* (STAR Collaboration), Phys. Rev. C**81** 024911 (2010).

[42] J. Y. Chen, J. X. Zuo, X. Z. Cai, F. Liu, Y. G. Ma and A. H. Tang, Phys. Rev. C **81**, 014904 (2010).

[43] G. Burau, J. Bleibel, C. Fuchs, A. Faessler, L. V. Bravina, and E. E. Zabrodin, Phys. Rev. C **71** 054905 (2005). J. Bleibel, G. Burau, A. Faessler and C. Fuchs, Phys. Rev. C **76** 024912 (2007).

[44] Piotr Bożek, private communication, 2010.

[45] S. V. Afanasiev *et al.* (NA49 Collaboration), Phys. Rev. C **66**, 054902 (2002); C. Alt *et al.* (NA49 Collaboration), Phys. Rev. C **77**, 024903 (2008); Phys. Rev. C **73**, 044910 (2006); T. Anticic *et al.* (NA49 Collaboration), Phys. Rev. C **69**, 024902 (2004).

[46] B. I. Abelev *et al.* (STAR Collaboration), Phys. Rev. C **79**, 034909 (2009).

[47] J. Adams *et al.* (STAR Collaboration), Phys. Rev. C **73**, 034903 (2006).

[48] B. I. Abelev *et al.* (STAR Collaboration), Phys. Rev. Lett. **101** 252301 (2008).

[49] C. Alt *et al.* (NA49 Collaboration), Phys. Rev. C **68** 034903 (2003).

[50] Z. W. Lin, C. M. Ko, B. A. Li, B. Zhang and S. Pal, Phys. Rev. C **72**, 064901 (2005).

[51] X. N. Wang and M. Gyulassy, Phys. Rev. D **45**, 844 (1992); M.Gyulassy and X. N. Wang, Comput. Phys. Commmun. **83**, 307 (1994).

[52] B. Zhang, Comput. Phys. Commun. **109**, 193 (1998).

[53] Z. W. Lin and C. M. Ko, Phys. Rev. C **68**, 054904 (2003).

[54] B. Andersson, G. Gustafson and B. Soderbery, Z. Phys. C **20**, 317 (1983).

[55] Z. W. Lin and C. M. Ko, J. Phys. G **30**, S263 (2004).

[56] B. Li, A. T. Sustich, B. Zhang and C. M. Ko, Int. J. Mod. Phys. E **10**, 267 (2001).

[57] C. M. Ko and L. W. Chen Nucl. Phys. A **774**, 527 (2006).

[58] J. H. Chen *et.al*, Phys. Rev. C **74**, 064902 (2006).

[59] J. X. Zuo *et.al*, Eur. Phys. J. C **55** 463 (2008).

[60] L. W. Chen, V. Greco, C. M. Ko, and P. Kolb, Phys. Lett. B **605** 95 (2005).

Publication List

1. B. I. Abelev *et. al.*, STAR Collaboration, “System-Size Independence of Directed Flow Measured at the BNL Relativistic Heavy-Ion Collider”, *Phys. Rev. Lett.*, **101**, 252301 (2008).

   Primary authors: **Jiayun Chen**, Feng Liu, Aihong Tang, Gang Wang.

2. **Jiayun Chen** (for STAR Collaboration), “Directed flow of identified particles from Au+Au collisions at RHIC”, *J. Phys. G Nucl. Part. Phys.*, **35**, 044072 (2008).

3. **Jiayun Chen** (for STAR Collaboration), “Particle Production in Au+Au Collisions at $\sqrt{s_N N} = 9.2$ GeV, *Proceeding of Science(CPOD)*, **047**, (2009).

4. Jiaxu Zuo **Jiayun Chen** *et. al.*, “Partonic effect on anisotropic flows of Ω baryon for Au+Au at 62.4 and 200 GeV/c”, *Eur. Phys. J. C*, **55**, 463-467 (2008).

5. **J.Y. Chen**, J.X. Zuo, X.Z. Cai, F. Liu, Y.G. Ma, A.H. Tang, “Energy Dependence of Directed Flow in Au+Au Collisions from a Multi-phase Transport Model”, *Phys. Rev. C*, **81**, 014904 (2010).

6. B. I. Abelev *et. al.*, STAR Collaboration, “Identified particle production, azimuthal anisotropy, and interferometry measurements in Au+Au collisions at $\sqrt{s_N N} = 9.2$ GeV”, *Phys. Rev. C*, **81**, 024911 (2010).

   Primary authors: **Jiayun Chen**, Feng Liu, Aihong Tang, Gang Wang.

7. **Jiayun Chen** (for STAR Collaboration), “Anisotropic flow at RHIC”, *Chinese Physics C(HEP & NP)*, **349:**, 1443-1445, 9 (2010).

8. **Jiayun Chen** (for STAR Collaboration), “Directed flow of identified particles from Au+Au collisions at RHIC”, *Indian Journal of Physics*, **84**, 12, 1801-1805(2011).

9. **Jiayun Chen** (for STAR Collaboration), “Directed flow measurements from STAR”, *Journal of Physics: Conference Series*, **270**, 012045 (2011).

10. H. Agakishiev, *et. al.*, STAR Collaboration, “Directed Flow of Identified Particles in Au + Au Collisions at $\sqrt{s_N N} = 200$ GeV”, paper proposal to *Phys. Rev. Lett.*.

    STAR internal review

    Primary authors: **Jiayun Chen**, Feng Liu, Aihong Tang, Gang Wang

Presentations

Talks

1. Directed flow at RHIC,

   The Hot Quarks 2010, La Londe les Maures, France, 2010.7.

2. Anisotropic Flow at RHIC

   The 8th National Delegate Conference of High Energy Physics Associate and Annual Conference, Nanchang, China, 2010.4.

3. Directed flow from Au+Au Collision at 200GeV

   The 13th National High Energy Nuclear Physics Conference, Hefei, China, 2009.11.

4. Anisotropic Flow at RHIC

   The 5th International Conference on Quarks and Nuclear Physics, Beijing, China, 2009.9.

5. Particle Production in Au+Au Collisions at 9.2GeV

   The 5th International Workshop on Critical Point and Onset of Deconfinement (CPOD), BNL, USA, 2009.6.

6. Directed flow of identified particles from Au+Au Collisions at RHIC

   The 10th National Conference on Particle Physics, Nanjing, China, 2008.4.

7. Directed flow of identified particles from Au+Au Collisions at RHIC

   The International Conference on Strangeness in Quark Matter, Levoča, Slovakia, 2007.6.

8. Directed flow of identified particles from Au+Au Collisions at RHIC

   Collective Dynamics in High-Energy Collisions, LBNL, USA, 2007.5.

Posters

1. Directed flow of identified particles in Au + Au Collisions at $\sqrt{s_{NN}} = 200$ GeV

   The 3rd HOPE meeting, Tokyo, Japan, 2011.3.

2. Model study of incident-energy dependence and particle type dependence of directed flow at RHIC

   International Conference Quark Matter, in Knoxville, Tennessee, USA, 2009.3.

3. Incident-energy study of Directed Flow from Au+Au collisions at RHIC

   International Conference on Strangeness in Quark Matter, Beijing, China, 2008.10.

4. Directed flow of identified particles from Au+Au collisions at RHIC

   Quark Matter 2008, Jaipur, India, 2008.2.

Acknowledgements

Many thanks to all people who help me to complete this thesis!

....